

**COHERENT ULTRAFAST OPTICAL MANIPULATIONS OF SEMI-  
CONDUCTOR QUANTUM DOTS FOR QUANTUM COMPUTATION**

by

Yanwen Wu

A dissertation submitted in partial fulfillment  
of the requirements for the degree of  
Doctor of Philosophy  
(Physics)  
in The University of Michigan  
2008

Doctoral Committee:

Professor Duncan G. Steel, Chair  
Professor Roberto D. Merlin  
Professor Theodore B. Norris  
Professor Georg Raithel  
Associate Professor Luming Duan



© Yanwen Wu 2008  
All Rights Reserved

## ACKNOWLEDGEMENTS

I thought this would be the easiest part of the thesis, but I am finding it extremely difficult now for words cannot express how lucky I am to be constantly immersed in the help and support from those around me. My only hope is that these few lines will at least begin to convey my deepest gratitude.

First and foremost, I would like to thank my advisor, Professor Duncan Steel. You have not only guided my growth as a physicist, but also given me much invaluable advice in life. You have taught me how to be an independent and confident individual as well as a scientist. I would also like to thank my committee members: Professor Luming Duan, Professor Roberto Merlin, Professor Ted Norris, and Professor Georg Raithel for your scientific discussions and encouragement. Additionally, many thanks go to Professor Paul Berman, Professor Alan Krisch and Professor Jean Krisch. Your excellent teaching and mentoring during my clueless undergraduate years have inspired me to pursue a graduate study in physics.

I could not have achieved all this without my labmates. I would like to give thanks to Dr. Elaine Li for being a "slave driver" and a mentor who always believed in me even when I didn't, and to Dr. Gurudev Dutt and Dr. Jun Cheng for sharing your knowledge and never showing an ounce of impatience during my "stupid" questions. I would also like to show my appreciation to Xiaodong Xu for the fun and engaging scientific and non-scientific discussions, to Erik kim (my "official lackey") for putting up with my bossiness, and to Qiong Huang, Katherine Smirl and Bo Sun for always keeping me honest and never letting me get away with sloppy physics explanations. To all, I would like to extend this big "Thank you" for the great times and great food

during Friday group lunches and football parties.

Last but not least, to my mother (Zhongyi Huang), father (Dr. Shezhang Wu), and sister (Chaowen Wu), I show my deepest gratitude. You are my fountain of unconditional love and support. Mom and Dad, I am especially grateful to you for believing in my potential and encouraging me to follow my own path. And Chaowen, thank you for proofreading this acknowledgement, or Pokemon, as you put it.

## TABLE OF CONTENTS

<b>ACKNOWLEDGEMENTS</b>		ii
<b>LIST OF TABLES</b>		vi
<b>LIST OF FIGURES</b>		vii
<b>LIST OF APPENDICES</b>		ix
<b>CHAPTER</b>		
<b>1.</b>	<b>Introduction to quantum computation</b>	1
1.1	From classical to quantum computation	2
1.2	Quantum computing basics: bits, gates, algorithms	5
1.3	Physical implementations of quantum computation	11
1.4	Thesis chapter outlines	13
<b>2.</b>	<b>Theory and characterization of semiconductor quantum dot structures</b>	16
2.1	Semiconductor theory of quantum dots	17
2.2	Neutral interface fluctuation quantum dots	23
2.3	Charged interface fluctuation quantum dots	28
2.4	Gated self-assembled quantum dots	32
2.5	Chapter summary	35
<b>3.</b>	<b>Theory and experimental methods of nonlinear spectroscopy</b>	36
3.1	Master equations of density matrix elements	37
3.2	Maxwell-Bloch equation	41
3.3	Differential transmission detection using phase-sensitive optical modulation	44
3.4	Chapter summary	49
<b>4.</b>	<b>Phase-Sensitive Consecutive Qubit Rotations in a Single Semiconductor Dot</b>	50
4.1	Theory of transient excitation in a closed two-level system	51

4.1.1	Two-level systems and the Pauli matrices . . . . .	52
4.1.2	Rotations in the Bloch sphere representation . . . . .	54
4.2	Experimental setup and phase-locking two optical pulses . . . . .	57
4.3	Consecutive rotations of an exciton-based qubit . . . . .	58
4.4	Chapter summary . . . . .	66
<b>5.</b>	<b>Density Matrix Tomography of a Single Exciton-Based Qubit</b>	<b>67</b>
5.1	Theory on the rotations of the measurement basis . . . . .	68
5.2	Density matrix tomography of a single exciton-based qubit . . . . .	70
5.2.1	Calibration and renormalization of the differential transmis- sion signal . . . . .	72
5.2.2	Reconstruction of the single qubit density matrix . . . . .	75
5.3	Chapter summary . . . . .	80
<b>6.</b>	<b>Selective Optical Control of Electron Spin Coherence in Singly Charged Quantum Dots via Optically dark and Bright States</b>	<b>81</b>
6.1	Theory on stimulated Raman transitions and ground state coher- ence in a $\Lambda$ system . . . . .	82
6.1.1	Exact solutions in the probability amplitude approach . . . . .	84
6.1.2	Perturbative solutions in the density matrix approach . . . . .	87
6.2	Optical coherent spin control experiment in singly charged quan- tum dots . . . . .	90
6.2.1	Experimental setup and quantum beat signals . . . . .	90
6.2.2	Coherent control of the initialized spin . . . . .	98
6.3	Chapter summary . . . . .	103
<b>7.</b>	<b>Summary and Future Directions</b>	<b>105</b>
7.1	Voltage dependent PL and modulated absorption of a single InAs dot . . . . .	107
7.2	Future directions in InAs self-assembled quantum dots . . . . .	110
7.2.1	CW and transient efforts on single dots . . . . .	110
7.2.2	InAs double-dot molecules . . . . .	111
7.3	Summary . . . . .	113
	<b>APPENDICES</b> . . . . .	<b>115</b>
	<b>BIBLIOGRAPHY</b> . . . . .	<b>125</b>

## LIST OF TABLES

### Table

1.1	Gate operation matrices of the controlled-NOT gate and the SWAP gate	8
2.1	Polarization selection for transitions in the spin-trion system under a magnetic field in the Voigt geometry . . . . .	32
5.1	Values of the fidelity, $F$ , of single qubit density matrix tomography .	80



## LIST OF FIGURES

<u>Figure</u>		
1.1	Moore's law showing the feature size of the transistor versus year . . .	3
1.2	Schematic of the multi-qubit Deutsch-Jozsa algorithm . . . . .	10
2.1	Pictorial comparison between discrete energy states and energy bands	18
2.2	Expanded view of the III-IV semiconductor energy band dispersion near $\vec{k} \sim 0$ . . . . .	20
2.3	Energy density of states as a function of reduced dimension . . . . .	21
2.4	STM and NSOM images of the GaAs IFQDs . . . . .	25
2.5	Neutral GaAs IFQD sample structure and aperture map of NRL-1197King	26
2.6	Energy level diagram in a single neutral GaAs IFQD . . . . .	27
2.7	Charged GaAs IFQD sample structure . . . . .	29
2.8	Energy level diagram in a singly charged GaAs IFQD in the absence and presence of a magnetic field . . . . .	31
2.9	Charged InAs IFQD sample growth, structure, and charging scheme .	33
2.10	Energy level diagram in a singly charged InAs SAQD in the absence and presence of a magnetic field . . . . .	34
3.1	Diagram of a general open three-level $\Lambda$ system . . . . .	38
3.2	Diagram of the double optical modulation setup . . . . .	47
4.1	Diagram of a closed two-level system . . . . .	51
4.2	Bloch sphere representation . . . . .	55
4.3	Phase-locking experimental setup . . . . .	58
4.4	Energy level diagram of excitons . . . . .	59
4.5	Degenerate DT measurements by ps pulsed and cw lasers . . . . .	60
4.6	Time domain DT measurement of exciton $T_1$ . . . . .	62
4.7	Ideal Bloch representation of the two consecutive $\frac{\pi}{2}$ rotations of a qubit	64
4.8	Experimental results of two consecutive $\frac{\pi}{2}$ rotations of a qubit . . . .	65
5.1	Passive and active rotations . . . . .	69
5.2	Pulse shaper in 4-f configuration . . . . .	71
5.3	Level diagram and readout . . . . .	73
5.4	Rotating and measuring the coherence components of a Bloch vector	76
5.5	Decay plots of single $\pi/2$ pulse and interferogram . . . . .	77
5.6	Density matrices of a single qubit created by a $\pi/2$ pulse . . . . .	78
6.1	Diagram of a closed three-level $\Lambda$ system . . . . .	83
6.2	Density matrix elements as a functions of pulse area in two-level and three-level $\Lambda$ systems . . . . .	87
6.3	Ensemble spectra and energy level diagrams of trion . . . . .	91

6.4	Balanced detection setup and spin quantum beats . . . . .	95
6.5	Two pulse initialization . . . . .	97
6.6	Bloch representation of the evolutions of the initialized spin polarization	100
6.7	Experimental results of the spin control experiment . . . . .	102
7.1	Voltage dependent PL map and absorption of a single InAs SAQD . .	108
7.2	InAs double dot molecule growth, structures, and voltage dependent PL map . . . . .	112
A.1	Stabilization scheme for the Michelson interferometer . . . . .	117

## LIST OF APPENDICES

### Appendix

A.	Interferometer stabilization circuits . . . . .	116
B.	Derivation of square pulse solution in three-level $\Lambda$ system . .	118
C.	Complete process of the spin coherent control . . . . .	120

## CHAPTER 1

### Introduction to quantum computation

As the size of transistors quickly and inevitably approaches the atomic scale as predicted by Moore's law [1], quantum effects become more relevant and will subsequently hinder further progress in classical computation. The concept of the quantum computer embraces the physics that governs the quantum mechanical nanoscale world. Rather than adhering to the notion that a computational bit must be either 0 or 1, the quantum bit (qubit) can be 0, 1, or any superposition thereof. This results in a massive parallelism in computation that makes certain quantum algorithms excel above their classical counterparts. For a few important algorithms, a quantum computer with only a handful of qubits can complete the desired task billions of times faster than the most powerful conventional supercomputer.

A working quantum computer must be capable of handling at least  $10^4$  logic gate operations on individual and any entangled pairs of qubits within the lifetime of the qubits [2]. The zero-dimensional semiconductor quantum dot (QD) is among the most popular candidates for the implementation of a practical quantum computer. These artificially fabricated "atoms" have discrete energy states much like their natural counterparts, which can be mapped directly into the states of a qubit. Their semiconductor nature also allows for easy integration with the hardware of modern day computers.

In this thesis, the main focus is on using coherent optical excitation to investigate zero dimensional semiconductor structures, such as neutral and charged quantum dots, for the implementation of physical qubits for quantum information processing

devices.

This chapter provides an overview of the history of computation and the emerging crisis in modern classical computation that drives the thriving field of quantum information theory. The basic requirements for the construction of a practical quantum computer are enumerated and the concepts of quantum bits and quantum gates are presented. A few exemplary quantum algorithms are also briefly discussed to showcase the superior computational power a quantum computer possesses. Lastly, we briefly review the promising quantum systems considered for the physical implementation of a quantum computer with an emphasis on quantum dot systems.

### **1.1 From classical to quantum computation**

The field of computer science started with the advent of the Turing machine. The Turing machine is a conceptual machine with infinite memory and infinitely-sized variables. It has been shown that any classical algorithm, regardless of the physical system on which it is performed, can eventually be simulated by a Turing machine. Therefore, the Turing machine is also regarded as a universal machine for classical computation. Since the algorithms are universal, the limitation of classical computation ultimately lies in the physical systems used, which will always have limited memory and size of the input variable.

The first physical manifestations of a programmable digital computer such as the Electronic Numerical Integrator And Computer (ENIAC) utilized nearly twenty thousand vacuum tubes. The vacuum tube is a voltage-controlled device that provides a unidirectional current flow from a heated cathode filament to an anode plate. However, the cumbersome size of the vacuum tubes posed an immediate problem as the ENIAC weighed nearly 30 tons and took up an entire 680 ft<sup>2</sup> room. In addition, the power consumed by the ENIAC was 150 kW. With the added issue of constant tube failures leading to prolonged computational downtime, increasing the computation capability of such design by adding more tubes was highly unlikely. As the development of the physical computer seemingly came to a halt, the discovery of the semiconductor

and the subsequent invention of the transistor launched the revolutionary leap into modern day digital computing.

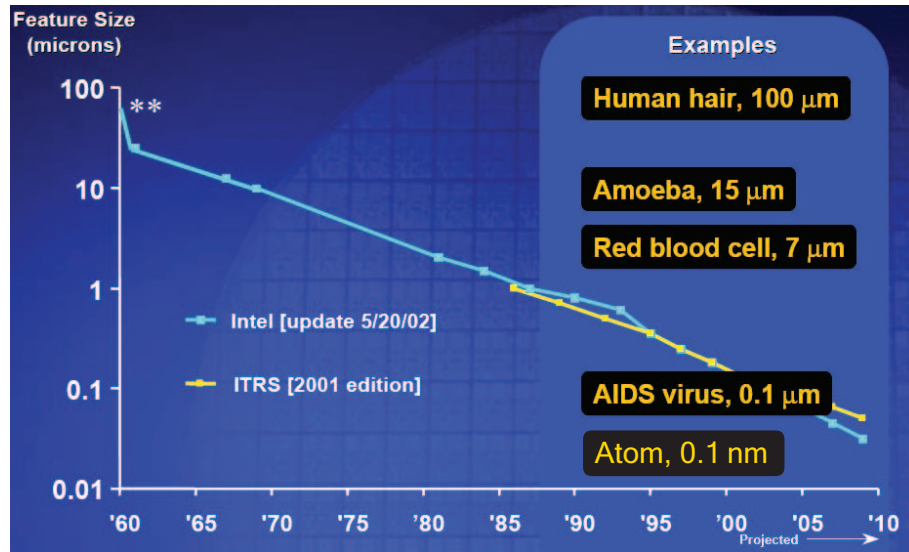


**Figure 1.1:** Moore's law showing the feature size of the transistor versus year. The figure is taken from Reference [3]. ITRS stands for International Technology Roadmap for Semiconductors.

The transistor functions similar to the vacuum tube with a size on the  $\mu\text{m}$  scale and power consumption in the mW range. Over the years, advances in semiconductor fabrication techniques and the vast infrastructure dedicated to the manufacturing of state-of-the-art integrated micro-circuits have created an invisible force steadily shrinking the cost and size of the transistor to vanishingly small values. In 1965, Gordon Moore noticed the correlation and stated that the number of the transistors on a chip will roughly double every two years while maintaining the same production cost [1]. This extrapolation was later extended to the size of the individual transistors on a chip as shown in Figure 1.1 [3]. Astonishingly, Moore's simple law has thus far accurately predicted the situation in reality. If this trend continues, in the near future classical computation will face a new crisis as the size of the transistor becomes comparable to the size of individual atoms where quantum mechanical effects begin to blur the well-defined classical bit values of 0 and 1.

Instead of despairing, physicists embraced the quantum challenge, and the field of quantum information took form. The inspiration for the discipline came from

the independent realization by Richard Feynman and Paul Benioff in 1982 that if information is but a recording of the states of a physical system and computation is a designed manipulation of the same physical system, then there must be a means of information storage and computation in a physical quantum system as well. What is most alluring about the prospect of quantum computation is the possibility of an enormously more powerful form of computation altogether. As Richard Feynman had stated in his 1959 American Physical Society lecture, *there's plenty of room at the bottom* [4], the Hilbert space of a quantum system is unimaginably large and the level of quantum complexity embedded in a quantum system has the potential of enabling a new class of computation unfathomable in a classical system, even beyond the capability of the universal Turing machine.

The probabilistic nature and the non-local correlation (ability of entanglement) of a quantum system are what lead to the massive-parallelism property unique to quantum information processing. Simply put, it allows for the processing of multiple inputs states simultaneously through quantum entanglement. It is true that a classical computer can simulate parallel operations with multiple systems, but the definitive advantage lies in the number of operations required to accomplish the task. Powered by this massive-parallelism, a quantum computer can complete a calculation in much fewer operations than multiple classical computers. A few examples showcasing this power are the Deutsch-Jozsa algorithm [5] discussed in Section 1.2, Shor's factoring algorithm [6], and Grover's search algorithm [7]. Exactly how much better is quantum computation compared to classical computation? The previous description of "much fewer operations" is not a satisfactory answer. In order to truly quantify the computation power of a given computation system, we must look at how the number of operations grows as a function of the size of the problem. For an *efficient* algorithm, the growth is polynomial in time (e.g.  $N^x$ , where  $N$  denotes the number of bits in the input and  $x$  is a fixed constant). On the other hand, an *inefficient* algorithm will grow as a superpolynomial function with respect to  $N$  (e.g.  $x^N$ , where  $x$  is some constant), although it is sometimes more generally referred to as exponential growth. It is also important to keep in mind that the definition of

“*efficiency*” is machine-independent, meaning that an *efficient* quantum algorithm should perform on the order of polynomial time in any physical quantum system. This is analogous to the idea of the Turing machine for classical algorithms. The algorithms mentioned above are examples of efficient quantum algorithms that have yet to be matched in the classical computation regime.

In the computational sense, the probabilistic nature of the quantum system is tremendously advantageous. However, when measurement of the output is considered, this quantum property leads to detrimental results. The entanglement leading to massive-parallelism is fragile against any external disturbance, including measurement. Once the quantum system is subject to such a disturbance, the massively entangled state collapses to one of its component states, and all the information stored is lost. Another obstacle threatening the applicability of a quantum computer is the inevitable quantum error. Even without the intentional disturbance of measurement, any perturbation from the environment can lead to error in the quantum system. Classically, errors are corrected by having backup copies of the same bits, but the quantum no-cloning theorem [8] forbids the duplication of any pure arbitrary quantum state.

The pressing issues of measurement and error correction are not so threatening if we learn to change our point of view and approach the problems quantum mechanically. Ultimately, the key is to be able to distinguish between a classical question and a quantum mechanical question. In the next section, we present the quantum basics of bits, gates, and algorithms in an effort to provide some insights into the realm of quantum computation. This section is only a brief overview of the broad subject of quantum information processing. For more in depth information and instruction on this topic, Reference [9] and [10] are both excellent sources.

## 1.2 Quantum computing basics: bits, gates, algorithms

The abundance of success in the theoretical development of quantum information processing aroused a tidal wave of eagerness in the experimental community to make



physical quantum computer a reality. In 2000, David DiVincenzo established a set of basic criteria that a physical quantum computer must satisfy in order to be deemed practical [2]. This set of criteria consists of five fundamental requirements as listed in Reference [2]:

1. *A scalable physical system with well characterized qubits,*
2. *The ability to initialize the state of the qubits to a simple fiducial state,*
3. *Long relevant decoherence times, much longer than the gate operation time,*
4. *A “universal” set of quantum gates,*
5. *A qubit-specific measurement capability.*

The first and third requirements are mostly imposed on the intrinsic properties of the quantum system chosen. A well characterized qubit means a well-isolated two-level system capable of interacting predictably with the designated means of external manipulation (quantum operations). Such a two-level system must also possess a long decoherence time within itself and with other qubits so that an entangled state can reliably accommodate a complete algorithm before it dephases. The third requirement also implies the inclusion of error correction algorithms for fault-tolerant quantum computation. If the qubit cannot exist long enough to allow for error correction, then it is not practical for quantum computation. With the inclusion of error correction codes, the minimum requirement on the decoherence time of a qubit is that it must be at least  $10^4$ - $10^5$  times the duration of a single quantum operation. The scalability part of the first requirement is usually the deciding factor for the practicality of a particular quantum system, since a non-scalable system is practically useless. Accomplishing scalability often requires clever structural engineering because the design of the system must allow for mutual interaction between qubits while maintaining the individuality of each qubit. Most importantly, the complexity of entangling qubits in a successfully scaled system should not increase exponentially with respect to the number of qubits involved.

The second, fourth and fifth requirements are all related to the mode of quantum operation chosen for the quantum system. State initialization, single and two-qubit operations, and individual qubit readout are merely different manners of exciting and interacting with the quantum system of choice with precision and control. The rest of this section will cover all aspects of these three requirements in the order of increasing structural complexity. We will start with the concept of a single qubit, then advance to two-qubit quantum gates, and conclude the discussion with multi-gate quantum algorithms.

The qubit is the fundamental logical unit for quantum computation. Unlike the classical bit, which takes on a discrete value of 0 or 1, a qubit is a vector spanning the entire Hilbert space of a two-level quantum system. The general form of a qubit is written as a superposition of states  $|0\rangle$  and  $|1\rangle$ ,

$$|qubit\rangle = \alpha |0\rangle + \beta |1\rangle, \quad (1.1)$$

where  $\alpha$  and  $\beta$  are the probability amplitudes of being in the qubit state  $|0\rangle$  and  $|1\rangle$ , respectively. The state and evolution of the qubit can also be described in the Bloch sphere representation which will be introduced in later chapters.

Controlling the qubit is equivalent to performing arbitrary unitary rotations in the Hilbert space of the two-level system. Any such unitary rotation of the qubit state constitutes a single qubit operational gate, including Rabi oscillation of the states. A frequently used single qubit gate is the Hadamard gate ( $U_H$ )

$$U_H = \frac{1}{\sqrt{2}} \begin{bmatrix} 1 & 1 \\ 1 & -1 \end{bmatrix}. \quad (1.2)$$

The Hadamard gate is similar to a  $\frac{\pi}{2}$  rotation. It is often used in combination with other gates to initialize and prepare the input state prior to an algorithm and controllably collapse the output into a measurable state upon completion of an algorithm.

In order to accomplish universal quantum computation, quantum operations involving multiple qubits are also necessary. Physically, these multiple qubit gates require interaction between individual qubits. The nature of the interactions can take on many forms, such as the Coulomb force, collective quantized vibrational modes of

particle motion, or the spin-spin interaction. In practice, it is desirable to be able to turn these interaction forces on and off at will, adding another obstacle in the design of a scalable system. Much like the single qubit gates, multi-bit gates are merely unitary operations on multiple qubit states.

Examples of simple two-qubit gates are the controlled-NOT gate and the SWAP gate represented by the gate operation matrices in Table 1.1. The input states for these gates are  $|00\rangle$ ,  $|01\rangle$ ,  $|10\rangle$  and  $|11\rangle$ . For the controlled-NOT gate, the first qubit is the control, which conditionally flips the second qubit if its value is 1 and does nothing if its value is 0. For the SWAP gate, the values of the two qubits are swapped. When paired with a single qubit rotational gate, each of these two-qubit gates can form a universal set of quantum gates which can be used to construct any quantum operations or algorithms. Other universal sets of gates also exist, including the single-set Deutsch gate [11] and the the controlled-phase gate. The choice between different sets of universal gates rests in their convenience in the particular physical system. For example, in the spin-based qubit system in a quantum dot, the SWAP gate set is the most obvious choice due to the spin-spin nature of the inter-qubit interaction.

controlled-NOT gate					SWAP gate				
	$ 00\rangle$	$ 01\rangle$	$ 10\rangle$	$ 11\rangle$		$ 00\rangle$	$ 01\rangle$	$ 10\rangle$	$ 11\rangle$
$ 00\rangle$	1	0	0	0	$ 00\rangle$	1	0	0	0
$ 01\rangle$	0	1	0	0	$ 01\rangle$	0	0	1	0
$ 10\rangle$	0	0	0	1	$ 10\rangle$	0	1	0	0
$ 11\rangle$	0	0	1	0	$ 11\rangle$	0	0	0	1

**Table 1.1:** Gate operation matrices of the controlled-NOT gate and the SWAP gate. For the controlled-NOT gate, the first qubit acts as the control for the second qubit.

Now that we have a fair understanding of simple quantum gates, we can advance to the more complicated logical structure of quantum algorithms. The most simple yet most defining quantum algorithm is the Deutsch-Josza (DJ) algorithm [5]. Although it serves no practical purpose, the DJ algorithm epitomizes the incredible capacity

of massive-parallelism in a quantum computer. The problem posed by Deutsch is the “easy” task of distinguishing whether an unknown function inside a black box is *constant* ( $f(0) = f(1)$ ) or *balanced* ( $f(0) \neq f(1)$ ). In a classical computer, the solution to the DJ problem is to process  $f(x)$  for both inputs 0 and 1, then compare the two results. Whether one chooses to compute  $f(x)$  serially with one computer or in parallel with two computers, the number of operations required is always two.

In the quantum computer, we can immediately take advantage of the quantum parallelism in a single qubit. Instead of processing the input twice, the input qubit is prepared in a superposition of  $|0\rangle$  and  $|1\rangle$ . The quantum DJ algorithm,  $U_{f(x)}$ , designed around the function  $f(x)$  is

$$U_{f(x)} : |x\rangle|y\rangle \rightarrow |x\rangle|y \oplus f(x)\rangle, \quad (1.3)$$

where  $\oplus$  represents the exclusive OR (XOR) logical operation. The two-qubit to two-qubit transformation is to maintain the unitary property of the quantum operation. Qubit  $|y\rangle$  acts as an axillary bit, which transfers information from the calculation to qubit  $|x\rangle$  and returns to its initial value,

$$\begin{aligned} U_{f(x)} : |x\rangle \frac{1}{\sqrt{2}}(|0\rangle - |1\rangle) &\rightarrow |x\rangle \frac{1}{\sqrt{2}}(|f(x)\rangle - |1 \oplus f(x)\rangle) \\ &= |x\rangle (-1)^{f(x)} \frac{1}{\sqrt{2}}(|0\rangle - |1\rangle). \end{aligned} \quad (1.4)$$

For  $|x\rangle = \frac{1}{\sqrt{2}}(|0\rangle + |1\rangle)$ , qubit  $|x\rangle$  acquires a relative phase shift of  $\pi$  between its qubit states if  $f(x)$  is a *balanced* function and no relative phase shift if  $f(x)$  is a *constant* function. If we perform a Hadamard operation on qubit  $|x\rangle$  to read out the result, we will measure  $U_H|x\rangle = |1\rangle$  for a *balanced* function and  $U_H|x\rangle = |0\rangle$  for a *constant* function. In only a single quantum process of the function  $f(x)$ , the problem is solved.

The true power of this quantum algorithm becomes more prominent as the number of qubits involved increase to an arbitrary large  $N$ . The number of possible inputs for  $N$  bit is  $2^N$ , and the classical computer will have to make the same number of evaluations of  $f(x)$  for each input in order to draw a conclusion on the function. On the other hand, utilizing the massive-parallelism of a quantum computer, we can simply create a superposition state of all possible inputs which still only takes one computation of the function  $f(x)$  to acquire the solution as shown in Figure 1.2.

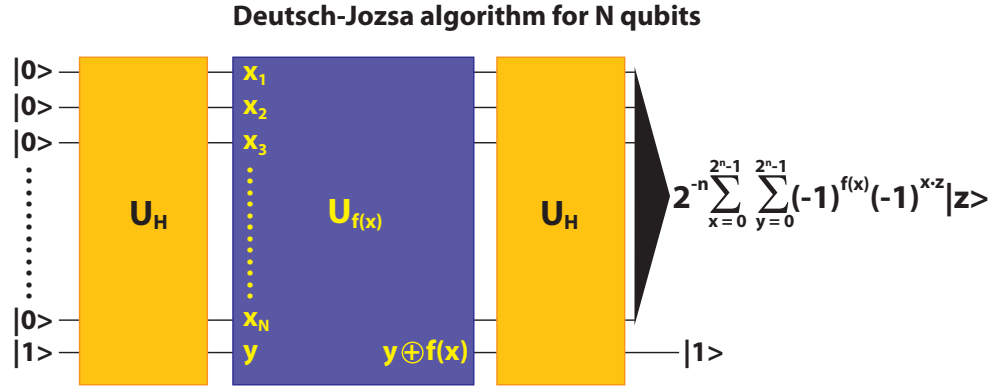


**Figure 1.2:** Schematic of the multi-qubit Deutsch-Jozsa algorithm.  $U_H$  is the unitary operation of the Hadamard gate and  $U_{f(x)}$  is the unitary operation related to the function  $f(x)$ . The  $x_N$ 's are the input bits and  $y$  is the auxiliary bit. For a *balanced* function, the sum at the output on the right will be 0.

The DJ problem illustrates a few important aspects of quantum computation. The advantage of massive parallelism is exemplified as a quantum algorithm solves an exponentially hard classical problem in polynomial time. In this case, it is a polynomial of order 0. In addition, it stresses the reward of thinking quantum mechanically. The classical way of thinking would naturally lead us to first concentrate on the solutions of  $f(x)$ , then analyze their equality and inequality. Alternatively, thinking quantum mechanically, we put the emphasis on the inherent difference between the two functions and how it can be employed by the quantum system to give an immediate result. Furthermore, transferring the embedded information in the massively correlated quantum state to a measurable result is not trivial. In the case of the DJ problem, a simple Hadamard gate can make that transfer from the superposition state in Equation 1.4 to the measurable qubit state of  $|0\rangle$  or  $|1\rangle$ . But in general, formulating the measurement process requires ingenuity.

In addition to the simple DJ algorithm, there are more complex and applicable quantum algorithms such as Shor's factoring algorithm [6]. Shor's algorithm is designed to factor the products of two extremely large prime numbers ( $N \gg 400$  digits) using a quantum Fourier transform (QFT) technique. The best classical factoring algorithm is the "number field sieve" [12] with a performance time of

$T_{classical} \simeq \exp[1.9(\ln N)^{1/3}(\ln \ln N)^{2/3}]$ . For 400 digits, the factoring time is  $10^{10}$  years, the age of the universe. The same 400 digit number factored using Shor's algorithm which operates in polynomial time ( $O[(\ln N)^3]$ ) would take less than 3 years. The details of both algorithms are beyond the scope of this thesis, nevertheless, the comparison in performance speed is convincing evidence of the spectacular advantages a quantum computer could have over a classical computer.

### 1.3 Physical implementations of quantum computation

The tremendous successes enjoyed in the theoretical development of quantum information processing inspired a soaring response from the experimental community, which announced several quantum systems as promising candidates for the physical realization of the quantum devices for quantum information processing. A few common proposals are single photons (quantum optics), superconductors, nuclear magnetic resonance (NMR) systems, atoms, and quantum dots.

The qubit states in single photons can be the orthonormal polarizations states. Single photon quantum information processing excels in the area of quantum communication and quantum networking [13, 14]. Long distance quantum key distribution in 148 km of optical fiber [15] and in 144 km of free space [16] have been successfully demonstrated in recent years. Quantum cryptography systems using photons are also commercially available. However, the lack of a steady supply of true single photons makes this pure optical scheme unsuitable for quantum computation.

Qubit states in superconductors can be charge-based (the presence or absence of Cooper pairs) [17–19], flux-based (flux quanta) [20–22] or a hybrid of both. The quantum operation used in the the superconductor regime is electrostatic in nature. Qubit states in NMR are not well-defined pure states but rather an ensemble of spins in a mixture of pure and maximally mixed states [23, 24]. Qubit states  $|0\rangle$  and  $|1\rangle$  are read out as an absorption and an emission in the NMR spectrum. Quantum operations in NMR quantum computation are done using radio frequency (RF) fields. Both systems have shown considerable progress towards physical quantum computation by

demonstrating quantum gates and multi-bit quantum algorithms. Nevertheless, electrostatic and RF quantum operations are limited in speed by the electronics used. In order to make the most of the decoherence time of a given quantum system, optical quantum systems are desirable where ultrafast optical pulses can be considered as a means of quantum manipulation.

The atom is an optical system with well-defined discrete energy states. The atomic qubit states of choice are the spin states of a single electron, due to its stability against long range Coulomb interactions. The atom has the advantage of an extensive literature base dedicated to the subject of optical properties and transitions between the atomic energy states. Therefore, the optical manipulation of an atom is relatively easy. However, capturing a single atom long enough to perform the manipulations is difficult. In fact, the cooling and trapping of atoms with coherent laser light was such an extraordinary feat that it earned Steven Chu, Claude Cohen-Tannoudji and William D. Phillips the Nobel prize in 1997 [25]. Laser cooling is but one step in a rigorous cooling scheme [26–29] to prepare the atom in a state fit for quantum computation. Nevertheless, once atom trapping was established, quantum computing in atomic systems began to show rapid progress. Single and multiple qubit quantum gates were executed with high fidelity which demonstrated a universal set of gates [30]. The intrinsic coherence time of an atomic state can be as long as a few minutes. The limiting factor for the qubit lifetime is usually related to the instability of the traps. Initialization of the qubit states is accomplished through optical pumping, and measurements are enhanced using an optical cycling scheme. In addition, entanglement within a trap system using quantized vibrational modes of the trap [31] was achieved in a spatial “cat-state” [32]. Entanglement of the atom with a photon [33] and with an atom in another trap [34] were also demonstrated signifying the feasibility of a quantum network. Lastly, the scalability issue was addressed with the conception of an atomic shuttling trap on a chip [35]. Overall, the atomic system satisfies the DiVincenzo criteria and is one of the leading candidates in the field of quantum application.

The semiconductor quantum dot system is another highly promising optical sys-

tem that satisfies all five of DiVincenzo's basic criteria for the physical implementation of quantum computation. Moreover, the quantum dot system does not rely on the cumbersome traps required for the atomic systems since the dots are embedded on the semiconductor itself. Another added benefit of the quantum dot structure is the advanced integrated circuits fabrication technology. The available fabrication infrastructure allows for the ease in designing and manufacturing low-cost, scalable systems consisting such structures. This entire thesis is dedicated to the optical coherent manipulation of semiconductor quantum dot structure with the goal of realizing a practical quantum computing device.

#### **1.4 Thesis chapter outlines**

The subject of quantum information processing is a vast interdisciplinary field interconnecting computer science, information science and physical science. This chapter has only skimmed the surface of the topic to provide a sense of the awesome computing power a quantum system can offer and the motivation behind the research conducted in this thesis. The remaining chapters are dedicated more specifically to the optical coherent control of semiconductor quantum dot systems, which serves to highlight the unique optical properties of semiconductor quantum dots and to demonstrate the capabilities of such systems in the physical implementation of quantum information processing.

Chapter 2 is dedicated to the background physics and structures of the semiconductor quantum dot systems, which are our chosen quantum hardware for the implementation of a physical quantum computing device. We launch the discussion with an overview of general bulk semiconductor theory and introduce the concepts of energy bands and optically excitable quasi-particles such as excitons. This understanding of the higher dimensional semiconductor bulk is applied to the lower dimensional semiconductor quantum dot to explain the energy level structures in the valence and conduction bands. The three specific types of quantum dot systems presented in this chapter are the neutral and charged GaAs interface fluctuation quantum



dots and the voltage gated InAs self-assembled quantum dots. Their respective dot structures, optical properties and roles towards quantum information processing are explored and compared.

Chapter 3 provides a theoretical treatment of the optical interactions between the coherent light source of a laser and the energy states in a quantum dot. The interactions are calculated in both probability amplitude and density matrix approaches. The detectable classical signal field in the laboratory is linked to the quantum mechanically derived polarization source through the Maxwell-Bloch equations. This chapter also describes the differential transmission detection technique using modulated optical pump and probe beams, which allows for detection of weak signals in the presence of a noisy background from scattering and diffraction. This particular method is the main detection technique for the major experiments in this thesis.

Chapters 4-6 are the main experimental chapters. In Chapter 4, picosecond pulses are used to perform quantum operations. We show that by using an actively stabilized optical phase-locking scheme, phase information from one optical pulse can be written onto an exciton-based qubit in a neutral single GaAs quantum dot system and then successfully transferred to a subsequent pulse at some delay. This experiment demonstrates consecutive phase dependent qubit rotations and proves that the exciton quantum system has the ability to maintain coherent information during its decoherence lifetime.

Chapter 5 applies the phase dependent qubit rotations technique in the tomographic reconstruction of the density matrix of a single qubit. The controlled rotation is utilized to change the basis of measurement, which enables the measurement of both real and imaginary parts of the off-diagonal coherence terms. Although the measured density matrix deviates from the ideal case, we have complete knowledge of the sources of the error, and hence complete control of our quantum dot system. The main sources of errors are attributed to the intrinsic decay parameters of the quantum system and the finite pulse width of the laser pulses. In fact, the simulated density matrix including the experimental parameters agrees excellently with the measured density matrix.

Experiments in chapters 4 and 5 are all performed on the exciton-based qubit in a single neutral GaAs quantum dot system. Chapter 6 explores the more robust spin-based qubit in charged GaAs quantum dot systems. Here we demonstrate ultrafast spin manipulation utilizing an upper charged exciton (trion) state in pursuit of arbitrary spin rotation. Due to complications not completely understood in the interface fluctuation charged QD, a complete spin rotation is not observed. However, the result obtained in this chapter sets the stage for future work on ultrafast arbitrary spin rotations in InAs self-assembled quantum dots.

Finally, Chapter 7 will highlight a few future directions towards the ultimate goal of realizing a physical quantum computation device using quantum dot systems. The summary will include brief descriptions of current experiments on the spin-based qubit in gated InAs self-assembled quantum dots and some preliminary results on quantum dot molecules. These efforts are aimed towards accomplishing arbitrary single electron spin rotation (single qubit rotation) and ultimately creating a scalable quantum dot system with the possibility of performing qubit entanglement.

## CHAPTER 2

### Theory and characterization of semiconductor quantum dot structures

Quantum dots (QDs) are essentially three dimensionally confined structures that exhibit a discrete density of states. This distinctive characteristic earns QDs the informal title of “artificial atoms”. The QD’s unique optical properties have generated a great deal of interest in their potential applications in novel devices such as quantum dot lasers [36–42] and single photon source [43–49] for quantum communication. In recent years, the increasing flexibility and precision control in the engineering and fabrication of semiconductor nanostructures have also excited a vast effort towards physical implementation of quantum information processing using QD systems [50–55].

The three dimensional confinement necessary for a quantum dot can be fabricated using various methods. Spherical semiconductor nanocrystal QDs are chemically synthesized and passivated to produce a core-shell structure [56–59]. They are used in biological labelling [60, 61] due to their small sizes, typically on the order of 2–10 nm, and the fact the dots are individually separable. Lithographically etched QDs are formed by various artificial patterning and etching techniques directly on epitaxially grown semiconductor quantum wells [62–67]. The size of the lithographic dots, limited by the resolution of the patterning techniques, such as electron beam and laser etching, tends to be large with an in-plane dimension reaching 100 nm. The size and shape of the nanocrystal [68–71] and lithographically etched QDs can be fully controlled during fabrications.

The two species of QDs studied in this thesis work are naturally and spontaneously

formed during the molecular beam epitaxy (MBE) growth process. The first type of dot is the interface fluctuation QD (IFQD) formed by monolayer fluctuation of the semiconductor interface [72–75]. This type of dot form irregular islands with an average lateral scale of 50 nm, and has a large optical dipole moment around 100 D [76, 77]. The second type of dot is the self-assemble QD (SAQD) resulting from the strain of lattice mismatch between the two semiconductors [78–81]. The dot sizes of SAQDs are around 15 nm, which leads to stronger spatial confinement but also a smaller optical dipole in comparison to the IFQDs. The optical dipole moment of the SAQD is measured by our group to be around 30 D [82].

In this chapter, we begin the discussion with the semiconductor physics that governs the behavior of particles inside a QD in Section 2.1. Then, the three major species of dots under investigation (neutral and charged IFQDs and gated SAQDs) are compared in Section 2.2- 2.4 in terms of their fabrication process, sample structures and physical parameters, optical polarization selectivity, optical characterizations and practicality in the physical implementation of quantum information processing.

## 2.1 Semiconductor theory of quantum dots

Most optical behavior of particles inside a single QD can be predicted and described astoundingly well using only simple energy level models borrowed from atomic physics. However, there exist more differences than similarities between a single QD and an atom. One important contrast to the atom is the breakdown of spherical symmetry in a QD, which voids spin and orbital angular momenta as valid quantum numbers for describing the QD system. Therefore, in order to correctly apply the more simple atomic treatment on a QD system, we need to understand the more complex semiconductor physics that actually governs the behaviors of particles inside a single semiconductor QD.

To fully appreciate the idea that a semiconductor QD comprised of  $10^3$ - $10^6$  [83] of atoms can behave as a single atom, we must first grasp the concept of how individual atoms are arranged to define a semiconductor crystal structure. Excellent

detailed discussions of semiconductor materials can be found in References [84, 85]. The following is a brief overview of the subject.

In a single atom, the energy levels are discrete with inter-level transitions in the range of optical frequencies. In a solid, atoms are packed close to each other. While the tightly bound electrons in the inner shells experience negligible effect from other atoms, the weakly bound electrons in the outer shells of neighboring atoms strongly interact with each other through Coulomb exchange. These inter-atomic Coulomb interactions lift the degeneracies of the electron spatial energies. As a result, discrete energy levels are replaced by energy bands as shown in Figure 2.1, and the energetically forbidden regions formed between the energy bands are called bandgaps. The filling status of the last occupied energy band determines the properties of the solid. A solid with an incompletely filled energy band is a metal, while that with a fully occupied energy band characterizes both insulator and semiconductor. The distinction between pure insulators and semiconductors is often blurred. The primary difference lies in the bandgap energy between the last occupied band (valence band) and the first available band (conduction band). This bandgap energy is larger in insulators. In general for semiconductors, this energy separation is accessible using optical frequencies around and below the visible spectrum.

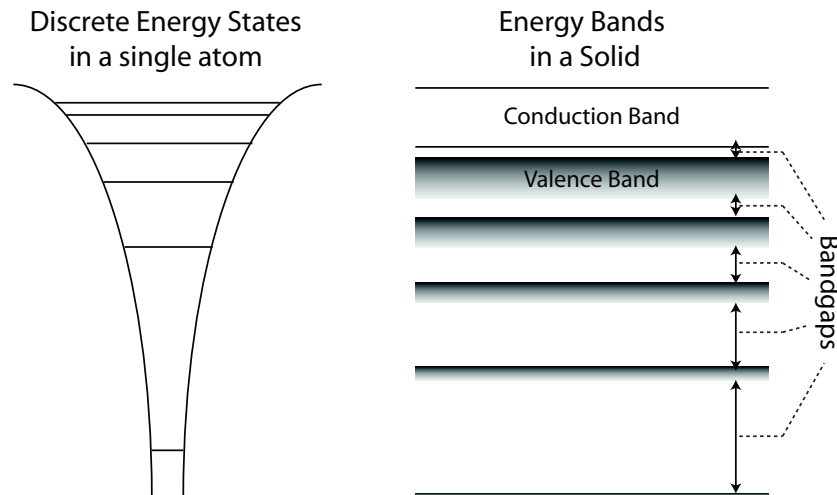


**Figure 2.1:** Pictorial comparison between discrete energy states in a single atom and energy bands in a solid.

The energy bands of a solid are not in a simple one-to-one correspondences with the original discrete atomic states, but rather, they are the results of coupling and mixing of multiple atomic energy states. Therefore, the behavior of electrons in a given energy band does not follow a straightforward atomic model. Nevertheless, in a periodically arranged crystalline bulk semiconductor structure, the wavefunctions of the electrons can be qualitatively modelled using the Schrödinger equation with a periodic potential  $W(\vec{\mathbf{r}})$ :

$$\left[ -\frac{\hbar^2}{2m} \nabla^2 + W(\vec{\mathbf{r}}) \right] \psi_{nk}(\vec{\mathbf{r}}) = \mathcal{E}_n(\vec{\mathbf{k}}) \psi_{nk}(\vec{\mathbf{r}}). \quad (2.1)$$

The form of  $\psi_{nk}(\vec{\mathbf{r}})$  in a given energy band  $n$  with reciprocal lattice vector  $\vec{\mathbf{k}}$  according to the Bloch theorem consists of a plane wave component,  $e^{i\vec{\mathbf{k}} \cdot \vec{\mathbf{r}}}$ , and an atomic component,  $u_{nk}(\vec{\mathbf{r}})$ ,

$$\psi_{nk}(\mathbf{r}) = \frac{e^{i\vec{\mathbf{k}} \cdot \vec{\mathbf{r}}}}{\sqrt{V}} u_{nk}(\vec{\mathbf{r}}), \quad u_{nk}(\vec{\mathbf{r}} + \vec{\mathbf{R}}) = u_{nk}(\vec{\mathbf{r}}), \quad (2.2)$$

where  $u_{nk}(\vec{\mathbf{r}})$  has full translational symmetry between Brillouin zones and  $V$  is the crystal volume. The energy term  $\mathcal{E}_n(\vec{\mathbf{k}})$  describes the dispersion within a band, and also gives rise to the notion of the effective mass, which is inversely proportional to the curvature of  $\mathcal{E}_n(\vec{\mathbf{k}})$ .

Calculating the exact forms of the electron wavefunction,  $\psi_{nk}(\mathbf{r})$ , and the energy band structure,  $\mathcal{E}_n(\vec{\mathbf{k}})$ , is tedious and requires a significant amount of work. The exact approach becomes especially dreadful considering that both functions need to be redetermined in different solids. Hence, it is much more desirable to use some forms of general approximation on the periodic potential,  $W(\vec{\mathbf{r}})$ , which can qualitatively summarize different structures with similar electron binding behaviors. Two of such approximations exist in the extreme cases of weak periodic potentials, where electrons are essentially free with wavefunctions of modified plane waves, and tight-binding potentials, where electrons are essentially bound to a single atomic site and retain some of their atomic orbital characteristic [84, 85].

Similar III-V semiconductors band structures, such as that of GaAs and InAs forming our QD structures, can be described using the tight-binding potential model.

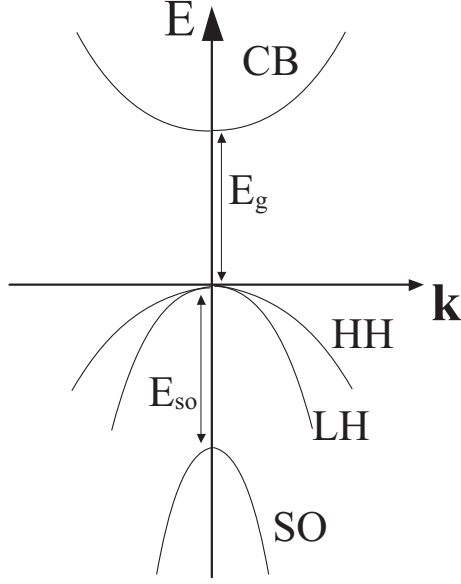


**Figure 2.2:** Expanded view of the III-IV semiconductor energy band dispersion near  $\vec{k} \sim 0$ . The bandgap energy is  $E_g$ , and the spin-orbital coupling energy between the split-off (SO) band and the light hole (LH) and heavy hole (HH) bands is  $E_{so}$ . CB and VB are the conduction and valence band, respectively.

In a single molecule, the outer shell electrons from each atom hybridize to form molecular bonds. As a result, the highest  $s$  and  $p$  energy states of these electrons are also mixed to form bonding and anti-bonding energy states. In the crystal structure, the bonding and anti-bonding levels become the valence and conduction bands, respectively. Near the center of the Brillouin zone where  $\vec{k} \sim 0$ , the conduction band has the properties of an  $s$ -orbital with a two-fold degeneracy due to spin. The valence band, on the other hand, has the properties of a  $p$ -orbital. Due to spin-orbital interaction, the six-fold degeneracy in a  $p$ -orbital is lifted to create a doubly degenerate band with  $j = \frac{1}{2}$  and two doubly degenerate bands with total angular momentum of  $j = \frac{3}{2}$  as illustrated in Figure 2.2. The  $j = \frac{1}{2}$  band is separated from the  $j = \frac{3}{2}$  bands by the spin-orbital coupling energy,  $E_{so}$ . At  $\vec{k} = 0$ , the valence band maximum,  $E_{so} = 0.34eV$  in GaAs and  $E_{so} = 0.41eV$  in InAs. Due to this separation, the  $j = \frac{1}{2}$  band is often called the split-off (SO) band. The  $j = \frac{3}{2}$  bands are degenerate at  $\vec{k} \sim 0$ , but this degeneracy is quickly lifted at non-zero values of  $\vec{k}$  due to anisotropy. The band with the larger curvature (smaller effective mass) is appropriately referred to as

the light-hole (LH) band with  $m_j = \pm\frac{1}{2}$ , and the smaller curvature (larger effective mass) band is the heavy-hole (HH) band with  $m_j = \pm\frac{3}{2}$ . Since our ultimate concern is the optical transition inside a QD, where three dimensional confinements restrict  $\vec{k}$  to be near zero, the dispersion of the bands can be neglected, and we can use the language of angular momentum to describe optical transitions. If necessary, a good approximation of the dispersion can be calculated using the Luttinger parameters derived from the  $\vec{k}\cdot\vec{p}$  perturbation theory [86,87].

### Density of States as a Function of Dimension

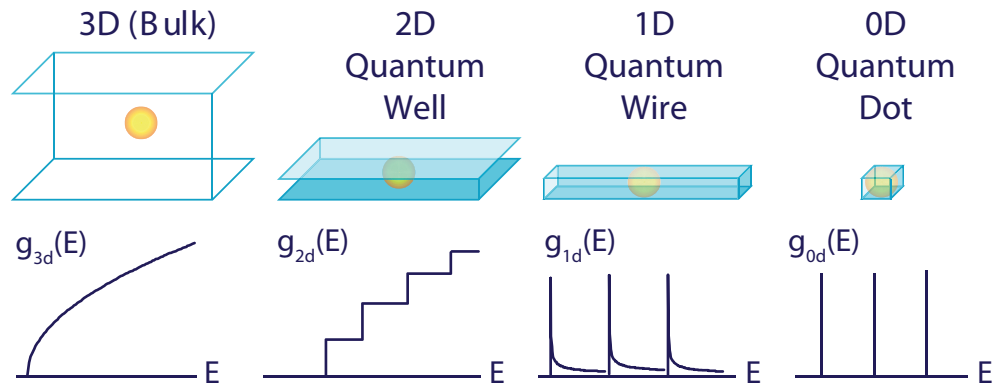


**Figure 2.3:** Energy density of states as a function of reduced dimension. The orange spheres are representatives of excitons where the size of the sphere is approximately the Bohr radius.

Confinements imposed in a semiconductor can lead to two dimensional structures of quantum wells, one dimensional quantum wires, or zero dimensional quantum dots as shown in Figure 2.3. The confinements change the density of state profile of the semiconductor and also drastically alter the optical properties of the semiconductor. Equations 2.4- 2.6 list the energy density functions for bulk, quantum well, quantum



wires and QDs,

$$3D \text{ Bulk} : g_{3d}(E) = \frac{1}{2\pi^2} \left( \frac{2m}{\hbar^2} \right)^{\frac{3}{2}} \sqrt{E}, \quad (2.3)$$

$$2D \text{ Well} : g_{2d}(E) = \frac{m}{\pi\hbar^2} \sum_i \Theta(E - E_i), \quad (2.4)$$

$$1D \text{ Wire} : g_{1d}(E) = \frac{1}{\pi} \left( \frac{m}{2\hbar^2} \right)^{\frac{1}{2}} \sum_{ij} \frac{1}{E - E_{ij}}, \quad (2.5)$$

$$0D \text{ Dot} : g_{0d}(E) = 2 \sum_{ijk} \delta(E - E_{ijk}), \quad (2.6)$$

where  $\Theta$  is the heavy-side step function and  $\delta$  is the delta function. As the dimensionality decreases in the semiconductor, abrupt features begin to appear in the energy density, signifying energy quantization in some form, which is especially apparent in the discrete  $\delta$  function density states of the zero dimensional QDs as presented in Figure 2.3.

As previously mentioned, QDs typically consist of  $10^3$ - $10^6$  atoms, which means the confinement is much larger than the size of an atom and, therefore,  $u_{nk}(\vec{r})$ , the atomic part of the Bloch wavefunction that is mainly defined within one Brillouin zone, is still valid in QDs. However, the plane wave envelope of the wavefunction,  $e^{i\vec{k}\cdot\vec{r}}$ , covering the entire semiconductor, is no longer an appropriate form of the wavefunction within the QDs in the presence of new boundary conditions. In place of a plane wave, the new wavefunction envelope inside a QD is in the form of a wave packet constructed by linear superpositions of multiple plane waves. An immediate analogy is “particle-in-a-box”. Due to the three dimensional spatial confinement, electrons in the QDs are localized at  $\vec{k} = 0$ , and the language of dispersion and energy band becomes irrelevant to dynamics inside a QD. Nevertheless, the angular momentum assignments to the conduction band and the LH and HH valence bands in bulk are still suitable labels for describing optical transitions in a QD, since they are defined for  $\vec{k} \sim 0$ .

Optical transitions in semiconductors can be categorized as either direct bandgap or indirect bandgap transitions. Since both GaAs and InAs are direct bandgap materials, we will concentrate on the direct bandgap type, which means both the maximum of the valence band and the minimum of the conduction band are located at the same position in  $\vec{k}$ . During optical excitation, electrons are promoted to the conduction

band, leaving vacancies, i.e. holes, in the valence band. Since the electron is negatively charged and the hole is positively charged, an attractive Coulomb interaction binds the two particles together to form an exciton, analogous to positronium. Due to this binding energy, exciton absorption is observed below the bandgap energy, distinguishing the excitons from non-interacting electron and hole pairs.

Behaviorally, the exciton is often considered as a quasi-particle with its center-of-mass and relative motions described by the envelope part of the excitonic wavefunction. The relative orbital motion of the electron and hole determines the exciton energies, and the center-of-mass motion expresses the movement of the exciton as a whole inside the semiconductor. In bulk, the center-of-mass motion is that of a plane wave, which result in excitonic energy bands. In a dot, the exciton is localized with quantized energy states, and the bands vanish. In the relative coordinate, the exciton envelop function can also have *s*- and *p*- type orbital behavior associating with the different exciton states. The relative motion also reveals information on the exciton Bohr radius, the separation between the electron and hole, which ultimately decides the binding energy of the exciton. Excitons that have large binding energies with Bohr radii on the order of or smaller than the lattice spacing are called Frenkel excitons. Weak binding excitons with Bohr radii larger than the lattice spacing are called Wannier excitons. Our interest lies in the Wannier type specie, commonly occurring in most III-V semiconductors, whose Bohr radii are on the order of the size of the dots leading to localization and quantization of the exciton energy states.

The semiconductor at thermal equilibrium without any optical excitation is said to be at its crystal ground state. In this thesis, we are mostly focusing on the optical transitions between the crystal ground state and the lowest energy exciton state inside a single QD. In this section, we gained a general understanding of the properties of a QD. In the next two sections, we will take a more specific look at various dots studied in our laboratory, namely neutral and charged GaAs IFQDs and InAs SAQDs in semiconductor heterostructures.

## 2.2 Neutral interface fluctuation quantum dots

The first detailed discussion is on the neutral GaAs interface fluctuation quantum dots (IFQDs). These dots are formed spontaneously during MBE growth of the GaAs/Al<sub>0.3</sub>Ga<sub>0.7</sub>As quantum wells in the form of interface monolayer fluctuations [74, 75, 88–91]. The bandgap energy for GaAs is  $E_g = 1.52$  eV, and for Al<sub>0.3</sub>Ga<sub>0.7</sub>As is  $E_g = 1.95$  eV, leading to a bandgap difference of 0.43 eV. The well confinement, as a result of the bandgap difference, is along the [001] growth direction ( $\hat{z}$ ). The lattice mismatch between lattice constants of GaAs and Al<sub>0.3</sub>Ga<sub>0.7</sub>As is less than 0.1 % (5.6533 Å for GaAs and 5.6556 Å for Al<sub>0.3</sub>Ga<sub>0.7</sub>As [92]), which greatly reduces strain in the hetero-interfaces. Instead, the lateral confinement of the QD comes from the monolayer high islands at the quantum well interface caused by growth interruption. Because the fluctuations at the interface occur as a result of thermalization, which is statistical in nature, the spatial distribution and the size of the islands are not well defined. However, as shown in the image obtained by the scanning tunnelling microscope (STM) in Figure 2.4(a) [88], there is a general tendency for the dot to be elongated along the  $[\bar{1}10]$  direction ( $\hat{y} - \hat{x}$ ), and that the average size of the dots is on the order of 60 nm. Even though the lateral confinement is only one monolayer high, it is sufficient to localize the excitonic wavefunction as seen in a near-field scanning optical microscope (NSOM) image in Figure 2.4(b) [93, 94]. Overall, the quantized energy level of the confined exciton in a dot is mostly determined by the stronger confinement along  $\hat{z}$  from the narrow quantum well.

The particular IFQD sample studied is a multi-well sample labelled as NRL-1197King. The structure contains quantum wells with different well widths (28Å, 42Å, 62Å, 85Å, 142Å, and 100nm) grown on a 100nm thick GaAs buffer and capped with another 50nm GaAs layer as illustrated in Figure 2.5(a). The growth interruption procedure is performed between each GaAs/Al<sub>0.3</sub>Ga<sub>0.7</sub>As quantum wells interface. As shown in the STM images in Figure 2.4(a), the monolayer fluctuations form dark regions representing “valleys” (lower monolayers) on the well surface, and bright regions representing “hills” (upper monolayers). In the schematic illustration of the cross-section view of the quantum well in Figure 2.4(c), the upper (lower) monolayer

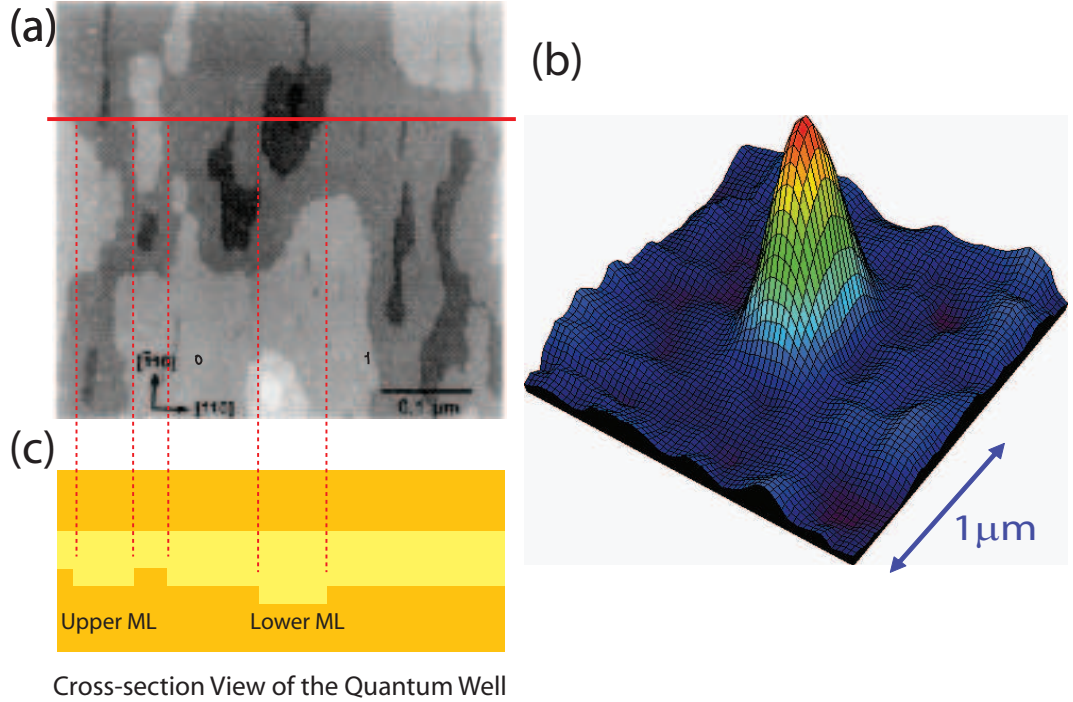


**Figure 2.4:** (a) STM image of the GaAs IFQDs [88] and (b) NSOM image of a single GaAs IFQD (courtesy of Dr. J. R. Guest [93,94]). The vertical and horizontal directions in (a) are  $[\bar{1}10]$  and  $[110]$ , respectively, with a scale of  $0.1 \mu\text{m}$ . (c) represents the cross-section view of the quantum well from (a) with indications of upper and lower monolayers (ML). (d) Photoluminescence (PL) of a  $42\text{\AA}$  quantum well with two distinct exciton energy from the upper and lower monolayers.

regions are associated with narrower (wider) well widths, and hence, has stronger (weaker) confinement. The difference in confinement strength give rise to two distinct excitons energy states in each quantum well corresponding to the two regions, where the higher (lower) energy state is located in the upper (lower) monolayer region. In the  $42\text{\AA}$  quantum well of interest, the energy separations between the lower and upper monolayer excitons is around 10 meV. The inhomogeneous broadening observed in the two main exciton peaks is due to the distribution of dot sizes.

In order to observe exciton states from a single dot, optical excitations and detections are performed through micron-sized apertures in a 100 nm thick aluminum mask deposited on the sample [75]. The advantage of these small apertures is the convenience of studying single dots using a far-field optical setup. The sizes of the apertures range from  $0.5 \mu\text{m}$  to  $25 \mu\text{m}$  as shown in Fig 2.5(b). The locations of each

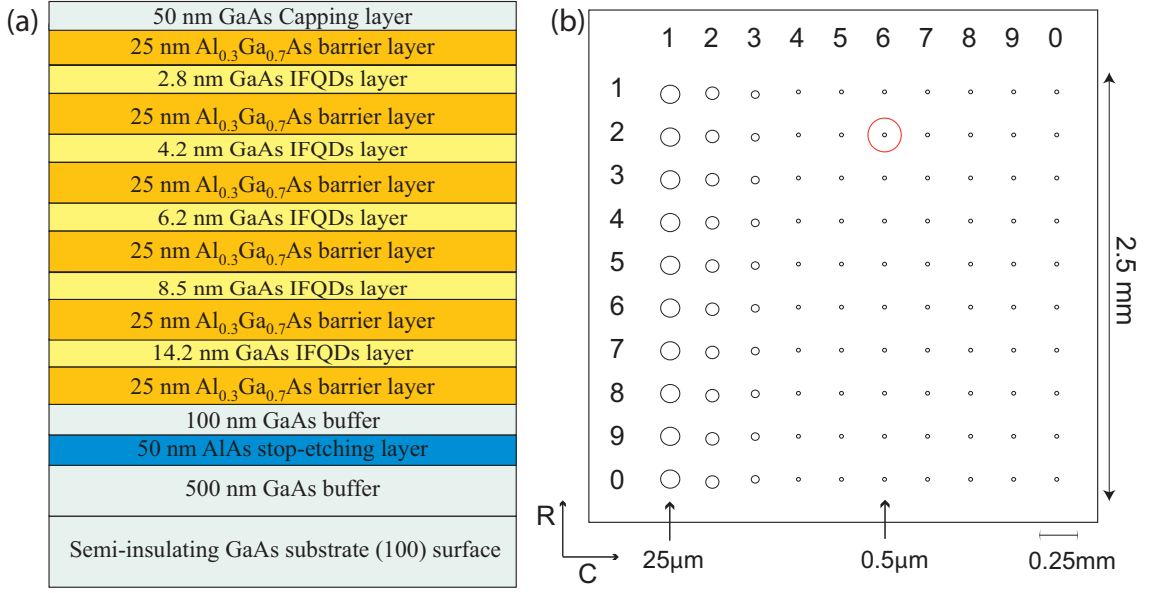


**Figure 2.5:** Neutral GaAs IFQD sample structure and aperture map of NRL-1197King. The individual apertures in (b) are labelled as (r,c) by the row (r) and column (c) positions. The red circle marks aperture (2,6) where the single dot experiments in later chapters are conducted.

aperture are labelled as (r,c) by their row (r) and column (c) positions. The single dot studied in Chapter 4 and 5 is located in aperture (2,6). The average dot density for NRL-1197King is approximately  $100/\text{cm}^2$ . Through the  $25 \mu\text{m}$  apertures, the laser beams are accessible to an order of  $10^5$  dots, making these large apertures ideal for ensemble studies such as that in Figure 2.4(d). For single dot studies, however, the spatial selectivity of the smaller  $0.5 \mu\text{m}$  apertures are needed, through which the number of dots visible to the optical excitation is drastically reduced to around 10-20. Further selectivity is enabled by the spectral resolution of the excitation laser.

In a quantum dot, the energy degeneracy of the HH and LH at  $\vec{k} \approx 0$  is lifted due to confinement and strain. For the GaAs dots, the HH has a higher energy than the LH and becomes the valence band. The lowest energy exciton contains a single *s*-type electron ( $|j, m_j\rangle = |\frac{1}{2}, \pm\frac{1}{2}\rangle$ ) and a *p*-type hole from the HH band ( $|j, m_j\rangle = |\frac{3}{2}, \pm\frac{3}{2}\rangle$ ). There are four possible transition combinations as shown in Figure 2.6(a), of which two are optically allowed ( $\Delta m_j = \pm 1$ ) and two are optically forbidden ( $\Delta m_j = \pm 2$ ) according to angular momentum conservation. Due to asymmetry of the dot shape and spin-dependent exchange interactions [88, 90, 91, 95–99], all four transitions are

non-degenerate in energy resulting in fine structures of the lowest exciton energy state. The optically forbidden states are separated from the optically allowed states by the short-range exchange interaction [99,100] where energy separation is typically around  $160 \mu\text{eV}$  [90]. The splitting within the pair of optically allowed states arise from the long-range exchange interaction [101–103] mostly due to the lateral asymmetry of the dots, which result in a much smaller energy difference of  $25 \mu\text{eV}$  [88]. Instead of being circularly ( $\sigma_+$  and  $\sigma_-$ ) polarized, the optically allowed transitions are orthogonal and linearly polarized ( $\Pi_x$  and  $\Pi_y$ ), parallel ( $[\bar{1}10]$ ) and perpendicular ( $[110]$ ) to the elongation direction, due to the mixing between the two exciton states. In the presence of a magnetic field in the combined Faraday (parallel to the growth direction  $\hat{z}$ ) and Voigt (perpendicular to the growth direction  $\hat{z}$ ) geometries, all four fine structure transitions can be observed [90]. Bound biexcitons are also observed to form in the GaAs dots with a binding energy of  $3.5 \text{ meV}$  [104]. For the concern of this thesis, we focus only on the two optically allowed exciton transitions in zero magnetic field in this sample.

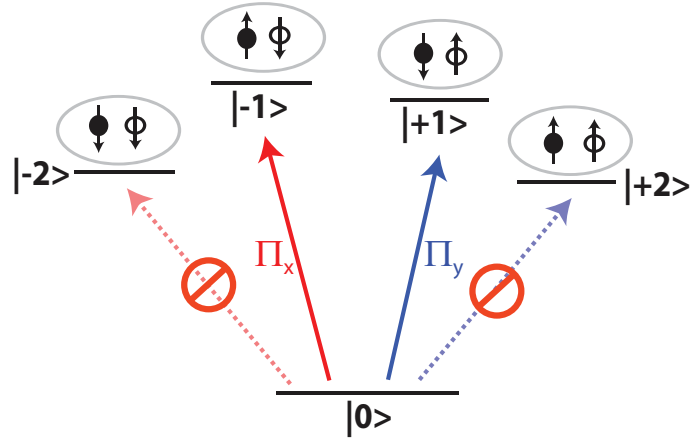


**Figure 2.6:** Energy level diagram in a single neutral GaAs IFQD. The states are labelled by their total angular momentum,  $m_j$ . The middle transitions are the two optically allowed states with horizontal ( $\Pi_x$ ) and vertical ( $\Pi_y$ ) polarizations. The two side transitions are optically forbidden due to angular momentum conservation.

The quantum bit (qubit) in quantum information processing in a GaAs dot is represented by the two-level system of the crystal ground state ( $|0\rangle$ ) and an exciton state ( $|1\rangle$ ). The exciton decay time in the GaAs dots, which sets the limit of the qubit

lifetime, is nominally around 100 ps due to the weak lateral confinement. This short time scale, even with ultrafast excitation pulses, implies that an IFQD is still a long stretch from a practical physical implementation for quantum information processing. However, the large dipole moment of these dots is advantageous for conducting initial studies on the optical properties of similar semiconductor nanostructures, where the obtained knowledge can be readily applied towards the more feasible spin-based systems in SAQDs. A few milestone experiments done on the IFQDs include single qubit rotations through exciton Rabi oscillations [76] and a two-qubit controlled-ROT gate through a biexciton [104]. It has also been shown that coherence exists between two excitons within one dot [105] suggesting the possibility of qubit entanglement. In Chapter 4 and 5, we further demonstrate the potential of the optically driven IFQDs in the coherent control and density matrix tomography experiments.

### 2.3 Charged interface fluctuation quantum dots

The qubit states in a neutral GaAs IFQD include an optically excited state, the exciton. Even though the exciton is overall-neutral, its electron and hole constituents are charged, which are subject to Coulomb interactions with the semiconductor environment. Such interactions are shielded and reduced within the confinement of a QD. However, in the IFQD where the exciton is weakly confined laterally, the Coulomb interactions lead to a short exciton recombination time. Consequently, the desire for a new qubit basis robust against Coulomb disturbances excited a large amount of interest towards the electron spin. The lifetime of the spin up and down states of a single electron spin confined in a QD are not limited by radiative decays. The spin relaxation time in a single dot has been measured to reach orders of milliseconds [106–108]. In addition, the spin coherence time is at least of order 100  $\mu\text{s}$  and mainly influenced by the hyperfine interactions between nuclear spins [109, 110]. Furthermore, the optically driven spin-based system addresses the scalability issue through the potential application of the RKKY scheme for entangling spins in multiple dots [111]. Naturally, a good prototype for the preliminary testing of a optically driven spin-based

qubit system is a singly charged GaAs IFQD, taking advantage of the large optical dipole.

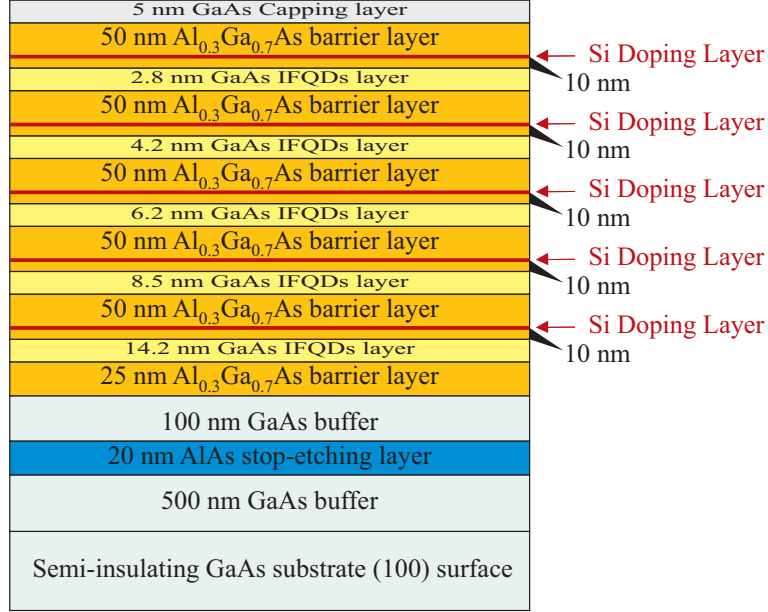


**Figure 2.7:** Charged GaAs IFQD sample structure.

The sample structure of charged GaAs dots is similar to that of the neutral GaAs dots as shown in Figure 2.7. The charging of the dots are accomplished by the introduction of a silicon  $\delta$ -doping layer in the Al<sub>0.3</sub>Ga<sub>0.7</sub>As barrier layer [112]. The excess donor electrons tunnel from the barrier into the quantum well and subsequently trapped by the QD potentials. The doping density controls the level of the Fermi energy, and hence, the average number of electron inside a single dot. The doping density that results in approximately one electron per dot is  $10^{10}/\text{cm}^2$ .

The crystal ground state of the sample is modified by the presence of the confined electron in the QD. In the absence of optical excitations, the states of the QD are defined by the two spin states of the confined electron quantized along the  $\hat{z}$  direction ( $|z\pm\rangle = |\pm\frac{1}{2}\rangle$ ). A bound negatively charged exciton (trion) resulting from the binding of the neutral exciton and the confined electron can be optically generated through on-resonant excitation. The binding energy of the trion is around 3.7 meV. The trion can also be distinguished from the exciton through temperature dependent PL studies, which found that the trion vanished at 37 K while the exciton remains unaffected by



the increasing temperature [113].

The three-particle trion complex has eight possible states with different angular momentum combination of the electrons and heavy hole. However, six of those states involve the electrons in the triplet states due to the Pauli exclusion principle and will not be the focus of this thesis. As a result, the two lowest trion states have the configuration of an electron pair with opposite spin in the singlet states with hole spin pointing either up or down as shown in the energy level diagram in Figure 2.8(a). The exchange interaction is cancelled in the trion system because of the opposite spin pairing configuration of the electrons.

In the absence of magnetic field, angular momentum conservation restricts the excitation of each electron spin ground state to a different trion state. Therefore, the spin ground states are not optically coupled. In order to couple these spin ground states through the trion states, a magnetic field in the Voigt geometry ( $\vec{B} = B_x \hat{x}$ ) is applied. The Hamiltonian,  $\mathbf{H}_{B_x}$ , in the  $|z\pm\rangle \leftrightarrow |t\pm\rangle$  basis of the spin-trion subspace with magnetic field coupling is,

$$\mathbf{H}_{B_x} = \begin{array}{l} \langle z-| \\ \langle z+| \\ \langle t-| \\ \langle t+| \end{array} \begin{bmatrix} |z-\rangle & |z+\rangle & |t-\rangle & |t+\rangle \\ E_{z-} & -g_{e\perp}\mu_B B_x & 0 & 0 \\ -g_{e\perp}\mu_B B_x & E_{z+} & 0 & 0 \\ 0 & 0 & E_{t-} & -g_{h\perp}\mu_B B_x \\ 0 & 0 & -g_{h\perp}\mu_B B_x & E_{t+} \end{bmatrix}, \quad (2.7)$$

where  $\mu_B$  is the Bohr magneton,  $g_{e(h)\perp}$  is the in-plane g-factor for the electron (hole). The new eigenstates of the spin ground states are  $|x\pm\rangle = \frac{1}{\sqrt{2}}(|z+\rangle \pm |z-\rangle)$  with a Zeeman splitting of  $\Delta = 2g_{e\perp}\mu_B B_x$ . Detailed magnetic field dependent studies reveal that the electron in-plane g-factor is  $|g_{e\perp}| = 0.13$  [90, 114]. The trion states, on the other hand, are defined by the hole spin and have negligible g-factor (i. e.  $g_{h\perp} \approx 0$ ). This is due to the large spin-orbital coupling in the quantum well direction leading to little mixing between the LH and HH [90, 115], which in turn pinning the hole spin along the  $\hat{z}$  direction. The final energy diagram of the optically driven spin-based system in the applied Voigt magnetic field is represented by two coupled  $\Lambda$  systems as illustrated in Figure 2.8(b).

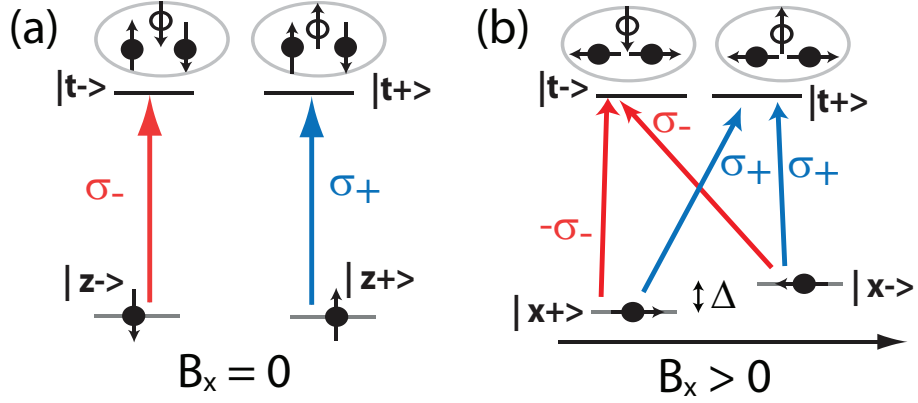


**Figure 2.8:** Energy level diagram in a singly charged GaAs IFQD in the (a) absence and (b) presence of a magnetic field in the Voigt geometry ( $\hat{x}$ ).  $\Delta$  is the Zeeman splitting.

The optical selection rules of this system can be calculated in the irreducible spherical tensors basis, where the optical dipole interaction,  $\vec{\mu} \cdot \vec{E} \propto \vec{r} \cdot \vec{\epsilon}$ , is rewritten as a dot product of two rank-one tensors ( $q = 1, k = -1, 0, 1$ ):

$$\vec{r} \cdot \hat{\epsilon} = -r_{-1}\epsilon_{+1} + r_0\epsilon_0 - r_{+1}\epsilon_{-1}, \quad (2.8)$$

where in general

$$\vec{A} = \sum_k (-1)^k A_{-k} \hat{\epsilon}_k, \quad \vec{A} \cdot \vec{B} = \sum_k (-1)^k A_{-k} B_k, \quad (2.9)$$

and

$$\hat{\epsilon}_{\pm 1} = \mp \frac{\hat{x} + i\hat{y}}{\sqrt{2}} = \mp \hat{\sigma}_{\pm}, \quad \hat{\epsilon}_0 = \hat{z}. \quad (2.10)$$

The interaction density matrix elements are determined by  $\langle m | \vec{r} \cdot \hat{\epsilon} | n \rangle$ , where  $|m\rangle$  and  $|n\rangle$  are the final and initial angular momentum states. The term  $\langle m | \vec{r} \cdot \hat{\epsilon} | n \rangle$  is only nonzero when  $m - n = \pm 1, 0$ . The polarization of each transition in Figure 2.8(b) are listed in Table 2.1

The charged GaAs IFQD sample produces great results in ensemble studies, such as in spectral hole burning experiment in Reference [116], amplitude and phase studies of spin quantum beats [114,117], and the spin coherence control studies in Chapter 6. However, the weak confinement of the GaAs IFQDs is inhibiting studies of single QD. Since the lateral confinement is weak, the electron can easily tunnel in and out of the dot, resulting in unstable single dot spectroscopy and especially unpredictable

Transition	Nonzero element of $\vec{r} \cdot \hat{\epsilon}$	Associated polarization
$ x+\rangle \rightarrow  t+\rangle$ :	$\langle +\frac{3}{2}   -\mathbf{r}_{+1}\epsilon_{-1}   \frac{1}{2} \rangle$	$-\hat{\epsilon}_{+1} = \hat{\sigma}_+$
$ x+\rangle \rightarrow  t-\rangle$ :	$\langle -\frac{3}{2}   -\mathbf{r}_{-1}\epsilon_{+1}   -\frac{1}{2} \rangle$	$-\hat{\epsilon}_{-1} = -\hat{\sigma}_-$
$ x-\rangle \rightarrow  t+\rangle$ :	$\langle +\frac{3}{2}   -\mathbf{r}_{+1}\epsilon_{-1}   \frac{1}{2} \rangle$	$-\hat{\epsilon}_{+1} = \hat{\sigma}_+$
$ x-\rangle \rightarrow  t-\rangle$ :	$\langle -\frac{3}{2}   \mathbf{r}_{-1}\epsilon_{+1}   -\frac{1}{2} \rangle$	$-\hat{\epsilon}_{-1} = \hat{\sigma}_-$

**Table 2.1:** Polarization selection for transitions in the spin-trion system under a magnetic field in the Voigt geometry

time-domain spin coherence studies. In the next section, a practical solution to these issues is discussed in the more strongly confined SAQDs with active electrical gates controlling the charging of the dots.

## 2.4 Gated self-assembled quantum dots

The growth of self-assembled quantum dots (SAQDs) can be classified by the surface energy and lattice mismatch of the semiconductor materials used. The InAs/GaAs SAQDs studied in Chapter 7 are grown by the Stranski-Krastanow (S-K) method which combines layer-by-layer and island growths. The bandgap energy for GaAs is  $E_g = 1.52$  eV, and for InAs is  $E_g = 0.43$  eV, leading to a bandgap difference of 1.09 eV. Hence, the vertical confinement of the InAs SAQDs is more than twice as strong compared to the GaAs IFQDs. The lattice constant is 5.6533 Å for GaAs and 6.0584 Å for InAs. The lattice mismatch is nearly 7%. As more layers of InAs are deposited on the GaAs, the strain buildup results in the spontaneous formation of coherent (defect free) islands on the epitaxial surface. The height of the dots can be controlled through a cap-and-flush procedure which involves partially capping the grown dots with GaAs and then applying an indium flush technique to remove the uncapped portion of the dots [118–120] as illustrated in Figure 2.9(a). This method allows some freedom in engineering the vertical size and, in turn, the optical transition energies inside the dots.

The size of the InAs dots studied in this thesis are 3 nm in the growth direction

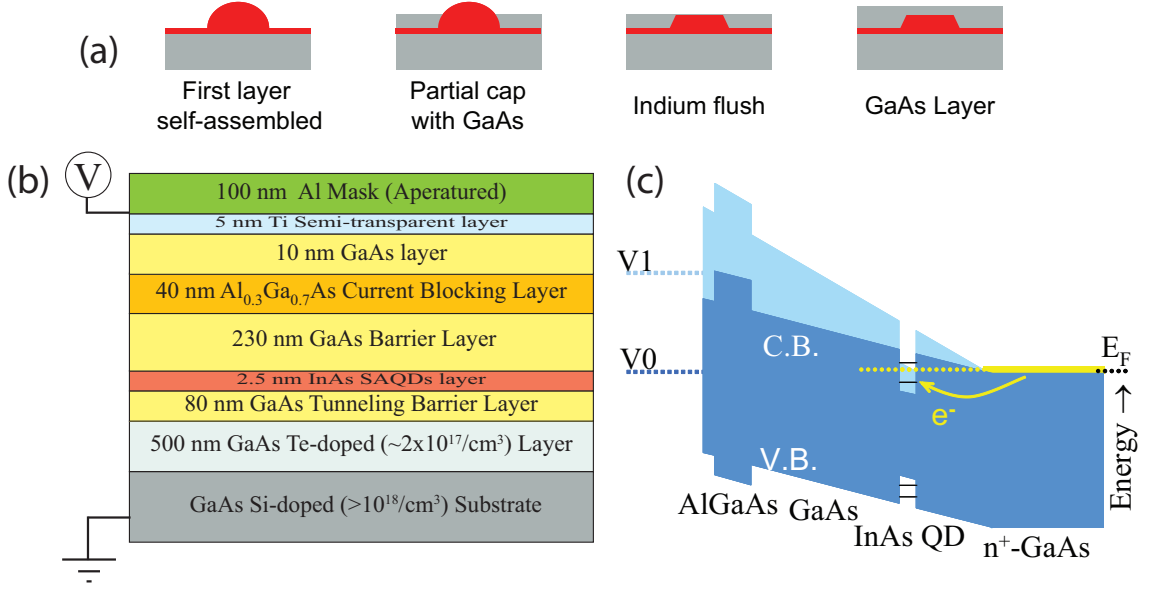


**Figure 2.9:** Charged InAs IFQD sample (a) growth (Courtesy of Dr. Dan Gammon, Naval Research Laboratory), (b) structure and (c) charging scheme, CB and VB stand for conduction band and valence band, respectively.

and around 20 nm laterally. In comparison, the lateral spatial confinement of the SAQDs is much stronger than the monolayer confinement of the IFQDs. The overall stronger confinement in all directions also leads to a smaller optical dipole moment in a SAQD, which has been measured to be around 30 D in one particular dot [82]. Additional studies of multiple dots in the laboratory have extracted dipole moments values ranging from 10-30 D.

The sample structure of the dots are shown in Figure 2.9(b). The n-doped Te layer provides excess electrons for the charging of the QDs. A bias voltage is applied to the sample in a Schottky diode configuration. By changing the voltage across the semiconductor, the applied electric field modifies the dot potential with respect to the Fermi energy level, and controls the precise charging of individual dots as illustrated in Figure 2.9(c). Voltage dependent PL studies of the gated dot sample reveal multiple species of exciton appearing at different voltage ranges. The most prominent features are from neutral excitons ( $X^0$ ), negative trions ( $X^-$ ), positive trions ( $X^+$ ), and doubly negative excitons ( $X^{2-}$ ) [119]. More exotic complexes such as neutral biexcitons ( $XX^0$ ), negative biexcitons ( $XX^-$ ), and triply negative excitons

( $X^{3-}$ ) are also observed. An example of the voltage dependent PL study is presented in Chapter 7. Since our goal is to perform optical manipulation of a single electron spin, we are mainly interested in the voltage range that produces the negative trion. The binding energy between the trion and neutral exciton in the InAs dots ranges from 5-7 meV depending on the dot size.

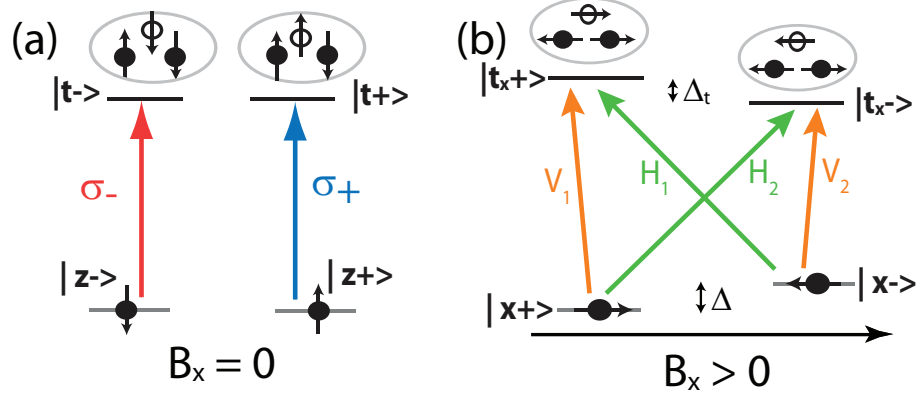


**Figure 2.10:** Energy level diagram in a singly charged InAs SAQD in the (a) absence and (b) presence of a magnetic field in the Voigt geometry ( $\hat{x}$ ).  $\Delta$  is the Zeeman splitting of the electron states and  $\Delta_t$  is the Zeeman splitting of the trion states.

At zero magnetic field, the energy levels of the optical transition in an InAs dot are exactly the same as in an IFQD (Figure 2.10)(a). As we turn on the Voigt magnetic field, the electron states become mixed and their energy degeneracy is lifted by the Zeeman splitting, similar to the IFQD case, as predicted in Equation 2.7. However, in the InAs dots, the hole spin  $g$ -factor is no longer negligible due to considerable LH and HH mixing in the stronger lateral confinement [121], which leads to mixing and splitting of the trion states as well. The new eigenstates of the electron and trion are  $|x\pm\rangle = \frac{1}{\sqrt{2}}(|z+\rangle \pm |z-\rangle)$  and  $|t\pm\rangle = \frac{1}{\sqrt{2}}(|t_x+\rangle \pm |t_x-\rangle)$ . In a magnetic field dependent study, the in-plane electron and hole  $g$ -factors are respectively extracted to be  $|g_{e\perp}| = 0.48$  and  $|g_{h\perp}| = 0.31$  [122]. The polarizations of the optical transitions between the spin and trion states are no longer purely circular due to the mixing of the states. Upon preliminary optical studies of these InAs dots [82, 122], the polarizations for the optical transitions are found to be orthogonally linear as labelled in Figure 2.10(b).

This point of the thesis marks the earlier stage investigation of these InAs dots. Nevertheless, promising results such as the observation of the complex Mollow absorption spectrum [82] and optical spin cooling [122] in a single InAs dot have begun to unveil the vast potential of these well-isolated SAQDs. Recently, great efforts have been devoted to obtaining time-domain signal from a single InAs dot in pursuit of single spin rotation. Concurrently, collaborators in the Naval Research Laboratory are realizing the possibility of a QD molecule to achieve inter-dot entanglement. These near future directions will be discussed briefly in Chapter 7.

## 2.5 Chapter summary

This chapter provided a general theoretical discussion of the semiconductor physics of a QD and a more specific look at the structures, optical properties and roles in quantum information processing of the different QD samples studied in this thesis, namely neutral and charged GaAs IFQDs and voltage gated InAs SAQDs. In the next four chapters, demonstrations of optical coherent controls on the different QDs will be elaborated through various experimental techniques. Chapters 4 and 5 will prove the ability of a single GaAs IFQD to maintain and propagate coherent information in the density matrix tomography measurement. Chapter 6 will extend the coherent control idea to an ensemble of charged GaAs IFQDs. Chapter 7 will deal with the current accomplishments and future goals in the InAs SAQDs.

## CHAPTER 3

### Theory and experimental methods of nonlinear spectroscopy

While the photoluminescence (PL) technique is excellent for the initial characterization of the energy states of a quantum system, due to the far off-resonant excitation condition the signal detected is limited to that of recombination emission. In order to truly explore the richness of higher order nonlinear optical properties in a quantum system, near or on-resonant excitations are often required.

In a system with spherical spatial symmetry such as an atom, it is possible to still use luminescence as a means of background-free detection, where the emission signal is collected away from the excitation beam path. It is, however, more difficult to do so in a semiconductor system, where the artificially grown structure usually limits the physical separation between the paths of the excitation beams and the signal, making background-free luminescence detection nearly impossible. Recently, through the clever use of a microcavity, background-free luminescence signals from quantum dots (QDs) were obtained by exciting through the non-cavity mode and detecting in the cavity mode direction [123]. This setup enables the rare observation of the emission spectra of the Mollow triplets in semiconductor structures. Nevertheless, for general semiconductor systems that are not specially engineered for such a task, more encompassing techniques are adapted.

In experimental works presented in this thesis, two particular techniques are used that allow for differential signal detection, even when the signal is propagating in the same direction as the excitation beams. One such technique is phase-sensitive homodyned differential transmission (DT). This is a pump-probe method that measures

the nonlinear signals of the quantum system. The two optical beams are modulated such that the co-propagating excitation beam enhances the homodyne signal while suppressing the undesired background signal. Another technique is voltage modulated absorption, which utilizes the electrically induced DC Stark shift to measure directly the absorption profile of a quantum system. The voltage modulation method was used to obtain the complex Mollow absorption spectrum [82], which contains different and richer physics not visible in its emission counterpart.

In this chapter, we begin by introducing the density matrix master equations (DMMEs) for the two-level and three-level  $\Lambda$  systems in the normal and field representation pictures. The DMME describe both linear and nonlinear responses of an optical system at the microscopic quantum level. The close relationship between these density matrix elements and the macroscopic radiating signal fields are discussed using the Maxwell-Bloch equations. And finally, we conclude the chapter by describing in detail the methodologies of the differential signal detection technique used in relevant experiments presented in this thesis.

### 3.1 Master equations of density matrix elements

As presented in Chapter 2, due to the three dimensional confinement provided by the QD structure, the density of states exhibit discrete  $\delta$ -function-like features similar to that of atomic systems. Therefore, it is valid to approximate the optical transitions involved in the exciton and trion systems inside a QD using simple two-level and three-level formalism, respectively.

The following discussion concentrates on the general case of the three-level  $\Lambda$  system in the presence of a single optical field. The general case for a two-level system can be recovered by setting appropriate terms in the three-level equations to zero. In the normal representation, which is the laboratory frame, an arbitrary superposition state  $|\psi\rangle$  of a three-level is written as

$$|\psi\rangle = a_1|1\rangle + a_2|2\rangle + a_3|3\rangle, \quad (3.1)$$

where the  $a_n$ 's are normalized state probability amplitudes for state  $|n\rangle$ . The optical



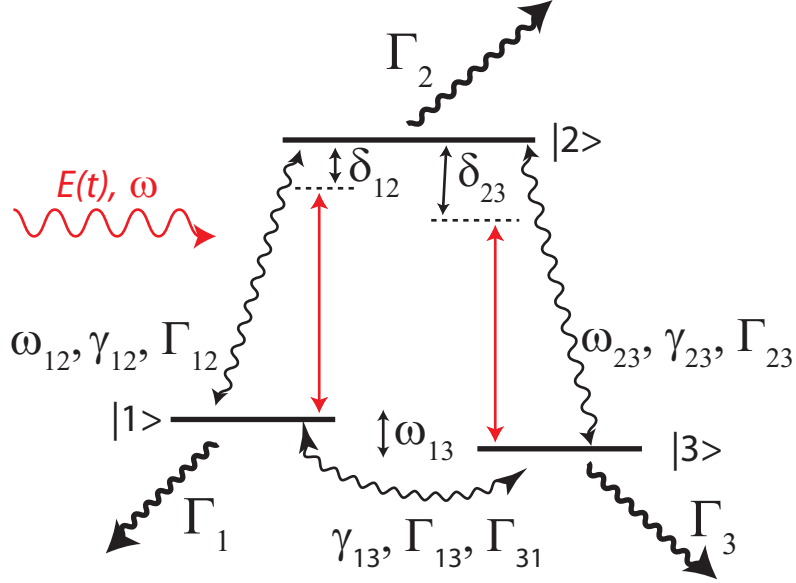


**Figure 3.1:** Diagram of a general open three-level  $\Lambda$  system.  $\omega_{12}$  ( $\omega_{23}$ ) is the transition frequency between states  $|2\rangle$  and  $|1\rangle$  ( $|3\rangle$ ).  $\omega_{13} = \omega_{23} - \omega_{12}$  is the frequency difference between states  $|1\rangle$  and  $|3\rangle$ .  $\mathbf{E}(t)$  is the excitation field with frequency  $\omega$ .  $\delta_{12(23)} = \omega_{12(23)} - \omega$  is detuning of the field from the state  $|1\rangle$  ( $|3\rangle$ ).  $\Gamma_{ij}$  ( $\gamma_{ij}$ ) is the population decay (decoherence) rate between states  $|i\rangle$  and  $|j\rangle$  for a closed system.  $\Gamma_n$  is the population decay of state  $|n\rangle$  in an opened system.

field in this representation is  $\vec{\mathbf{E}}(t) = \frac{1}{2} [\hat{\mathbf{e}}E(t)e^{-i(\omega t - \vec{\mathbf{k}} \cdot \vec{\mathbf{r}})} + c.c.]$ , where “*c.c.*” denotes the complex conjugate term, and  $\hat{\mathbf{e}}$  is the polarization direction of the field. Since the QDs under study satisfy the condition of  $\vec{\mathbf{k}} \cdot \vec{\mathbf{r}} \ll 1$  for the dipole approximation, the value of the spatial component,  $e^{i\vec{\mathbf{k}} \cdot \vec{\mathbf{r}}}$ , can be set to unity. The Schrödinger equation for the  $\Lambda$  system with  $|1\rangle$  and  $|3\rangle$  as ground states is then

$$i\hbar\dot{\vec{a}} = \mathbf{H}\vec{a}, \quad \mathbf{H} = \hbar \begin{bmatrix} -\omega_{12} & X_{12} & 0 \\ X_{21} & 0 & X_{32} \\ 0 & X_{23} & -\omega_{23} \end{bmatrix}, \quad (3.2)$$

where  $X_{ij} = -\frac{\boldsymbol{\mu}_{ij} \cdot \vec{\mathbf{E}}(t)}{\hbar} = \chi_{ij}e^{-i\omega t} + c.c.$  and  $\boldsymbol{\mu}_{ij}$  is the dipole moment between transition  $i \leftrightarrow j$ . The energy of the excited state  $|2\rangle$  is arbitrarily set to zero for convenience (i.e.  $\omega_2 = 0$ ), and the transition frequency between state  $|1\rangle$  and  $|2\rangle$  is  $\omega_{12(23)} = |\omega_2 - \omega_{1(3)}|$ .

The probability amplitude picture is great for modelling and understanding the underlying physics behind optical excitations. However, in this picture, it is difficult to take into account decay processes if the specific detail of the interactions leading

to decay is unknown. Therefore, the amplitude picture is in general only useful for describing the evolution dynamics of a pure state system. In order to calculate the actual signal output from a realistic quantum system, we must take into account the associated decay and decoherence times and the possibility of a mixed state system. To do so, we must look into the density matrix picture. The general expression for the equation of motion of the density matrix is

$$i\hbar\dot{\rho} = [\mathbf{H}, \rho] + i\hbar\dot{\rho}|_{relaxation}, \quad (3.3)$$

where  $\mathbf{H}$  is the Hamiltonian. For the  $\Lambda$  system represented in Figure 3.1, the expanded equations of motion for all the density matrix elements in the normal density representation are

$$\begin{aligned} \dot{\rho}_{11} &= -iX_{12}\rho_{21} + iX_{12}\rho_{12} + \Gamma_{21}\rho_{22} - (\Gamma_{13} + \Gamma_1)\rho_{11} + \Gamma_{31}\rho_{33} \\ \dot{\rho}_{22} &= iX_{12}\rho_{21} - iX_{12}\rho_{12} - iX_{23}\rho_{23} + iX_{23}\rho_{32} - \Gamma_2\rho_{22} \\ \dot{\rho}_{33} &= -iX_{12}\rho_{23} + iX_{12}\rho_{32} + \Gamma_{23}\rho_{22} - (\Gamma_{31} + \Gamma_3)\rho_{33} + \Gamma_{13}\rho_{11} \\ \dot{\rho}_{12} &= \dot{\rho}_{21}^* = -iX_{12}[\rho_{22} - \rho_{11}] + iX_{23}\rho_{13} - (\gamma_{21} - i\omega_{12})\rho_{12} \\ \dot{\rho}_{23} &= \dot{\rho}_{32}^* = iX_{23}[\rho_{22} - \rho_{33}] - iX_{12}\rho_{13} - (\gamma_{23} + i\omega_{23})\rho_{23} \\ \dot{\rho}_{13} &= \dot{\rho}_{31}^* = -iX_{12}\rho_{23} + iX_{23}\rho_{12} - [\gamma_{13} - i(\omega_{12} - \omega_{23})]\rho_{13}. \end{aligned} \quad (3.4)$$

The decay parameter  $\Gamma_{ij}$  ( $\gamma_{ij}$ ) is the population decay (decoherence) rate between states  $|i\rangle$  and  $|j\rangle$ . These doubly indexed decay parameters characterize the relaxation within the closed three-level  $\Lambda$  system.  $\Gamma_n$  denotes the population decay of state  $|n\rangle$  in an open system. Since the QDs studied in the work of this thesis are basically closed quantum systems, the open system decay terms are set to zero in later calculations.

In the normal representation, the field related term  $X_{ij}$  contains oscillations of  $e^{-i\omega t}$  and  $e^{i\omega t}$  associated with  $\chi_{ij}$  and  $\chi_{ij}^*$ , respectively. Solving the density matrix equations with these rapid oscillating phases can sometimes be complicated. To simplify the process, it is more convenient to remove these oscillations by going into the rotating frame of the quantum system (interaction picture) or the field (field interaction picture). Since we are only concerned about single optical field excitations here, it is appropriate to convert to the field interaction picture.

In the field interaction picture, the ground state probability amplitudes,  $a_1$  and  $a_3$ , in Equation 3.1 are rewritten as products of an amplitude component and an oscillating component with the optical field frequency,  $\omega$ ,

$$\begin{aligned} a_1 &= c_1 e^{i\omega t} \\ a_2 &= c_2 \\ a_3 &= c_3 e^{i\omega t}. \end{aligned} \quad (3.5)$$

By applying the substitutions in Equation 3.5 appropriately to Equation 3.4, the master equations in terms of  $\rho_{ij}^{FI} = c_j^* c_i$  are,

$$\begin{aligned} \dot{\rho}_{11}^{FI} &= -iX_{12}e^{-i\omega t}\rho_{21}^{FI} + iX_{12}e^{i\omega t}\rho_{12}^{FI} + \Gamma_{21}\rho_{22}^{FI} - (\Gamma_{13} + \Gamma_1)\rho_{11}^{FI} + \Gamma_{31}\rho_{33}^{FI} \\ \dot{\rho}_{22}^{FI} &= iX_{12}e^{-i\omega t}\rho_{21}^{FI} - iX_{12}e^{i\omega t}\rho_{12}^{FI} - iX_{23}e^{-i\omega t}\rho_{23}^{FI} + iX_{23}e^{i\omega t}\rho_{32}^{FI} - \Gamma_2\rho_{22}^{FI} \\ \dot{\rho}_{33}^{FI} &= -iX_{12}e^{-i\omega t}\rho_{23}^{FI} + iX_{12}e^{i\omega t}\rho_{32}^{FI} + \Gamma_{23}\rho_{22}^{FI} - (\Gamma_{31} + \Gamma_3)\rho_{33}^{FI} + \Gamma_{13}\rho_{11}^{FI} \\ \dot{\rho}_{12}^{FI} &= \dot{\rho}_{21}^{FI*} = -iX_{12}e^{-i\omega t}[\rho_{22}^{FI} - \rho_{11}^{FI}] + iX_{23}e^{-i\omega t}\rho_{13}^{FI} - (\gamma_{21} - i\delta_{12})\rho_{12}^{FI} \\ \dot{\rho}_{23}^{FI} &= \dot{\rho}_{32}^{FI*} = iX_{23}e^{i\omega t}[\rho_{22}^{FI} - \rho_{33}^{FI}] - iX_{12}e^{i\omega t}\rho_{13}^{FI} - (\gamma_{23} + i\delta_{23})\rho_{23}^{FI} \\ \dot{\rho}_{13}^{FI} &= \dot{\rho}_{31}^{FI*} = -iX_{12}e^{-i\omega t}\rho_{23}^{FI} + iX_{23}e^{i\omega t}\rho_{12}^{FI} - [\gamma_{13} - i(\delta_{12} - \delta_{23})]\rho_{13}^{FI}, \end{aligned} \quad (3.6)$$

where  $\delta_{12(23)} = \omega_{12(23)} - \omega$ . Further simplification can be achieved by applying the rotating wave approximation (RWA). This approximation is applied to the terms  $X_{ij}e^{i\omega t} = \chi_{ij} + \chi_{ij}^*e^{i2\omega t}$  and  $X_{ij}e^{-i\omega t} = \chi_{ij}e^{-i2\omega t} + \chi_{ij}^*$ . The validity of the approximation lies in that the frequency of the rapid oscillating terms are much larger than that evolution time scales of the density matrix elements (i.e.  $|\chi_{ij}/2\omega| \ll 1$  and  $|\delta_{ij}/2\omega| \ll 1$ ). If these conditions are satisfied, then the terms  $e^{\pm i2\omega t}$  average to zero in a short time scale and can be neglected. The density matrix master equations with RWA are

$$\begin{aligned} \dot{\rho}_{11}^{FI} &= -i\chi_{12}^*\rho_{21}^{FI} + i\chi_{12}\rho_{12}^{FI} + \Gamma_{21}\rho_{22}^{FI} - (\Gamma_{13} + \Gamma_1)\rho_{11}^{FI} + \Gamma_{31}\rho_{33}^{FI} \\ \dot{\rho}_{22}^{FI} &= i\chi_{12}^*\rho_{21}^{FI} - i\chi_{12}\rho_{12}^{FI} - i\chi_{23}^*\rho_{23}^{FI} + i\chi_{23}\rho_{32}^{FI} - \Gamma_2\rho_{22}^{FI} \\ \dot{\rho}_{33}^{FI} &= -i\chi_{12}^*\rho_{23}^{FI} + i\chi_{12}\rho_{32}^{FI} + \Gamma_{23}\rho_{22}^{FI} - (\Gamma_{31} + \Gamma_3)\rho_{33}^{FI} + \Gamma_{13}\rho_{11}^{FI} \\ \dot{\rho}_{12}^{FI} &= \dot{\rho}_{21}^{FI*} = -i\chi_{12}^*[\rho_{22}^{FI} - \rho_{11}^{FI}] + i\chi_{23}^*\rho_{13}^{FI} - (\gamma_{21} - i\delta_{12})\rho_{12}^{FI} \\ \dot{\rho}_{23}^{FI} &= \dot{\rho}_{32}^{FI*} = i\chi_{23}[\rho_{22}^{FI} - \rho_{33}^{FI}] - i\chi_{12}\rho_{13}^{FI} - (\gamma_{23} + i\delta_{23})\rho_{23}^{FI} \\ \dot{\rho}_{13}^{FI} &= \dot{\rho}_{31}^{FI*} = -i\chi_{12}^*\rho_{23}^{FI} + i\chi_{23}\rho_{12}^{FI} - [\gamma_{13} - i(\delta_{12} - \delta_{23})]\rho_{13}^{FI}. \end{aligned} \quad (3.7)$$

In the rest of this thesis, all calculations are completed using this set of master equations in the field interaction representation (Equation 3.7). For simplicity, the superscript “FI” will be omitted in future chapters.

Exact solutions to these density matrix equations are in general not available. However, there are always assumptions one can make to obtain valuable information from these density matrix master equations without solving them completely. For the case of time independent  $\chi_{ij}$ ’s, the time derivative on the left hand side can be set to zero in a steady state approximation, and the calculation process is reduced to coupled algebraic equations instead of coupled differential equations. For a more general treatment regardless of the form of  $\chi_{ij}$ ’s, a perturbation approach with respect to the field is used. Basically, in the perturbation approach, any density matrix elements ( $\rho_{ij}$ ) can be written as

$$\rho_{ij} = \sum_n \rho_{ij}^{(n)}, \quad \rho_{ij}^{(n)} \propto \sum_{p.c.} \left( \kappa_{p.c.} \prod_n E_k \right), \quad (3.8)$$

where  $n$  denotes the  $n$ th order in the perturbation chain,  $\kappa_{p.c.}$  is a value determined by the dipole and polarization dot-product, and “p.c.” means all possible combinations of  $n$  fields. For example, for  $n = 2$ ,  $\sum_{p.c.} \prod_n E_k = \kappa_{11} E_1 E_1 + \kappa_{22} E_2 E_2 + \kappa_{12} E_1 E_2 + \kappa_{21} E_2 E_1$ . The higher order density matrix elements ( $\rho^{(n)}$ ) can be solved from lower order density matrix elements ( $\rho^{(n-1)}$ ) by using simple perturbation theory calculations. The higher the number of terms used in the summation, the more precise  $\rho_{ij}$  will become. In the weak field regime, a third order ( $n = 3$ ) approximation of the density matrix elements is sufficient to accurately describe the dynamics of the quantum system. Even in the strong field regime, where an exact treatment to Equation 3.7 is required to see phenomena such as Rabi oscillations, the third order approximation can still provide extremely insightful information on the quantum system. Subsection 6.1.2 in Chapter 6 gives an in depth discussion and comparison between the exact solution and the third order approximation of a three-level  $\Lambda$  system.

### 3.2 Maxwell-Bloch equation

The density matrix elements in previous section describe the evolution dynamics

of the system quantum mechanically. However, none of these quantities are directly measurable. The experimentally obtainable value of a given physical observable in a quantum system is actually the expectation value of the related quantum operator. The expectation value depends highly on the condition of the quantum state, thus gaining insightful information on the density matrix elements in Equation 3.7 is important.

In the optical measurements in this thesis, the physical observable of interest is the dipole moment,  $\boldsymbol{\mu}$ . The dipole moment of a single quantum system leads to an overall macroscopic polarization,  $\vec{\mathbf{P}}$ , which in turn produces radiating electromagnetic fields that can be measured in a laboratory. The macroscopic polarization has the expression of total dipole moment per unit volume,

$$\vec{\mathbf{P}} = \sum_k \langle \boldsymbol{\mu}^k \rangle = \sum_k \text{Tr}(\boldsymbol{\mu}^k \boldsymbol{\rho}) = \sum_k \sum_{ij} (\boldsymbol{\mu}_{ij}^k \rho_{ji} + c.c.) \quad (3.9)$$

where the sum over  $k$  depends on the spatial locations of the dipoles within the unit volume, and  $i \neq j$ . In a nonlinear medium with instantaneous response, the polarization can be broken down into contributions from different orders of nonlinear susceptibility of the medium,

$$\vec{\mathbf{P}} = \sum_i \epsilon_0 \boldsymbol{\chi}^{(1)} \vec{\mathbf{E}}_i + \sum_{ij} \epsilon_0 \boldsymbol{\chi}^{(2)} \vec{\mathbf{E}}_i \vec{\mathbf{E}}_j + \sum_{ijk} \epsilon_0 \boldsymbol{\chi}^{(3)} \vec{\mathbf{E}}_i \vec{\mathbf{E}}_j \vec{\mathbf{E}}_k + \dots, \quad (3.10)$$

where  $\epsilon_0$  is the permittivity of free space. The  $\boldsymbol{\chi}^{(n)}$ 's here represent the  $n$ th order of nonlinear susceptibility, and are in general tensors. They are closely related to the density matrix elements. The relationship is apparent by comparing same order terms in Equation 3.10 and Equation 3.9 with the substitution of Equation 3.8.

The real part of the first order susceptibility,  $\boldsymbol{\chi}^{(1)}$  leads to the linear refractive index,  $n^2 = 1 + \boldsymbol{\chi}^{(1)}$ , and the imaginary part leads to linear absorption. The second order term,  $\boldsymbol{\chi}^{(2)}$ , is responsible for phenomena such as second harmonic generation, sum frequency generation and difference frequency generation. There are a wide range of applications using the second order effect including tunable laser sources such an optical parametric amplifier (OPA) and optical parametric oscillator (OPO). Our optical measurement technique, which is a specific form of the four-wave mixing

(FWM), relies on the third order susceptibility,  $\chi^{(3)}$ . Other well-known applications associated with  $\chi^{(3)}$  are third harmonic generation, intensity dependent refractive index effects, and stimulated Raman scattering effects.

The quantum mechanically derived polarization,  $\vec{P}$ , is related to the classical signal field,  $\vec{E}_{sig}$ , through Maxwell's equations where  $\vec{P}$  enters in as a source term. Maxwell's equations for the case of no free charges ( $\rho = 0$ ) and no current sources ( $\vec{J} = 0$ ) are

$$\nabla \cdot (\epsilon \vec{E}_{sig} + \vec{P}) = 0, \quad (3.11)$$

$$\nabla \times \vec{E}_{sig} = -\frac{\partial \vec{B}}{\partial t}, \quad (3.12)$$

$$\nabla \times \vec{B} = \mu \frac{\partial (\epsilon \vec{E}_{sig} + \vec{P})}{\partial t}, \quad (3.13)$$

$$\nabla \cdot \vec{B} = 0, \quad (3.14)$$

where  $\epsilon$  and  $\mu$  are the permittivity and permeability in a medium. By taking the curl of the left-hand side of Equation 3.12 ( $\nabla \times \nabla \times \vec{E}_{sig}$ ) and substituting Equation 3.13 to the right-hand side, we obtain an expression for the relationship between  $\vec{E}_{sig}$  and  $\vec{P}$ :

$$\nabla(\nabla \cdot \vec{E}_{sig}) - \nabla^2 \vec{E}_{sig} = -\frac{1}{c^2} \frac{\partial^2 \vec{E}_{sig}}{\partial t^2} - \frac{1}{c^2 \epsilon} \frac{\partial^2 \vec{P}}{\partial t^2}, \quad (3.15)$$

where  $c = \frac{1}{\sqrt{\mu\epsilon}}$  is the speed of light. Equation 3.15 is the Maxwell-Bloch equation.

In general, it is not trivial to solve the Maxwell-Bloch equation exactly. However, if certain preconditions are assumed, then some approximations can be made to allow for analytical solutions of the differential equation. The first approximation is that  $\nabla \cdot \vec{E}_{sig} \approx 0$ , which is valid in vacuum, or when transverse effects due to bound charges in a medium is negligible. Without transverse effects, the signal field maintains its propagating direction, say  $\hat{z}$ , and can be represented by plane waves. The double spatial derivative in Equation 3.15 is then simplified to only contain the  $z$  component:

$$\frac{\partial^2 \vec{E}_{sig}}{\partial z^2} = \frac{1}{c^2} \frac{\partial^2 \vec{E}_{sig}}{\partial t^2} + \frac{1}{c^2 \epsilon} \frac{\partial^2 \vec{P}}{\partial t^2}. \quad (3.16)$$

We can assume a solution of the form  $\vec{E}_{sig}(\vec{P}) = \tilde{E}(\tilde{P})e^{-i(\omega t - kz)} + c.c..$  For convenience, we concentrate only on the  $\tilde{E}(\tilde{P})$  term since the complex conjugate term

can be solved in exactly the same manner. Substituting the solution form into Equation 3.16 gives time derivatives of the field envelopes that are proportional to  $\frac{\partial^2 \tilde{\mathbf{E}}_{sig}}{\partial t^2}$ ,  $\frac{\partial \tilde{\mathbf{E}}_{sig}}{\partial t}$ ,  $\frac{\partial^2 \tilde{\mathbf{P}}}{\partial t^2}$  and  $\frac{\partial \tilde{\mathbf{P}}}{\partial t}$ . For most optical fields, such as those used in our experiment, the field envelopes vary much slower in time than the optical oscillations,  $\omega^{-1}$ , and these terms are all negligible as a result in this slowly varying envelope approximation (SVEA). Furthermore, the spatial field envelopes are slowly varying compared to the optical wavelength  $\lambda = 2\pi/k$ , and the second order spatial derivative term  $\frac{\partial^2 \tilde{\mathbf{E}}_{sig}}{\partial z^2}$ , can also be omitted using SVEA. The final wave equation with the above applied simplifications is then

$$i2k \frac{\partial \tilde{\mathbf{E}}_{sig}}{\partial z} - k^2 \tilde{\mathbf{E}}_{sig} = -\frac{\omega^2}{c^2} \tilde{\mathbf{E}}_{sig} + -\frac{\omega^2}{c^2 \epsilon} \tilde{\mathbf{P}}. \quad (3.17)$$

Since  $\omega = kc$ , Equation 3.17 has an even more simplified form of

$$\frac{\partial \tilde{\mathbf{E}}_{sig}}{\partial z} = i \frac{k}{2\epsilon} \tilde{\mathbf{P}}. \quad (3.18)$$

For the case of our semiconductor QD samples, Equation 3.18 might not describe the complete picture in these complicated structures. For example, in the case where a single dot is considered, we can no longer use plane waves to approximate the fields in solving Equation 3.15 since the field propagation profile is governed by the dipole radiation pattern. However, these complications only affect the angular distribution of the propagating fields. The most important information that we are interested in is the interaction between the quantum system and the optical fields. This information is embedded in the density matrix elements and is the same across the angular distribution of the field in the case of a single dot. Therefore, Equation 3.18 is sufficient in terms of providing a helpful insight to our measured signal.

### 3.3 Differential transmission detection using phase-sensitive optical modulation

In a practical experimental measurement, the signal fields and the excitation fields often overlap in propagation direction. In single dot measurements, diffraction from the sub-micron apertures erases the information of the original propagation directions

of the optical beams. Even in ensemble type measurement where apertures are absent, scattering from the sample itself still causes the same issue. It is useful then, to devise detection techniques that will enable the detection of weak signal fields in the presence of strong excitation fields. In this section, one such method discussed in detail is the phase-sensitive optical modulation, which is used in the main experiments in this thesis. In Chapter 7, a similar method will be discussed, which uses the DC Stark shift as a form of modulation.

The phase-sensitive optical modulation method in general uses a two-beam pump-probe configuration. It is essentially a specific form of four-wave mixing technique. In order to understand the more complicated setup used in the experiment which modulates both pump and probe beams, we start with the more straightforward concept of single beam modulation. In the simplest picture of a standard pump-probe experiment, the pump beam usually has a stronger optical power than the probe beam. The strong pump beam interacts with and excites the quantum system leading to changes in the complex refraction index of the excited medium, which is determined by the matrix elements in Section 3.1. The change in the real component of the refraction index produces a phase shift in the propagating field, whereas the change in the imaginary component of the index affects the absorption, and hence, attenuation of the field. In turn, these changes affect the propagation of the optical field of the probe beam, which is kept at a much weaker power and does not impose further perturbation on the quantum system. For a system with a weak optical response, isolating the small changes in the probe beam from the background of the original excitation fields can be a difficult task, because the signal is overwhelmed by contributions from other sources such as scattering and diffraction. However, if we modulate the amplitude of the pump beam at a frequency of  $\Omega$ , this modulation will be transferred through the quantum system and, in turn, appear in the probe beam. The signal extracted from the probe beam at this modulation frequency is a direct measurement of the interaction between the pump field and the quantum system. The single modulation signal can simply be considered as the differential signal between the two conditions of pump on and pump off.



In order to pursue a complete treatment of optical modulation mathematically, we need to solve the density matrix equations by including the modulations in the electric field terms [116]. However, for the purpose of understanding the basic ideal of modulation, we can model the single modulation scheme with a simple rate equation picture, with  $Q$  representing the quantity of interest in the measurement

$$\dot{Q} = \frac{I_1}{2}(1 + \alpha \cos \Omega t) - \Gamma Q, \quad (3.19)$$

where  $I_1$  is the intensity of the pump field,  $\alpha$  is the modulation depth where  $\alpha = 1$  represents 100% modulation,  $\Omega$  is the modulation frequency, and  $\Gamma$  is any characteristic decay rate in the quantum system. The solution to the rate equation in Equation 3.19 has the form  $Q = Q_0 + Q_1 \cos \Omega t + Q_2 \sin \Omega t$ , where  $Q_0 = \frac{I_0}{2\Gamma}$ ,  $Q_1 = \frac{\Gamma I_0}{2(\Omega^2 + \Gamma^2)}$ ,  $Q_2 = \frac{\Gamma I_0}{2(\Omega^2 + \Gamma^2)}$ . A more compact form of the solution can be written as

$$Q = \frac{I_1}{2} \left[ \frac{1}{\Gamma} + \cos(\Omega t - \phi_{mod}) \right], \quad (3.20)$$

where

$$\phi_{mod} = \tan^{-1} \frac{Q_1}{Q_2} = \tan^{-1} \frac{\Omega}{\Gamma}. \quad (3.21)$$

The value  $\phi_{mod}$  is a measurable quantity in a phase-sensitive experiment. It represents the electronic phase shift between the original modulation reference frequency and the modulated signal. For a decay rate much larger than the modulation frequency ( $\frac{\Omega}{\Gamma} \rightarrow 0$ ), the phase,  $\phi_{mod}$ , approaches 0, meaning there is no considerable phase lag between the modulation reference and the signal. However, when the modulation frequency is comparable to the decay rate ( $\frac{\Omega}{\Gamma} \rightarrow 1$ ), the phase shift will be  $\phi_{mod} \sim \frac{\pi}{4}$ . Likewise, for  $\frac{\Omega}{\Gamma} \rightarrow \infty$ , the signal is completely out of phase from the original reference with a phase shift of  $\phi_{mod} = \frac{\pi}{2}$ . The well-defined relationship between these three quantities in Equation 3.21 can be utilized to extract useful relaxation time scales in a quantum system, such as the spin relaxation rate in a single quantum dot [116].

In the case where the signal and the modulated pump beams cannot be spatially separated, such as in the detection configurations in Chapters 4- 6, modulation on both pump and probe beams are required to isolate the signal. Returning to the simple rate equation expression, the mathematical form for the the double modulation

scheme where the pump beam ( $I_1$ ) is modulated at  $\Omega_1$  and the probe ( $I_2$ ) at  $\Omega_2$  is simply  $Q$  with an additional modulation,

$$Q = \frac{I_1 I_2}{4} \left[ \frac{1}{\Gamma} + \cos(\Omega_1 t - \phi) \right] (1 + \cos \Omega_2 t)$$

$$= \frac{I_1 I_2}{4} \left[ \frac{1}{\Gamma} (1 + \cos \Omega_2 t) + \cos(\Omega_1 t - \phi_{mod}) + \frac{1}{2} \cos(\Omega_+ t - \phi_{mod}) + \frac{1}{2} \cos(\Omega_- t - \phi_{mod}) \right], \quad (3.22)$$

where  $\Omega_{\pm} = \Omega_1 \pm \Omega_2$  are the sum and difference frequencies. As long as  $\Omega_{\pm} \neq \Omega_1, \Omega_2$ , the differential signal can be detected either at the sum ( $\Omega_+$ ) or difference ( $\Omega_-$ ) frequency of the original modulations where background signals due to the pump or the probe fields are eliminated.

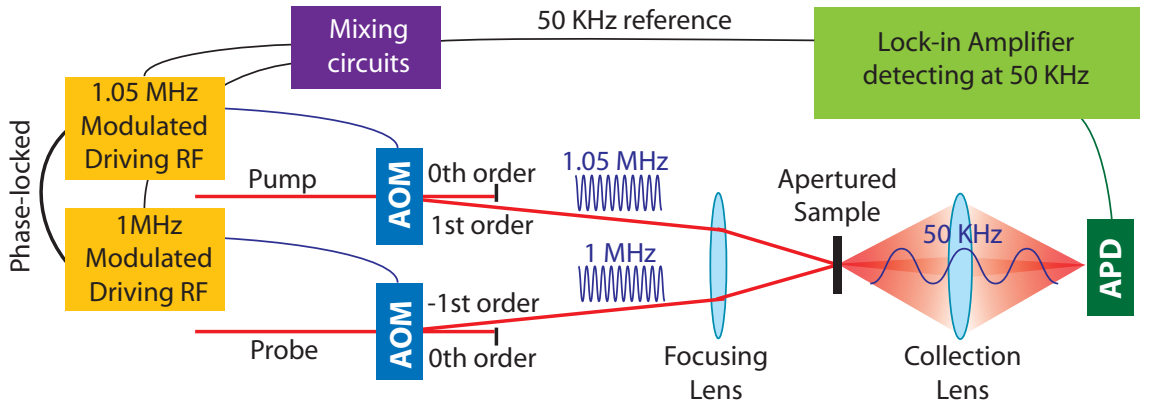


**Figure 3.2:** Diagram of the double optical modulation setup.

In the actual experimental setup shown in Figure 3.2, the modulations on the pump and probe beams are applied by using IntraAction<sup>TM</sup> travelling-wave acousto-optic modulators (AOMs). The signal is detected using a Hamamatsu<sup>TM</sup> avalanche photodiode (APD) in the far field regime and processed using a Stanford Research<sup>TM</sup> model 830 phase-sensitive lock-in amplifier. The frequencies of the modulations are  $\Omega_1 = 1.05\text{MHz}$  and  $\Omega_2 = 1\text{MHz}$  provided by two Novatech<sup>TM</sup> signal generators phased locked to each other. These frequencies are chosen so that they are large enough to suppress  $\frac{1}{f}$  noise, yet still smaller than the repetition rate of the pulsed Ti:Sapphire laser (76 MHz) to effectively modulate the pulse trains. The outputs from the signal generators are mixed with the RF driving frequencies of the AOMs (70 MHz) to create two modulated driving fields at 1.05MHz and 1MHz, which are connected to

the respective AOMs. The optical beams passing through the driven AOMs are Bragg diffracted at the modulation frequencies. The optical frequency of the +1(-1) order of the diffracted beam is increased (decreased) by the amount of the driving frequency (70 MHz). The opposite orders are usually chosen for the pump and probe beams to avoid optical interference on the detector in the case of degenerate frequencies between the pump and the probe. The signal is detected at the difference frequency of  $\Omega_1 - \Omega_2 = 50\text{KHz}$ , which is chosen to be within the detection frequency range of the lock-in amplifier. The phase-sensitive lock-in amplifier is specially designed to measure both the in-phase and out-of-phase component of the signal, in other words, it can measure  $\phi_{mod}$  from Equation 3.22.

The transmission collected on the APD from the QD sample often contains both signal and excitation fields. The detection of the signal field propagating along with the excitation fields is a special form of heterodyne detection. In a heterodyne detection setup, an external reference beam is introduced along the signal field to enhance signal detection. In homodyne detection, the reference beams are the original excitation beams. The signal and the excitation fields experience the same optical phase shift (independent of the electronic modulation phase of  $\phi_{mod}$ ) inside the medium and are propagating in phase. Since the phase shifts are the same, this method does not measure changes in the real component of the refraction index, but rather the imaginary component that leads to absorption. Therefore, in a homodyne setup, the differential modulation signal between pump on and pump off is a measurement of the effect of the pump field on the absorption of the probe field, or rather, the differential transmission (DT) of the fields. The homodyne signal on the APD is given by

$$I_{APD} = |E_{sig} + E_{ex}|^2 = |E_{sig}|^2 + |E_{ex}|^2 + 2\text{Re}\{E_{sig}E_{ex}\}, \quad (3.23)$$

where  $E_{sig}$  is the signal field, and  $E_{ex} = E_1 + E_2$  is the sum of the pump ( $E_1$ ) and probe ( $E_2$ ) fields. The first term in Equation 3.23 is the intensity related to the pure signal. Because  $E_{sig}$  is in general much weaker in comparison to  $E_{ex}$ , this term can be neglected. For a detectable DT signal at the difference frequency,  $I_{APD}$  must contain terms that are proportional to the product of the pump and probe field intensities as

suggested in Equation 3.22. This means the non-signal term,  $|E_{ex}|^2$ , is not detected and can also be omitted. The dominant DT signal ( $I_{DT}$ ) selected by the lock-in amplifier is the homodyne term

$$I_{DT} \cong 2\text{Re}\{E_{sig}E_{ex}\}. \quad (3.24)$$

The frequency filtering of the lock-in amplifier eliminates the first order linear absorption signal, making this phase-sensitive optical modulation detection technique an excellent tool for studying the third order nonlinear effects of a quantum system. Higher odd order terms from  $E_{sig}$  also have frequency components at the modulated frequency, and thus, are detected as well. These higher order signals are responsible for the observations of Rabi oscillations in Chapter 4 and 5.

This section gave a detailed explanation of a two-beam optically modulated detection technique. However, modulation techniques are in general used to eliminate undesired background signals. Once the fundamentals are understood, we can expand the technique to multiple-beam modulation, or voltage modulation such as that used in Chapter 7.

### 3.4 Chapter summary

This chapter provided a theoretical treatment of the origin of the signal field using a quantum mechanical approach to derive the macroscopic polarization field. Through the Maxwell-Bloch equation we established the relationship between the quantum derived polarization and the classical signal field. Finally, a background free detection method of the signal field was introduced using modulated optical pump and probe beams. The experimental method described in this chapter will be used as the main detection technique for the major experiments in this thesis.

## CHAPTER 4

### Phase-Sensitive Consecutive Qubit Rotations in a Single Semiconductor Dot

The two key elements of a family of universal gates in quantum information processing are the arbitrary single qubit rotational gate and the two-qubit control-NOT gate [2]. The fundamental building blocks behind these constituent gates and all quantum algorithms constructed from them are single Rabi rotations between the qubit states. However, the successful execution of an actual quantum algorithm is more than a matter of performing individual Rabi rotations perfectly. It is imperative that consecutive rotations also communicate with each other throughout the entire algorithm. This communication relies heavily on maintaining the coherence between the Rabi rotations and the quantum system, meaning that information imprinted by the first rotation is maintained and propagated via the quantum system to the subsequent rotation and so forth.

In semiconductor heterostructures, a set of universal gates has been demonstrated successfully in a single QD using qubits based on exciton pseudo-Bloch vectors [76, 104]. The Rabi rotations are performed using ultrafast optical pulses with well-defined pulse areas. The significance of this accomplishment is the suppression of higher dimensional scattering effects in a zero-dimensional QD system, which in turn allows the system to respond coherently during the optical excitations. Questions still remain, such as whether the QD system can communicate this coherent information from one optical Rabi rotation to another.

In this chapter, we investigate the ability of the QD system to perpetuate coher-

ent information between consecutive optical rotations by using a two pulse phase-locking technique. The phase-locked two-pulse configuration is analogous to the pair of Hadamard gates required to prepare and collapse the qubit in many quantum logic operations, including error correction codes [9], the Deutsch-Josa (DJ) algorithm [5] and Grover's search algorithm [7]. The execution of this pair of gates greatly influences the accuracy of the final outcome of the quantum operations. In addition, it plays a critical role in single qubit density matrix tomography discussed [124] (also see detail discussion in Chapter 5). Furthermore, the pair of phase-locked pulses are valuable in the measurement of the coherent lifetime of a quantum system [125].

This chapter begins with a theoretical discussion on the transient optical excitation of a simple two-level system. It is followed by the experimental setup with details on the phase-locking of two optical pulses. This technique is then applied to a single semiconductor QD to explore the dynamics of the exciton system under excitations of the phase-locked pulse pair with different relative phases. The experimental result is compared to the theoretical simulation taking into account system dephasing and finite pulse width, where errors and discrepancies are analyzed and discussed.

#### 4.1 Theory of transient excitation in a closed two-level system

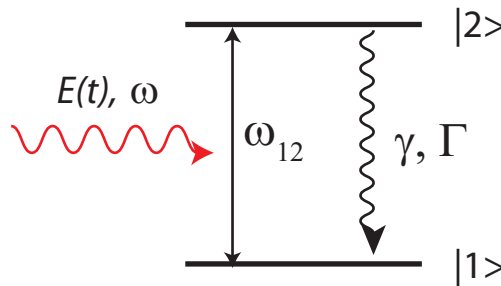


**Figure 4.1:** Diagram of a simple closed two-level system.  $\omega_{12}$  is the transition frequency between states  $|2\rangle$  and  $|1\rangle$ .  $E(t)$  is the excitation field with frequency  $\omega$ , and  $\gamma$  ( $\Gamma$ ) is the decoherence (population decay) rate between the states.

Optical transitions in a single QD between the crystal ground states and an exciton state can be closely modelled by physics of a simple two-level system seen in Figure 4.1. This approximation is valid as long as the three-dimensional quantum confinement

of the dots produces discrete energy states that are well-isolated from the higher dimensional scattering states. The excitation of the ground-exciton transition in a single QD by a strong transient optical field can be explained mathematically through the use of Pauli matrices and pictorially in the Bloch sphere representation.

#### 4.1.1 Two-level systems and the Pauli matrices

The general state of a two-level system can be expressed in the Dirac notation as  $|\psi\rangle = a_1|1\rangle + a_2|2\rangle$ , where  $a_1$  and  $a_2$  are probability amplitudes for states  $|1\rangle$  and  $|2\rangle$  in the normal representation, respectively. In the field interaction representation (see conversions and definitions in Chapter 3) with the rotating wave approximation (RWA) and the absence of decays, the Schrödinger equation of motion,  $i\hbar \dot{\vec{c}}(t) = \mathbf{H} \vec{c}(t)$ , for the probability amplitude state vector ( $\vec{c}$ ) of a two-level system [126–128] is simply

$$\begin{bmatrix} \dot{c}_1(t) \\ \dot{c}_2(t) \end{bmatrix} = -i \begin{bmatrix} -\frac{\delta}{2} & \chi^*(t) \\ \chi(t) & \frac{\delta}{2} \end{bmatrix} \begin{bmatrix} c_1(t) \\ c_2(t) \end{bmatrix}, \quad (4.1)$$

where  $\delta = \omega_{12} - \omega$  is the detuning of the excitation field ( $\omega$ ) from the transition resonance frequency ( $\omega_{12}$ ), and  $\chi(t) = -\frac{\boldsymbol{\mu}_{12} \cdot \mathbf{E}(t)}{2\hbar}$  is related to the time dependent envelop of the field amplitude,  $\mathbf{E}(t)$ , and the dipole moment,  $\boldsymbol{\mu}_{12}$ , of the transition between the two levels. Decays of the system are neglected here for simplicity. A full treatment including population decay and dephasing is evaluated numerically in Section 4.3.

The solution of Equation 4.1 does not have a general analytical form for arbitrary  $\mathbf{E}(t)$ . However solutions are available for select conditions on the detuning,  $\delta$ , and the pulse shape,  $\mathbf{E}(t)$ . For  $\delta \neq 0$ , analytical solutions are possible for hyperbolic secant pulses and square pulses. Since our interest focuses on the dynamics of the state of the quantum system after the pulse excitation and not during, we choose the more simple solution of the square pulse. The resultant final state after the excitation would be the same as long as the square pulse has the same pulse area as the actual hyperbolic secant pulse used in the experiment. For a more rigorous approach to the exact solution using the actual pulse shape, Rosen and Zener provide a detail

derivation in Ref. [129].

The square pulse solution to Equation 4.1 is

$$\vec{c}(t_p) = \mathbf{T}(t_p) \vec{c}(0) = e^{-i\frac{\Theta(t_p)}{2}} \vec{c}(0), \quad (4.2)$$

where

$$\Theta(t_p) = \frac{\mathbf{H}t_p}{\hbar} = \begin{bmatrix} -\delta t_p & \theta^*(t_p) \\ \theta(t_p) & \delta t_p \end{bmatrix}. \quad (4.3)$$

The general value of  $\theta(t_p) = 2 \int_{-\infty}^{t_p} \chi(t') dt'$  is denoted as the time-dependent pulse area of the pulsed excitation field,  $\mathbf{E}(t)$ . For a square pulse,  $\theta(t_p) = 2\chi t_p$  where  $\chi$  is a constant and  $t_p$  is the pulse duration. The term  $\mathbf{T}(t_p) = e^{-i\frac{\Theta(t_p)}{2}}$  in Equation 4.2 is the unitary time evolution operator for the initial state vector  $\vec{c}(0)$  [127], which describes how the state vector evolves from its initial value in time. This operator can be rewritten in terms of the Pauli spin matrices to further examine the details of the time evolution.

The Pauli spin matrices are normally associated with the two-level spin- $\frac{1}{2}$  system. This set of  $2 \times 2$  orthogonal unitary matrices is the followed,

$$\sigma_x = \begin{bmatrix} 0 & 1 \\ 1 & 0 \end{bmatrix}, \quad \sigma_y = \begin{bmatrix} 0 & -i \\ i & 0 \end{bmatrix}, \quad \sigma_z = \begin{bmatrix} 1 & 0 \\ 0 & -1 \end{bmatrix}. \quad (4.4)$$

They each corresponds to a physical observable of the spin system, namely, the spin angular momentum projection onto each of the three spatial coordinates ( $\hat{\mathbf{x}}$ ,  $\hat{\mathbf{y}}$ , and  $\hat{\mathbf{z}}$ ) as labelled. Because the Pauli spin matrices are the generators for the SU(2) Lie group [130], in combination with the identity matrix,  $\mathbf{I}$ , they form a complete set that can express any  $2 \times 2$  complex matrix, including the Hamiltonian of a two-level quantum system.

Equation 4.3 rewritten in terms of the Pauli spin matrices is then

$$\Theta(t_p) = \text{Re}\{\theta(t_p)\} \sigma_x + \text{Im}\{\theta(t_p)\} \sigma_y + \delta t_p \sigma_z = \Theta(t_p) \hat{\mathbf{n}} \cdot \vec{\sigma}, \quad (4.5)$$

where  $\Theta(t_p) = \sqrt{(\delta t_p)^2 + |\theta(t_p)|^2}$  is the amplitude of the field-associated vector in the direction of  $\hat{\mathbf{n}} = [\text{Re}\{\theta(t_p)\} \hat{\mathbf{x}} + \text{Im}\{\theta(t_p)\} \hat{\mathbf{y}} + \delta t_p \hat{\mathbf{z}}] / \Theta(t_p)$ , and  $\vec{\sigma} = \sigma_x \hat{\mathbf{x}} + \sigma_y \hat{\mathbf{y}} + \sigma_z \hat{\mathbf{z}}$  is



the Pauli spin vector. By substituting the term from Equation 4.5 into Equation 4.2, the rewritten solution is

$$\vec{c}(t_p) = \mathbf{T}(t_p) \vec{c}(0) = e^{-i\frac{\Theta(t_p)}{2}\hat{\mathbf{n}}\cdot\vec{\sigma}} \vec{c}(0). \quad (4.6)$$

The unitary time evolution operator,  $\mathbf{T}(t_p)$ , is now in the form of the generator of infinitesimal rotation. Further simplification of  $\mathbf{T}(t_p)$  using the identity expression  $e^{-i\vec{a}\cdot\vec{\sigma}} = \cos a\mathbf{I} - i\sin a(\hat{\mathbf{n}}\cdot\vec{\sigma})$  brings the solution in Equation 4.6 to its final form,

$$\begin{bmatrix} c_1(t_p) \\ c_2(t_p) \end{bmatrix} = \begin{bmatrix} \cos \frac{\Theta(t_p)}{2} + i\frac{\delta t_p}{\Theta(t_p)} \sin \frac{\Theta(t_p)}{2} & -i\frac{\theta^*(t_p)}{\Theta(t_p)} \sin \frac{\Theta(t_p)}{2} \\ -i\frac{\theta(t_p)}{\Theta(t_p)} \sin \frac{\Theta(t_p)}{2} & \cos \frac{\Theta(t_p)}{2} - i\frac{\delta t_p}{\Theta(t_p)} \sin \frac{\Theta(t_p)}{2} \end{bmatrix} \begin{bmatrix} c_1(0) \\ c_2(0) \end{bmatrix}. \quad (4.7)$$

For the spin- $\frac{1}{2}$  system, the time evolution operator,  $\mathbf{T}(t_p)$ , is associated with physical rotation of the initial spin around the applied field in Cartesian coordinate space. In a general two-level system, the rotation occurs in the abstract Hilbert space. In both cases, the dynamics of the rotation becomes more apparent as we translate the results obtained here to the Bloch sphere representation covered in the next subsection (Subsection 4.1.2).

#### 4.1.2 Rotations in the Bloch sphere representation

The Bloch sphere representation is a useful tool in visualizing the evolution of a two-level quantum system during free induction decays and excitation by an external field. While mathematically, we need to solve the Schrödinger equations exactly to extract information on the time evolution of the state of the system, pictorially through the Bloch sphere such information is easily obtained even when analytical solutions are impractical.

The Bloch sphere representation is derived from the field interaction density matrix formalism of the two-level system. The density matrix master equations including general decay parameters are derived in Section 3.1 of Chapter 3. For this subsection, decays are neglected to emphasize the excitation aspect of the dynamics.

The axes of the Bloch sphere are generally denoted by  $\hat{\mathbf{u}}$ ,  $\hat{\mathbf{v}}$ , and  $\hat{\mathbf{w}}$  as seen in Figure 4.2. Two important definitions in the Bloch sphere representation are the

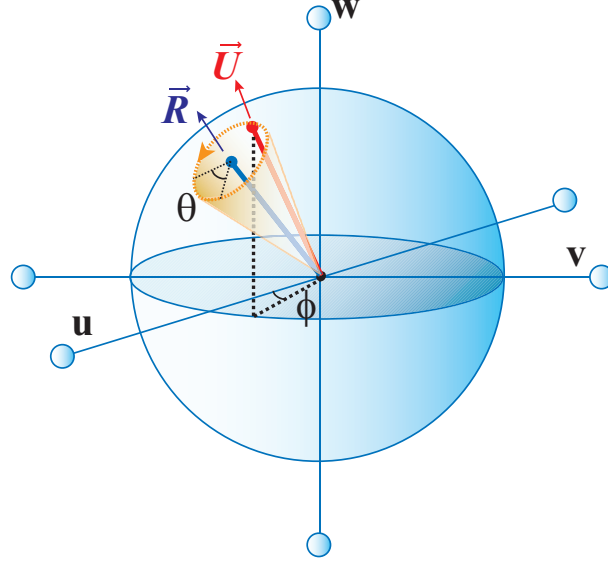


**Figure 4.2:** Bloch sphere representation of a general two-level system. The bases of the sphere are  $\hat{u}$ ,  $\hat{v}$  and  $\hat{w}$ . The thick red (blue) solid line represents the Bloch (pseudo-field) vector,  $\vec{U}$  ( $\vec{R}$ ). The dotted orange line represents the path and direction of  $\vec{U}$ 's precession around  $\vec{R}$ . The angle,  $\theta$ , traced out by the precession represents the pulse or transition area. The angle,  $\phi$ , represents the overall phase of the field.

Bloch vector ( $\vec{U}$ ) and the pseudo-field vector ( $\vec{R}$ ), where

$$\vec{U} = \begin{bmatrix} U_{\hat{u}} \\ U_{\hat{v}} \\ U_{\hat{w}} \end{bmatrix} = \begin{bmatrix} 2\text{Re}\{\rho_{12}\} \\ -2\text{Im}\{\rho_{12}\} \\ \rho_{22} - \rho_{11} \end{bmatrix}, \quad \vec{R} = \begin{bmatrix} R_{\hat{u}} \\ R_{\hat{v}} \\ R_{\hat{w}} \end{bmatrix} = \begin{bmatrix} 2\text{Re}\{\chi\} \\ -2\text{Im}\{\chi\} \\ \delta \end{bmatrix}. \quad (4.8)$$

The Bloch vector ( $\vec{U}$ ) contains density matrix elements describing the initial state of the system, including both state populations ( $\rho_{11}$  and  $\rho_{22}$ ) as well as the coherence between the states ( $\rho_{12}$ ). The pseudo-field vector ( $\vec{R}$ ), on the other hand, discloses information on the detuning ( $\delta$ ) of the field from the resonance frequency of the system, and the coupling strength and relative phase between the field and the system through the term  $\chi$ . The interaction dynamics between the excitation field and the system is characterized by the cross-product of the the two vectors,

$$\dot{\vec{U}} = \vec{R} \times \vec{U}, \quad (4.9)$$

which illustrates the precession of the Bloch vector,  $\vec{U}$ , about the pseudo-field vector,  $\vec{R}$ , as shown in Figure 4.2. The angle,  $\theta$ , swept out during the precession is the

area of the excitation pulse field and also the corresponding transition. The angle,  $\phi$ , represents the overall phase of the field.

The advantage of the Bloch sphere is evident in the fact that the final state of the system can be extracted from the pictorial representation without the need for solving Equation 4.9. For example, given the knowledge of the excitation field with a pulse area of  $\theta$  and the initial conditions of the system, we can construct two vectors ( $\vec{\mathbf{R}}$  and  $\vec{\mathbf{U}}$ ) in the Bloch sphere. The next step is simply precessing  $\vec{\mathbf{U}}$  about  $\vec{\mathbf{R}}$  by an angle of  $\theta$  and reading out the final state of the system by examining the projection of  $\vec{\mathbf{U}}$  onto each axes of the sphere.

The discussion in this section provides the basic physical model for a general two-level system. To customize the solution for the experiments presented in this thesis, we apply the experimental parameters to the matrix solution in Equation 4.7, namely,  $\delta = 0$  for on resonance excitation. The solution then has the following simplified form,

$$\begin{bmatrix} c_1(t_p) \\ c_2(t_p) \end{bmatrix} = \begin{bmatrix} \cos \frac{|\theta(t_p)|}{2} & -ie^{i\phi} \sin \frac{|\theta(t_p)|}{2} \\ -ie^{-i\phi} \sin \frac{|\theta(t_p)|}{2} & \cos \frac{|\theta(t_p)|}{2} \end{bmatrix} \begin{bmatrix} c_1(0) \\ c_2(0) \end{bmatrix}, \quad (4.10)$$

where  $\phi$  is the overall phase of the excitation field. This substitution corresponds to the pinning of the pseudo-field vector,  $\vec{\mathbf{R}}$ , on the  $\mathbf{u} - \mathbf{v}$  plane of the Bloch sphere. For rotations by more than one pulse, the multi-pulse time evolution operator of the initial state is simply the product of the representing time evolution operators for each pulse,  $\mathbf{T} = \prod \mathbf{T}_n(\theta_n, \phi_n)$ . The expression for consecutive rotations by two distinct pulses is written out for the convenience of later discussion,

$$\begin{aligned} \mathbf{T} &= \mathbf{T}_2(\theta_2, \phi_2)\mathbf{T}_1(\theta_1, \phi_1) \\ &= \begin{bmatrix} \cos \alpha \cos \beta - e^{i\Delta\phi} \sin \alpha \sin \beta & -i(e^{i\Delta\phi} \sin \beta \cos \alpha + \sin \alpha \cos \beta) \\ -i(e^{-i\Delta\phi} \sin \beta \cos \alpha + \sin \alpha \cos \beta) & \cos \alpha \cos \beta - e^{-i\Delta\phi} \sin \alpha \sin \beta \end{bmatrix}, \end{aligned}$$

where  $\Delta\phi = \phi_2 - \phi_1$ ,  $\alpha = \frac{|\theta_1|}{2}$ , and  $\beta = \frac{|\theta_2|}{2}$ .

For the remainder of the thesis, Equation 4.10, Equation 4.11, and their corresponding Bloch sphere representation will be referred to for future physical discussions on two-level transitions in exciton (Chapter 4, Chapter 5), trion and spin (Chapter 6) systems.

## 4.2 Experimental setup and phase-locking two optical pulses

The semiconductor sample studied in this experiment is NRL-1197King. It consists of interface fluctuation GaAs/Al<sub>0.3</sub>Ga<sub>0.7</sub>As QDs [75,88,90] as presented in Chapter 2. The sample is mounted inside a continuous flow liquid helium cryostat (Janis Research<sup>TM</sup>10DT) and stabilized at 7 K to inhibit acoustic phonon modes. Optical excitations and detections are performed through the 0.5  $\mu\text{m}$  aperture located at  $(r,c) = (2,6)$ , where “r” and “c” represent the row and column positions, respectively. The sub-micron aperture provides the necessary spatial filtering needed to excite and detect individual quantum dots.

The experimental setup is shown in Figure 4.3. The optical pump and probe pulses are derived from a single 702 series dye laser synchronously pumped by a 76 MHz mode-locked, doubled Nd-YAG Antares laser, both from Coherent<sup>TM</sup>. The pump and probe beams are each modulated by a travelling wave acousto-optic modulator (AOM) at  $\Omega_1=1.05$  MHz and  $\Omega_2=1$  MHz, respectively. A three-plate birefringent filter inside the 702 laser cavity produces a pulse width of 5 ps, corresponding to a spectral bandwidth of 0.37 meV.

To achieve two pump pulses with tunable coarse (on orders of ps) and fine (on order of fs) delays for consecutive qubit rotation, the pump beam is split by a 50/50 beam splitter and sent through a Michelson interferometer. One arm of the interferometer is controlled by a micro-translation stage for the picosecond coarse delay ( $\tau$ ) between the pulses. The other arm is modified by a piezoelectric translation stage (PZT) which provides high resolution temporal control on the order of sub-femtosecond. This delay path is used to control the optical phase ( $\phi$ ) between the two pump pulses. For on resonance transitions in this particular sample, the excitation wavelength is around 760 nm. Even a slight movement of the order of micrometers can disrupt the stability of the optical phase between pulses. To counteract this problem, an active feedback loop stabilizes the PZT to eliminate disturbances from air currents and other causes of micro-motions. The stabilization circuit is presented in Appendix A.

The nonlinear differential transmission (DT) signal is obtained by scanning the delay of the probe pulse through the time scale of interest covering the double-pump

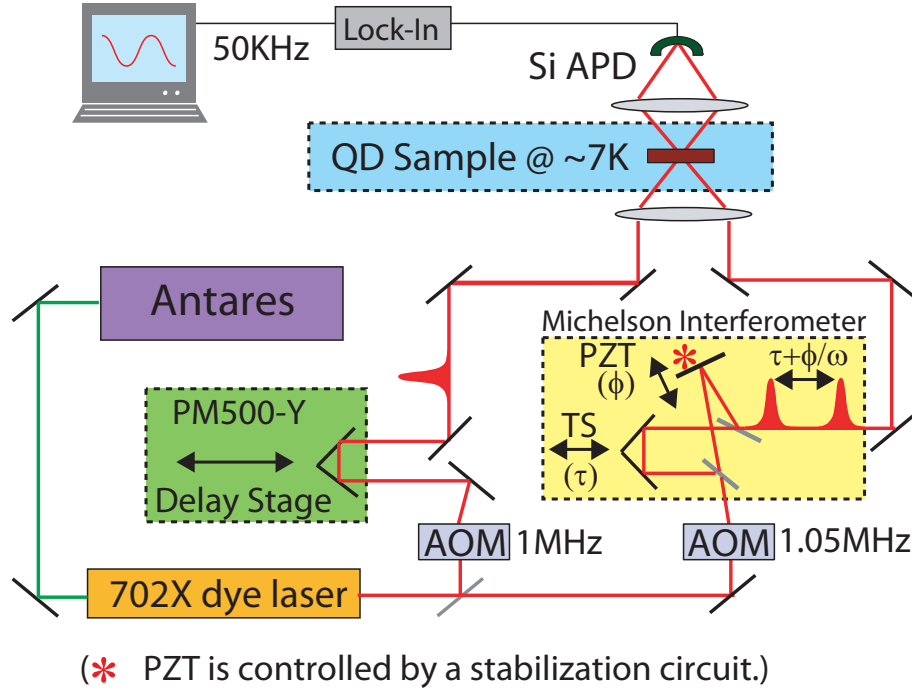


**Figure 4.3:** Experimental setup of the phase-locking experiment. The micro-translation stage (TS) controls the coarse delay ( $\tau$ ) while the piezoelectric translation stage (PZT) controls the optical phase delay ( $\phi$ ) between the two pump pulses.  $\omega$  is the center frequency of the laser pulse.

pulsed excitation and the subsequent decay. The signal is detected optically by a silicon avalanche photodiode (APD) and processed through a lock-in amplifier and computer at the reference frequency of  $\Omega_1 - \Omega_2 = 50$  KHz.

### 4.3 Consecutive rotations of an exciton-based qubit

The physical structure of the interface fluctuation dots allows for the confinement of two linear-orthogonally polarized ( $\Pi_x$  and  $\Pi_y$ ) excitons inside a single dot [88]. For two uncoupled excitons, the energy level diagram is two separate two-level systems each representing one exciton transition as shown in Figure 4.4(a). In these dots, however, the excitons are Coulomb coupled, which leads to an intertwined energy level diagram of a four-level system as shown in Figs. 4.4(b). The lower state is the crystal ground state, the intermediate states are the two nearly degenerate linear-orthogonally polarized excitons, and the upper state is the biexciton. Since the laser

pulse bandwidth (0.37 meV) is much smaller than the binding energy of the biexciton  $\Delta_{XX} \sim 3.5$  meV) [104], we can safely neglect transitions to the biexciton and concentrate on the reduced three level  $\mathbf{V}$  system in the dashed boxes illustrated in Figs. 4.4(b).

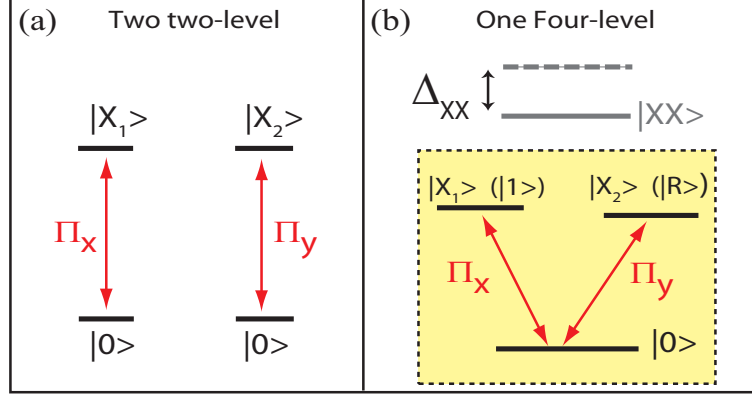


**Figure 4.4:** Energy level diagram of excitons. (a) Two uncoupled excitons ( $|X_1\rangle$  and  $|X_2\rangle$ ). (b) Two coupled excitons make up a four-level system.  $|0\rangle$  is the crystal ground state and one of the qubit state,  $|X_1\rangle$  ( $|X_2\rangle$ ) also serves as qubit state  $|1\rangle$  (read out state  $|R\rangle$ ), and  $|XX\rangle$  is the biexciton state. The binding energy for the biexciton is  $\Delta_{XX} \sim 3.5$  meV.  $\Pi_x$  ( $\Pi_y$ ) is the polarization of the transition along the  $\hat{x}$  ( $\hat{y}$ ) direction.

For the control-ROT experiment in Reference [104], both exciton transitions constitute qubits. Here, we define one polarized transition of the exciton ( $\Pi_x$ , horizontal) as the qubit and the orthogonally polarized transition ( $\Pi_y$ , vertical) as the readout for the purpose of this measurement. The qubit states are  $|0\rangle$  and  $|1\rangle$  and the state  $|R\rangle$  is the readout exciton as labelled in Figs. 4.4(b).

Through the spatial filtering of the sub-micron apertures, the number of excitable dots is decreased from order of millions to order of tens (Chapter 2). Further selectivity relies on the spectral resolution of the optical excitation field. A narrow band continuous wave (cw) laser (bandwidth  $\sim 300$  KHz) is first used to resolve and characterize single exciton states under each small aperture. Both pump and probe beams are linearly co-polarized and degenerate in frequency. Their powers are kept at a linear response regime in third order of the field to avoid saturating the states. The frequency of the laser beams are then scanned to obtain the DT spectra. The average

linewidth of an exciton state is around 30 GHz. Once the true single exciton states are verified, the 5 ps pulsed laser is setup in the same configuration to reproduce the energy spectra and determine the state best suited for the experiment. An example of a good candidate is highlighted in the spectra in Figure 4.5, which has the signature of a clear single exciton state in the cw spectrum and also appeared well-isolated in the pulsed spectrum.

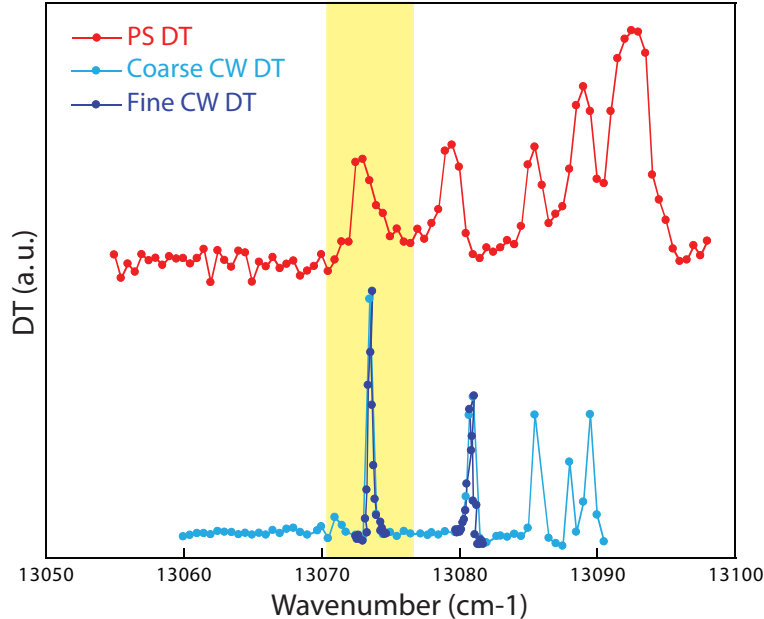


**Figure 4.5:** Degenerate DT measurements by ps pulsed (red) and cw (blue) lasers through aperture (2,6) on NRL-1197King. The lighter blue data points are a cw rough scan and the dark blue data points are the fine scan over the single states. The highlighted exciton state is the state used in the consecutive rotation experiment.

In contrast to the frequency domain measurements, which use optical fields in the weak field regime, the time domain measurements use a strong pump field with pulse area  $\theta > \pi/2$  to actually rotate the qubit. In addition, for the time domain measurements in the rest of the discussion, the pump and probe beams are cross-polarized. The pump beam is tuned on resonance to the transition of the qubit states,  $|0\rangle$  and  $|1\rangle$ , and the probe is tuned on resonance to the transition to the readout state,  $|R\rangle$ , as indicated in Figure 4.4. The crossed-polarization of the beams ensure that the state preparation and manipulation are solely due to the pump pulse

or pulses, and the probe pulse is only responsible for measuring the outcome. The DT signal is detected along the probe through a polarizer that eliminates the pump beam after the sample. The response of the system is attributed to all orders of the pump and first order of the probe. The DT pump on minus pump off signal, to first order of the probe, is proportional to  $\rho_{0R}^{(1)}$ ,

$$DT \propto (\rho_{0R}^{(1)})_{on} - (\rho_{0R}^{(1)})_{off} \propto (\rho_{RR}^{(0)} - \rho_{00}^{(0)})_{on} - (\rho_{RR}^{(0)} - \rho_{00}^{(0)})_{off}, \quad (4.11)$$

where  $\rho_{RR}^{(0)}$  and  $\rho_{00}^{(0)}$  are the density matrix elements after solving for all orders of the pump. Since the pump pulse is not coupled to state  $|R\rangle$ , and all the state population is initially in state  $|1\rangle$  without any excitation,  $(\rho_{RR}^{(0)})_{on} = (\rho_{RR}^{(0)})_{off} = 0$  and  $(\rho_{00}^{(0)})_{off} = 1$ . Furthermore, for a closed system,  $\rho_{00}^{(0)} + \rho_{11}^{(0)} + \rho_{RR}^{(0)} = 1$ . With these substitutions, the expression in Equation 4.11 is simplified to

$$DT \propto (\rho_{0R}^{(1)})_{on} - (\rho_{0R}^{(1)})_{off} \propto (\rho_{11}^{(0)})_{on}. \quad (4.12)$$

This signifies that the DT signal is proportional to the populations in the qubit state  $|1\rangle$ .

The excitons in each single dot have an average lifetime of 60 ps with negligible pure dephasing effects inferred from nonlinear spectroscopy studies [125, 131]. The lifetime of the the selected state in Figure 4.5 is measured in Figure 4.6 to be 60 ps using a single  $\frac{\pi}{2}$  pump pulse. The pulse area is determined by optical Rabi oscillation measurements [76, 132–134] which correlates pulse areas to average laser powers. The details of obtaining Rabi oscillations are described in Reference [76] and will not be discussed here. Since the 5 ps pulse is short compared to the 60 ps population decay time, it is an appropriate compromise between operational speed and spectral selectivity.

Single qubit rotations are performed by applying single pump pulses with corresponding pulse areas from 0 to  $\pi$ , which create arbitrary superposition states of  $|0\rangle$  and  $|1\rangle$  from the initial state  $|0\rangle$ . Phase sensitive consecutive qubit rotations are performed by two phased-locked pump pulses. We chose each pump pulse area to be  $\theta = \pi/2$  because this creates a quantum state with maximum coherence. Such a



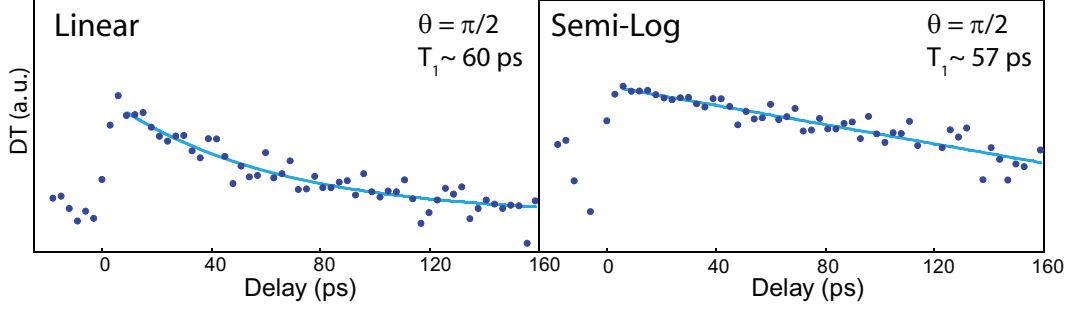


**Figure 4.6:** Time domain DT measurement of exciton  $T_1$  on linear and semi-log scales. The pulse area used is  $\frac{\pi}{2}$  and the pump and probe are linearly cross-polarized. The blue lines are fits to the decay parts of the scans, which measures a population decay time of  $T_1 \sim 60$  ps.

state is most affected by the changes in the relative phase,  $\Delta\phi$ , between the pulses. The pump pulses are separated by  $\tau = 23$  ps to ensure that the final qubit state is due to two distinct optical pulses, and not the product of optical interference. This  $\tau$  is chosen to sufficiently reduce optical interference while minimizing system decay during the separation. Using Equation 4.11, we can predict the outcome of the state after two consecutive  $\frac{\pi}{2}$  pulses with varying the relative phase,  $\Delta\phi$ , through the PZT stage, for an exciton system initially at the crystal ground state  $|0\rangle$ ,

$$\begin{bmatrix} c_0 \\ c_1 \end{bmatrix} = \begin{bmatrix} \frac{1}{2}(1 - e^{i\Delta\phi}) & -\frac{i}{2}(1 + e^{i\Delta\phi}) \\ -\frac{i}{2}(1 + e^{-i\Delta\phi}) & \frac{1}{2}(1 - e^{-i\Delta\phi}) \end{bmatrix} \begin{bmatrix} 1 \\ 0 \end{bmatrix}. \quad (4.13)$$

The corresponding density matrix elements of the final state are

$$\begin{aligned} \rho_{00}(\Delta\phi) &= \sin^2 \frac{\Delta\phi}{2}, \\ \rho_{11}(\Delta\phi) &= \cos^2 \frac{\Delta\phi}{2}, \\ \rho_{01}(\Delta\phi) &= \frac{1}{2} \sin \Delta\phi, \end{aligned}$$

Equation 4.14 shows that by varying  $\Delta\phi$ , we are changing the effective pulse area of the pulse sequence. These changes in  $\Delta\phi$  are reflected in the sinusoidal oscillations of the  $|1\rangle$  state population as illustrated by the quantum interferograms in the insets of Figures 4.8(c) and (d). The maxima of the interferogram correspond to constructive interference ( $\Delta\phi = 2\pi$ , effective  $\theta = \pi$ ) while the minima correspond to destructive interference ( $\Delta\phi = \pi$ , effective  $\theta = 0$ ).

To break down the dynamics of the two-pulsed phase-locked qubit rotation, we examine two extreme cases in the time domain measurement,  $\Delta\phi = \pi$  and  $\Delta\phi = 2\pi$ ,

with the aid of the Bloch sphere representation. The component of the Bloch vector projected onto the  $\mathbf{u-v}$  plane represents the coherence, and the projection onto the  $\hat{\mathbf{w}}$  axis represents the population difference of the quantum system. The  $|0\rangle$  ( $|1\rangle$ ) state is represented by the Bloch vector pointing down (up). Since all the excitations are on resonance, the representing pseudo-field vectors are strictly on the  $\mathbf{u-v}$  plane.

The phase  $\phi_1$  of the first optical pulse is irrelevant and can be set to zero, which means the first pseudo-field vector is real and aligned along the  $\hat{\mathbf{u}}$  axis (see Subsection 4.1.2). Ideally, for two pump pulses each at  $\theta = \frac{\pi}{2}$ , the qubit state is initially driven from the  $|0\rangle$  state to the  $(|0\rangle - i|1\rangle)/\sqrt{2}$  state. This is described by the Bloch vector rotating around the field vector from a down position to the  $\mathbf{u-v}$  plane along the  $\hat{\mathbf{v}}$  axis following Equation 4.9. By setting  $\Delta\phi = \pi$ , the pseudo-field vector of the out-of-phase second pulse lies along the  $-\hat{\mathbf{u}}$  axis. Precession around this field rotates the Bloch vector an angle of  $\frac{\pi}{2}$  back to down position, which translates to driving the quantum state back down to  $|0\rangle$  as shown in Figure 4.7. This two-pulse combination acts with an effective pulse area of  $\theta = 0$ , and the corresponding DT signal after the full rotations of the two pulses are anticipated to be zero.

In contrast, for  $\Delta\phi = 2\pi$ , the pseudo-field vector of the in-phase second pulse is in the same direction as the first pulse, and continue to rotate the Bloch vector to the up position. This corresponds to driving the quantum state up to  $|1\rangle$  as shown in Figure 4.7. This combination acts with an effective pulse area of  $\theta = \pi$ , and the DT signal after the rotations should be equivalent to that of a single  $\pi$  pulse. Hence, phase control between consecutive quantum operations is critical since two consecutive rotations with the same magnitudes but different phases can lead to profoundly different outcomes, a result well known in atomic type systems. The ability to control this phase then ensures control for consecutive and arbitrary qubit rotations as well as accuracy of the operation output, all of which are necessary for practical quantum information processing.

The experimental data are taken by fixing the pump pulses temporally and scanning the probe delay to observe the dynamics of the system. Because of decay in the physical system, experimental results deviate from the ideal case. Despite the

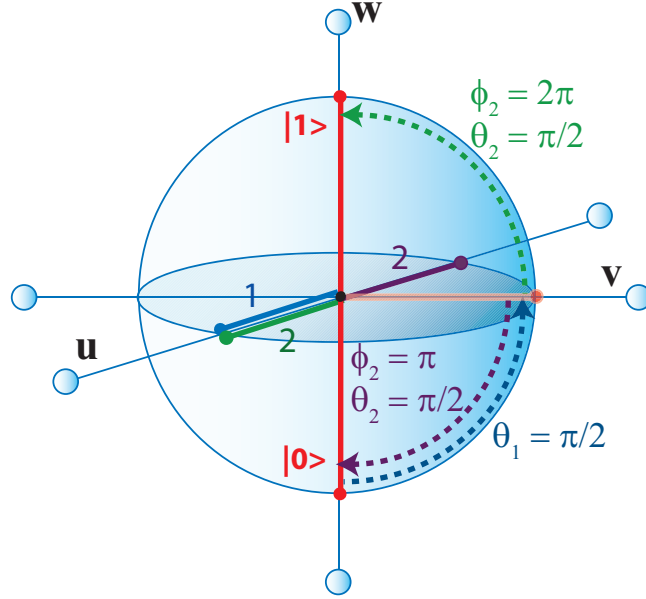


**Figure 4.7:** Ideal Bloch representation of the two consecutive  $\frac{\pi}{2}$  rotations at  $\Delta\phi = \pi$  and  $2\pi$ . The blue, green and purple solid lines are the pseudo-field vectors. The red lines are the Bloch vectors. The dashed curves represent the the precession paths around the pseudo-field vectors with respective colors. The blue color scheme is depict the first pump pulse, the purple depict the second pump pulse with  $\Delta\phi = \pi$ , and green depict the second pump pulse with  $\Delta\phi = 2\pi$ .

decay, we see clearly that in the case of  $\Delta\phi = \pi$  (Figure 4.8(c)), the population is being driven back down to state  $|0\rangle$  by the second pulse. Due to the population decay from the  $|1\rangle$  state, part of the population lost the phase information between the two pulses and is not affected by the second pulse in a coherent manner. Hence, the signal does not diminish after the second pulse, and the non-zero signal is largely due to the incoherent population. Similarly, in the case of  $\Delta\phi = 2\pi$  (Figure 4.8(d)), the population is being driven up to state  $|1\rangle$ , but the decay process prevents the signal from reaching the same strength as that created a single  $\pi$  pulse. The fast population decay leads to the loss of coherence between the two qubit states and limits the accuracy of coherent control by laser pulses.

Pure population decay in the Bloch sphere is represented by the Bloch vector rotating from its original position back down toward the  $-\mathbf{w}$  direction. In this case, the Bloch vector strays from its position on the  $\mathbf{u}-\mathbf{v}$  plane after the first  $\frac{\pi}{2}$  rotation and decay towards  $-\mathbf{w}$ , reducing the angle between the two directions. Recalling the

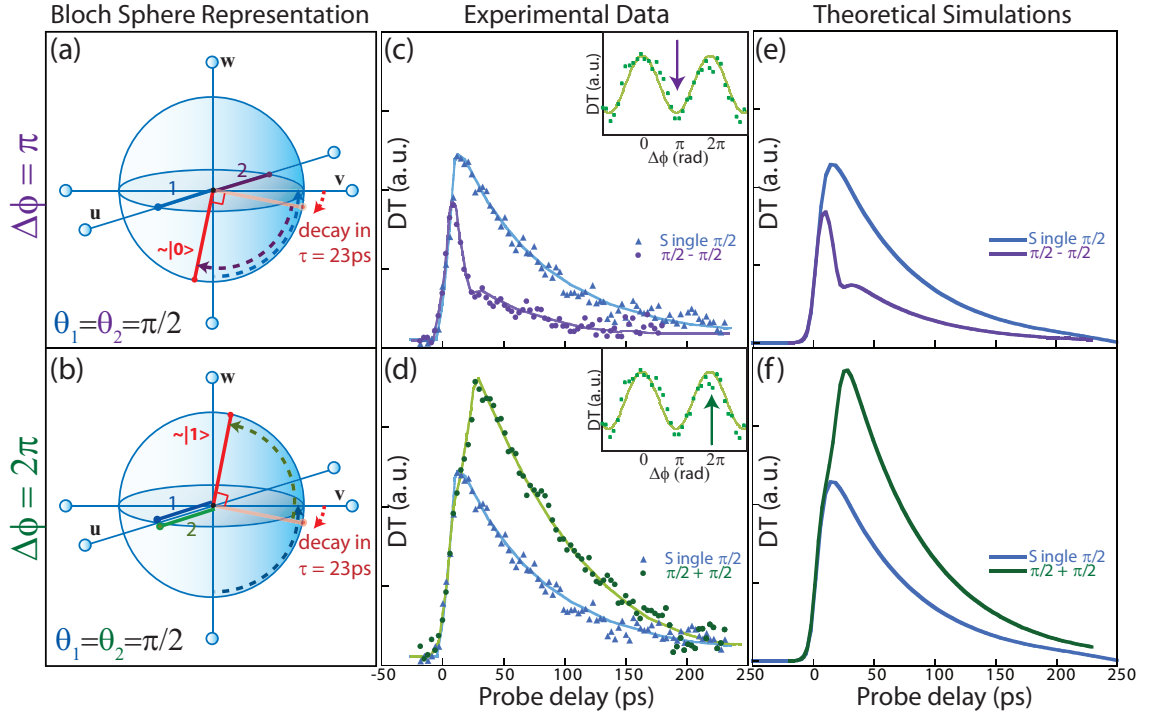


**Figure 4.8:** Experimental results of two consecutive  $\frac{\pi}{2}$  rotations of a qubit at  $\Delta\phi = \pi$  and  $2\pi$ . (a) and (b) are Bloch representation of the rotations in a physical qubit system. The red arrows represent population decay. (c) and (d) are the experimental data where the purple (green) plot corresponds to a relative phase of  $\Delta\phi = \pi(2\pi)$  between the two pump pulses. The blue plots are the same single  $\pi/2$  decay, which serves as a comparison. The lines are guides to the eye. The insets are interferograms. (e) and (f) are theoretical simulations of the experimental data taking into account all the experimental parameters.

meaning of each axis for the Bloch vector in Equation 4.8, this means it is losing coherence component and gaining population in the  $|0\rangle$  state. As the second  $\frac{\pi}{2}$  pulse arrives, the rotation overshoots the  $-\mathbf{w}$  direction and gains a  $|1\rangle$  component (Figure 4.8(a)), which is the source of the non-zero signal in the case of  $\Delta\phi = \pi$ . In the case of  $\Delta\phi = 2\pi$ , the rotation of  $\frac{\pi}{2}$  is insufficient for the Bloch vector to be completely aligned in the  $\mathbf{w}$  direction (Figure 4.8(b)), and causes the deviation from the DT signal.

Another contribution to the discrepancy is due to the temporal overlap of the two pulses. Although the pulses are separated by 23 ps, the tail of the first pulse and front of the second pulse are still overlapped in time. In the Bloch sphere representation,

this signifies the simultaneous rotation of the Bloch vector by the two pulses during the overlap. We simulate the data in Figures 4.8(e) and (f) by numerically solving the Schrödinger equations for the exciton system using all the experimental parameters. The results reproduce the data excellently.

We can avoid errors caused by simultaneous rotation of the Bloch vector by separating the two pulses further to eliminate overlaps, but the short decoherence between the qubit states  $|0\rangle$  and  $|1\rangle$  will begin to introduce greater error as the measurement is made at a larger delay. It may be that the discrepancies can be minimized by using a combination of pulse-shaping techniques on shorter pulses to avoid exciting nearby states [53, 135, 136]. Quantum systems with longer decay times, such as the spin qubit system in charged QDs (see Chapter 6), would also minimize this error.

#### 4.4 Chapter summary

In this chapter, we have demonstrated consecutive phase dependent qubit rotations. This accomplishment proves that the exciton quantum system has the ability to maintain coherent information during its lifetime. This technique is extremely useful in density matrix tomography of the single qubit (Chapter 5), where the phased-locked pulses are acting as coherent rotations of the measurement axes. Improved performance in optically driven spin based systems [111] is anticipated because spin lifetimes are expected to be four orders of magnitude longer than the exciton system [106, 107, 109, 137].

## CHAPTER 5

### Density Matrix Tomography of a Single Exciton-Based Qubit

Many critical milestones toward practical quantum computation have now been achieved in exciton based quantum bit (qubit) systems including single qubit rotation [76], a two-qubit controlled-NOT gate [104] and a two-qubit population swap [138]. The next practical step would be to quantify the performance (fidelity) of these operations mentioned above [9] using density matrix tomography. In other words, we need to be able to measure the values of the population and coherence terms of all the qubits involved after the quantum operations. The comparison of the physical density matrix to the ideal density matrix of the result qubit states can then be used to decide the appropriate error corrective actions needed in the quantum operations.

In this chapter, we demonstrate density matrix tomography of a single exciton-based qubit in a single semiconductor quantum dot (QD) [124]. The density matrix tomography technique combines procedures of signal calibration and optical phase control on an exciton-based qubit in a single QD. The key ingredient of this technique is the controlled rotation of the measurement basis of the qubit. This approach is commonly used in nuclear magnetic resonance (NMR) [139] and atomic [140] systems, and it enables us to measure both the real and imaginary components of the coherence term as well as the population terms.

In the exciton-based qubit system, the basis rotation is achieved by phase-locking the optical rotation pulse to the quantum state being measured (details in Chapter 4). The new measurement basis is determined by the relative phase between the preparation pulse and the rotation pulse.

The chapter begins with a theoretical interpretation of the physics behind rotating a measurement basis. Then the experiment divided into two parts: 1) Calibration and renormalization of the differential transmission (DT) signal, and 2) The reconstruction of the density matrix of a single exciton-based qubit after a  $\frac{\pi}{2}$  pulse excitation. The experimental result is then analyzed and compare to the ideal case and the fidelity of the measurement process is extracted.

### 5.1 Theory on the rotations of the measurement basis

Classically, a single bit can only retain one discrete value at a given time, 0 or 1, obtaining information on the bit is simply a matter of measuring which state it currently occupies. Quantum mechanically, however, since a qubit can be in a superposition of the qubit states,  $\alpha|0\rangle + \beta|1\rangle$ , obtaining information on the true state of the system becomes nontrivial, especially when the measurement process also destroys the prepared state.

The measurable physical quantities for a qubit state of  $\alpha|0\rangle + \beta|1\rangle$  are not the state amplitudes,  $\alpha$  and  $\beta$ , but rather the population of each state,  $\rho_{00} = \alpha^*\alpha$  and  $\rho_{11} = \beta^*\beta$ , and the coherence between the two states,  $\rho_{01} = \alpha^*\beta$ , with  $\rho_{01}$  in general being a complex number with both real and imaginary terms. By only measuring the population terms,  $\rho_{00}$  and  $\rho_{11}$ , we cannot distinguish between a pure state ( $\alpha|0\rangle + \beta|1\rangle$ ) and a mixed state ( $\alpha|0\rangle$  and  $\beta|1\rangle$ ). Therefore, a fully characterized qubit state requires all four pieces of information, two population terms, and the real and imaginary components of the coherence term. These quantities can be summarized into a single  $2 \times 2$  density matrix,

$$\boldsymbol{\rho}_0 = \begin{bmatrix} \rho_{00} & \rho_{01} \\ \rho_{10} & \rho_{11} \end{bmatrix} = \begin{bmatrix} \alpha^*\alpha & \alpha\beta^* \\ \beta\alpha^* & \beta^*\beta \end{bmatrix}. \quad (5.1)$$

In general, the population terms,  $\rho_{00}$  and  $\rho_{11}$ , can be extracted directly from the optical signal, provided that there is a way to calibrate and renormalize the DT signal. Obtaining the coherence term, on the other hand, is not as straightforward. Most optical measurement processes detect optical intensities. The coherence term, being

a complex number, contains phase information that needs to be detected through interference measurements, where the phase can be converted into detectable quantities, in other words, into population terms. This process of converting phase to population can also be considered as changing the measurement basis.

The measurement basis can be changed through active or passive rotations. A passive rotation is done by fixing the position of the state vector of the quantum system and physically altering the geometry of the measurement device to align the detection axis with the state vector (Figure 5.1(a)). An example of passive rotation is the use of the Stern-Gerlach apparatus [141]. Although passive rotations might seem more straightforward and less intrusive for the quantum system being measured, it is in general difficult to change the axis of measurement.

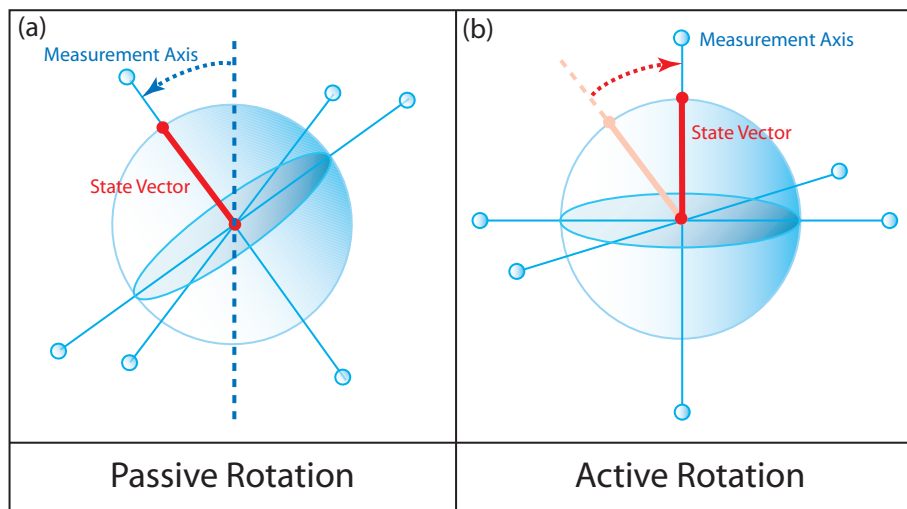


**Figure 5.1:** Passive and active rotations to change the measurement basis. (a) Passive rotation rotates the measurement axis while leaving the state vector (solid red line) fixed. (b) Active rotation rotates the state vector itself while leaving the measurement axis fixed.

An alternative and more practical method to change the measurement basis is through the active rotation of the state vector of the quantum system. Active rotation is achieved by fixing the measurement axis while rotating the state vector to the axis of measurement (Figure 5.1(b)). Physically, this rotation is performed by an external excitation field phase-locked to the quantum state being rotated. The technique of phase sensitive rotations discussed in Chapter 4 is an essential tool for this task.



The mathematical representation of the active rotation can be derived using the same formulism presented in Section 4.1 of Chapter 4. The transformation from an initial density matrix state,  $\rho_0$ , to its final state,  $\rho_r$ , by an resonant ( $\delta = 0$ ) optical pulsed field with pulse area  $\theta$  and relative phase  $\phi$  is described by

$$\rho_r = \mathbf{T}(\theta, \phi)\rho_0\mathbf{T}^\dagger(\theta, \phi), \quad (5.2)$$

with

$$\mathbf{T}(\theta, \phi) = \begin{bmatrix} \cos \frac{\theta}{2} & -ie^{i\phi} \sin \frac{\theta}{2} \\ -ie^{-i\phi} \sin \frac{\theta}{2} & \cos \frac{\theta}{2} \end{bmatrix}, \quad (5.3)$$

where  $\mathbf{T}(\theta, \phi)$  is the unitary transformation matrix representing the optical pulsed field. The expanded and simplified expression of  $\rho_r$  is

$$\rho_r = \begin{bmatrix} \rho_{00}^r & \rho_{01}^r \\ \rho_{10}^r & \rho_{11}^r \end{bmatrix} = \begin{bmatrix} C^2\rho_{00} + S^2\rho_{11} - SCIm\{e^{-i\phi}\rho_{01}\} & C^2\rho_{01} + e^{i2\phi}S^2\rho_{10} + iSCe^{i\phi}(\rho_{00} - \rho_{11}) \\ C^2\rho_{10} + e^{-i2\phi}S^2\rho_{01} - iSCe^{-i\phi}(\rho_{00} - \rho_{11}) & C^2\rho_{11} + S^2\rho_{00} + SCIm\{e^{-i\phi}\rho_{01}\} \end{bmatrix}, \quad (5.4)$$

where  $C = \cos \frac{\theta}{2}$  and  $S = \sin \frac{\theta}{2}$ . Equation 5.4 is used in the next section to calculate the real and imaginary components of the coherence term,  $\rho_{01}$ , for specific values of  $\theta$  and  $\phi$ .

## 5.2 Density matrix tomography of a single exciton-based qubit

The density matrix tomography experiment is conducted on the sample NRL-1197King, which contains the same interface fluctuation dots used in the phase sensitive rotation experiment discussed in Chapter 4. The exciton state described in Chapter 4 is a good candidate for the tomographic measurement since it exhibits a predictable optical response in the presence of coherent pulsed excitation. Furthermore, it shows the capability for sustaining coherence information imprinted by the optical field.

The laser system used in this experiment is the Mira system from Coherent<sup>TM</sup>. The Mira laser system consist of a passively modelocked Ti:Sapphire laser (MIRA)

pumped by a diode laser (Verdi-10). The MIRA laser operating in the fs mode produces 130 fs pulse at a 76 MHz repetition rate. This ultrafast pulse has wide spectral bandwidth which is well-suited for the application of pulse shaping.

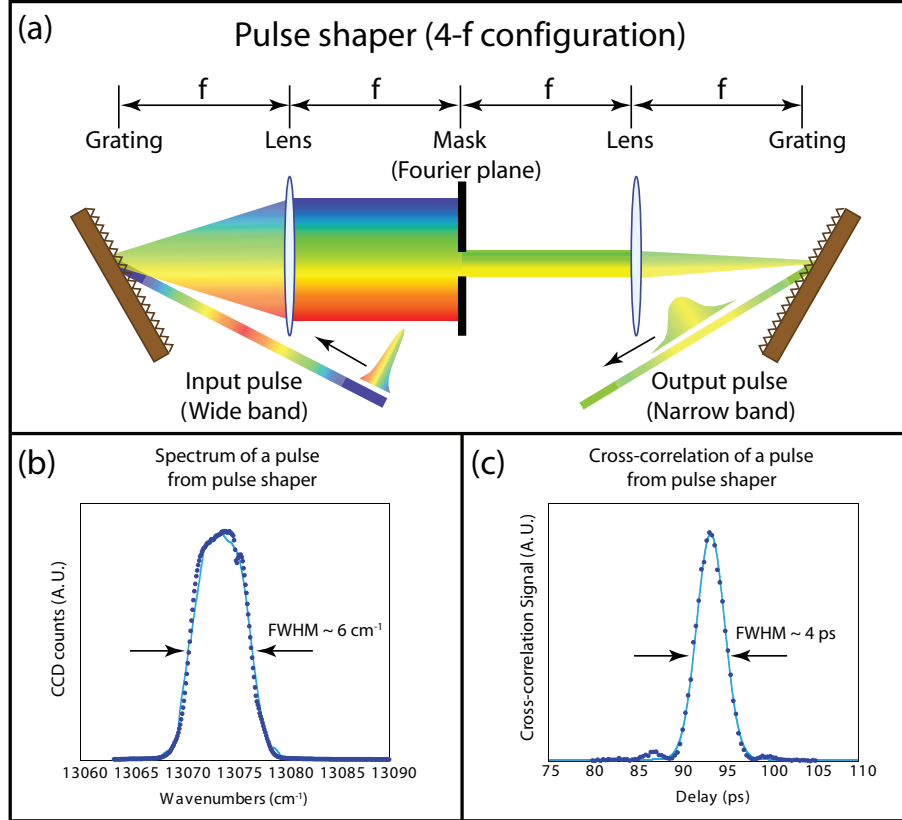


**Figure 5.2:** (a) Pulse shaper in 4-f configuration. The higher frequency is represented by the color blue, and the lower frequency is represented by the color red. (b) Spectrum of the shaped pulse after the pulse shaper. The FWHM is  $6 \text{ cm}^{-1}$ , corresponding to a energy bandwidth of  $0.75 \text{ meV}$ . (c) Cross-correlation of the shaped pulse after the pulse shaper. The fit function to the pulse shape is a Gaussian function. The FWHM of the pulse is  $4 \text{ ps}$ .

The train of 130 fs pulses is passed through a beam splitter, and each beam is then sent through a pulse shaper in the 4-f configuration [142, 143] as illustrated in Figure 5.2(a). The pulse shapers give the advantage of both tunable pulse width and wavelength. In addition, the two pulse shaper configuration allows for degenerate and non-degenerate frequency domain studies. The full-width-half-maximum (FWHM) of the pulse used in the tomography experiment is  $4 \text{ ps}$  as shown in the cross-correlation measurement in Figure 5.2(c). The corresponding FWHM bandwidth of the pulse is

$6 \text{ cm}^{-1}$  in wavenumber and  $0.75 \text{ meV}$  in energy. The abrupt drop-off of the spectral tails in the frequency spectrum is due to the sharp edges of the slit on the mask in the Fourier plane. The Fourier transform of this spectral profile leads to fringes in the temporal tails, which are visible in the cross-correlation scan.

The rest of the experimental setup after the pulse shapers is identical to the setup in the phase-sensitive rotation experiment in Chapter 4. The two pulses derived from the Michelson interferometer with tunable temporal delay,  $\tau$ , and phase delay,  $\phi$ , are assigned as the preparation pulse and the rotation pulse. The single probe pulse then measures the exciton-based qubit system throughout the preparation and rotation process.

The reduced three-level  $\mathbf{V}$  system approximation used in Chapter 4 remains valid with the newly adapted pulse width of  $4 \text{ ps}$ . Since the bandwidth of this  $4 \text{ ps}$  pulse is  $\sim 0.75 \text{ meV}$ , which is still smaller than the binding energy of the biexciton ( $\sim 3.5 \text{ meV}$ ) [104], we can neglect transitions to the biexciton in this experiment as well, and focus on the transitions to the two exciton states.

We define the horizontally ( $\Pi_x$ ) polarized transition of the exciton as the qubit and the vertically ( $\Pi_y$ ) polarized transition as the readout state. The qubit states are labelled as  $|0\rangle$  and  $|1\rangle$ , respectively, and the readout state is labelled as  $|R\rangle$  in Figures 5.3(a) and (b).

### 5.2.1 Calibration and renormalization of the differential transmission signal

Before the tomography measurement can be made, we need to first establish a relationship between the DT signal and the populations of the qubit states,  $|0\rangle$  and  $|1\rangle$ . A direct correspondence between these two quantities is completed through a calibration scheme implemented with the readout state  $|R\rangle$ .

Theoretically, the calibration process can be achieved simply using a pair of pump and probe pulses. We first resonantly excite transitions between the qubit states with a pump pulse of known pulse area,  $\theta$ . The weak probe ( $\theta < \frac{\pi}{2}$ ) then measures the

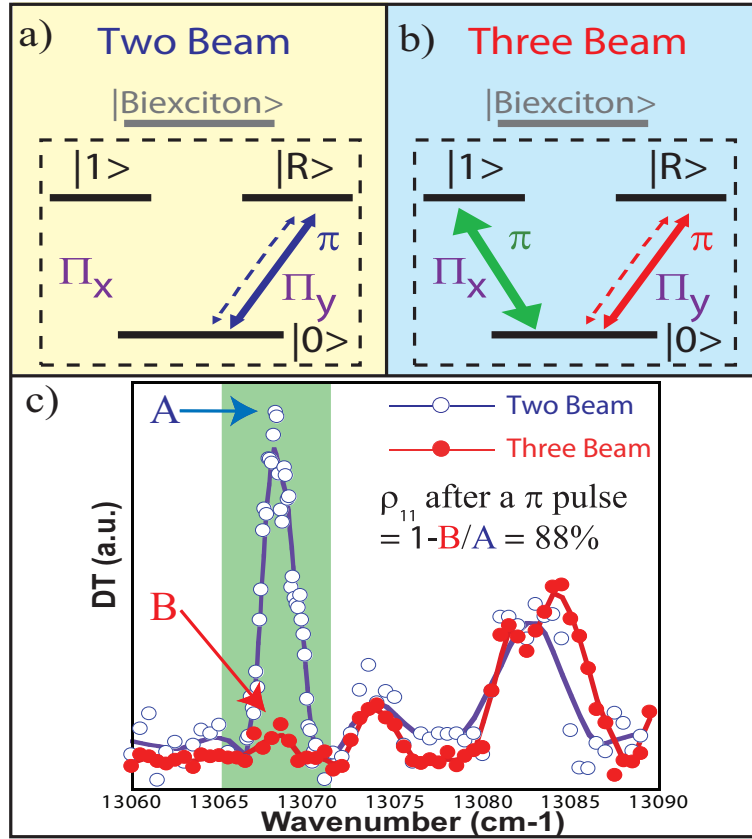


**Figure 5.3:** (a) and (b) Four-level representation. (a) Two-beam setup. (b) Three-beam setup.  $|0\rangle$  and  $|1\rangle$  are the crystal ground state and the qubit exciton, respectively, while  $|R\rangle$  is the readout exciton. The arrows in (a) and (b) denote the laser pulses, where the dashed lines are the probes, the normal solid lines are the pumps and the thick solid line is the pre-pump. (c) DT signal obtained by using the two-beam (blue open circle) and three-beam (red solid circle) setups. The state where the pre-pump is fixed is highlighted in green. We indicate that a  $\pi$  pulse inverts 88% of the population to state  $|1\rangle$ , leaving 12% in state  $|0\rangle$ .

population of the  $|0\rangle$  state. The DT signal, which is the signal with the pump off minus the signal with the pump on, is proportional to  $1 - \rho_{00}$  (Chapter 4, Section 4.3). Since the two-level qubit system in a single dot is shown to be a closed system [131], which means  $\rho_{11} + \rho_{00} = 1$ , the signal is linearly proportional to  $\rho_{11}$ . Without decay, this is sufficient to completely calibrate the DT signal. However, in a physical system, due to the finite pulse width of 4 ps and the short relaxation time of the exciton at 60 ps, a  $\pi$  pulse does not invoke a complete population inversion from state  $|0\rangle$  to  $|1\rangle$ . Hence, we must take the reality of the experiment into consideration.

A pair of experiments is conducted to measure the actual amount of population transferred to state  $|1\rangle$  for a  $\pi$  pulse. First, a two-beam setup is used to drive transitions between states  $|0\rangle$  and  $|R\rangle$  [thin blue solid and dashed arrows in Figure 5.3(a)], where the solid (dashed) arrow represents the pump (probe). The pump and probe with the same optical frequency are scanned in frequency, where the pump is set at a pulse area of  $\pi$  and the probe is kept weak below a pulse area of  $\pi/2$ . The pump and probe are temporally separated by 10 ps to avoid any contribution from coherent artifacts. The DT signal is recorded as the blue open circle plot in Figure 5.3(c), where the exciton transition of interest is highlighted in green. We denote the signal strength of this measurement as  $\mathbf{A}$ . This two-beam experiment can be viewed as a measurement of remaining population in  $|0\rangle$  when a  $\theta = 0$  pulse is used to excite the qubit states.

To measure the signal due to the remaining population in  $|0\rangle$  after a  $\theta = \pi$  pulse excitation, a three-beam setup is used. A pre-pump with pulse area  $\pi$  is fixed in frequency at the  $|0\rangle$  to  $|1\rangle$  transition [thick green solid arrow in Figure 5.3(b)], and transfers the maximum population to state  $|1\rangle$ . A pump and probe pair similar to the two-beam experiment [thin red solid and dashed arrows in Figure 5.3(b)], is delayed 10 ps from the pre-pump and scanned in frequency to read the population in state  $|0\rangle$  by driving transitions to state  $|R\rangle$ . The result is recorded as the red solid circle plot in Figure 5.3(c). The signal strength of the highlighted state in this experiment is denoted as  $\mathbf{B}$ .

The value of  $\mathbf{A}$  represents signal corresponding to remaining population in  $|0\rangle$  of  $\rho_{00} = 1$ , since the pre-pump pulse area is  $\theta = 0$ . On the other hand, the value of  $\mathbf{B}$  corresponds to a remaining population of  $\rho_{00} = \zeta$  in  $|0\rangle$  after a  $\theta = \pi$  pre-pump pulse. The percentage of remaining population in  $|0\rangle$  after a  $\pi$  pulse excitation is then simply the ratio of  $\frac{\mathbf{B}}{\mathbf{A}} \times 100 = \zeta \times 100 = 12\%$ . Therefore, we conclude that the maximum population transferred by a 4 ps wide  $\pi$  pulse is  $1 - \frac{\mathbf{B}}{\mathbf{A}} = 88 \pm 1\%$ . A simulation using the experimental parameters gives the result of an 85% population transfer, which is in excellent agreement with the data.

The calibration result obtained in this section is used to renormalize the DT signal

in the remainder of the chapter.

### 5.2.2 Reconstruction of the single qubit density matrix

We demonstrate the ability to measure the off-diagonal matrix elements ( $\rho_{01}, \rho_{10}$ ) as well as the diagonal density matrix elements ( $\rho_{00}, \rho_{11}$ ) of a closed two-level system, which leads to a complete mapping of the density matrix of a qubit in a single QD. To obtain the coherence terms, we use the active rotation method discussed in Section 5.1 to rotate the components in the  $\mathbf{u}\text{-}\mathbf{v}$  plane onto the measurement axis  $\hat{\mathbf{w}}$  through an optical excitation of  $\theta = \pi/2$ . By choosing the right phase of this optical rotation field, we can easily extract both the real and imaginary parts of the coherence terms.

From the equation of motion, the time evolution of the Bloch vector  $\vec{\mathbf{U}}$  is a precession around the field vector  $\vec{\mathbf{R}}$  by an angle of the pulse area of the field. We utilize this precession in a controlled manner to extract the real and imaginary parts of the coherence terms. From the Bloch sphere representation, we can clearly see that the real (imaginary) components of the field and coherence lie on the  $\hat{\mathbf{u}}$  ( $\hat{\mathbf{v}}$ ) axis. A purely real field rotates only the imaginary part of the coherence to the  $\hat{\mathbf{w}}$  axis for measurement (Figure 5.4(a)). Similarly, a purely imaginary field ( $\phi = \pi/2$ ) only measures the real part of the coherence (Figure 5.4(b)).

Mathematically, we refer to the Equation 5.4 in Section 5.1. For  $\theta = \frac{\pi}{2}$ , the new density matrix elements are simple expressions of the original density matrix elements. The simplification of this equation takes into account the closed system relation of  $\rho_{11} + \rho_{00} = 1$ . The simplified expression of the new density matrix,  $\rho_r$ , is

$$\begin{bmatrix} \rho_{00}^r & \rho_{01}^r \\ \rho_{10}^r & \rho_{11}^r \end{bmatrix} = \begin{bmatrix} \frac{1}{2} - \text{Im}\{e^{-i\phi}\rho_{01}\} & \frac{1}{2}[\rho_{01} + e^{i2\phi}\rho_{10} + ie^{i\phi}(\rho_{00} - \rho_{11})] \\ \frac{1}{2}[\rho_{10} + e^{-i2\phi}\rho_{01} - ie^{-i\phi}(\rho_{00} - \rho_{11})] & \frac{1}{2} + \text{Im}\{e^{-i\phi}\rho_{01}\} \end{bmatrix}. \quad (5.5)$$

Since the DT signal is calibrated to the density matrix element of  $\rho_{11}$ , we only need to concentrate on  $\rho_{11}^r$ , where

$$\rho_{11}^r = \frac{1}{2} + \text{Im}\{e^{-i\phi}\rho_{01}\}. \quad (5.6)$$

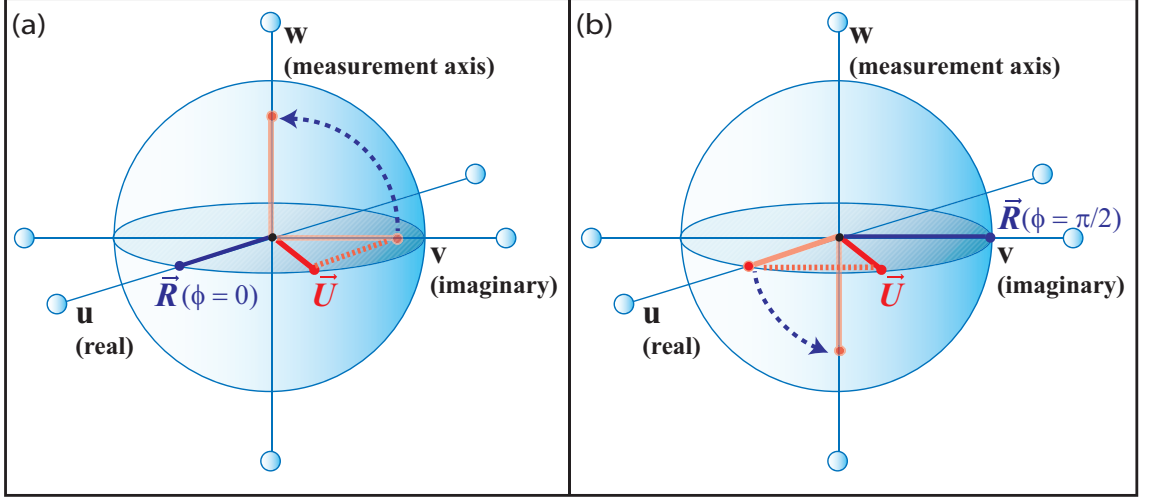


**Figure 5.4:** Rotating and measuring the coherence components of a Bloch vector (red),  $\vec{U}$ . (a) At  $\phi = 0$ , the pseudo-field vector (blue),  $\vec{R}$  is aligned along the  $\hat{u}$  (real) direction, and rotates the imaginary component of  $\vec{U}$  (pink) to the  $\hat{w}$  (measurement) axis. Similarly, (b at  $\phi = \frac{\pi}{2}$ , the pseudo-field vector,  $\vec{R}$  is aligned along the  $\hat{v}$  (imaginary) direction, and rotates the real component of  $\vec{U}$  (pink) to the  $\hat{w}$  (measurement) axis.

For  $\phi = 0$ ,  $\rho_{11}^r = 1/2 + Im[\rho_{01}]$ . Similarly, for  $\phi = \frac{\pi}{2}$ ,  $\rho_{11}^r = 1/2 - Re[\rho_{01}]$ . From these two values of  $\phi$ , the real and imaginary components of the coherence term of the original density matrix,  $\rho_{01}$ , can be extracted directly from the DT signal calibrated and renormalized to  $\rho_{11}^r$ .

Experimentally, we demonstrate the application of single qubit density matrix tomography on the maximum coherent state of a two-level system,  $|\psi_{\pi/2}\rangle = (|0\rangle - i|1\rangle)/\sqrt{2}$ , created by a  $\pi/2$  pulse. For a delta function pulse excitation and no decoherence presence, the ideal value of the density matrix,  $\rho_{ideal}$ , of this maximum coherent state is

$$\rho_{ideal} = \begin{bmatrix} 0.5 & i0.5 \\ -i0.5 & 0.5 \end{bmatrix}. \quad (5.7)$$

In the Bloch sphere representation, the Bloch vector,  $\vec{U}$ , for this state lies along the  $\hat{v}$  axis, with only imaginary component in the coherence term.

The population terms of state  $|\psi_{\pi/2}\rangle$ ,  $\rho_{00}$  and  $\rho_{11}$ , are directly measured through a two-beam experiment, where the preparation pulse of  $\theta = \frac{\pi}{2}$  prepares the state and the probe reads the value of  $\rho_{11} = 0.36 \pm 0.05$  through calibrated DT signal as shown

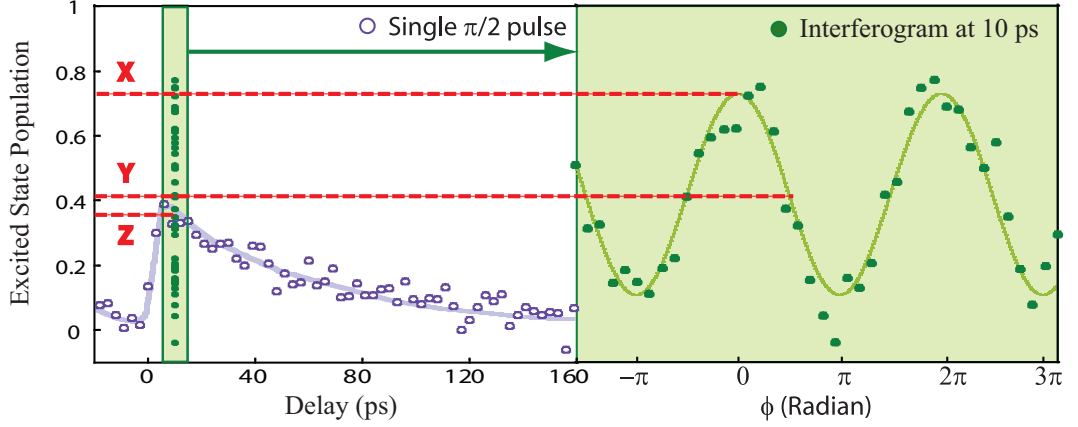


**Figure 5.5:** Decay plots of single  $\pi/2$  pulse and interferogram taken at 10 ps delay from the creation pulse. The horizontal dash lines mark the values of each population readout. **X** gives  $\rho_{11}^r = 0.73$ , **Y** gives  $\rho_{11}^r = 0.42$  and **Z** gives  $\rho_{11} = 0.36$ .

in Figure 5.5. The ground state population of  $\rho_{00} = 0.64 \pm 0.05$  is inferred for this closed system.

To measure the coherence terms ( $\rho_{01}$  and  $\rho_{10}$ ), a  $\pi/2$  rotation pulse is inserted after the preparation pulse to rotate the coherence components to the measurement axis  $\hat{\mathbf{w}}$ . The preparation pulse is temporally separated from the other pulses by 10 ps to avoid interfering with the preparation of the original state. The values of  $\rho_{11}^r = 0.73 \pm 0.03$  at  $\phi = 0$  and  $\rho_{11}^r = 0.42 \pm 0.03$  at  $\phi = \pi/2$  can be obtained through the calibrated interferogram shown in Figure 5.5. Using Eq. 5.6 and values from Figure 5.5, the imaginary part of  $\rho_{01}$  of state  $|\psi_{\pi/2}\rangle$  is simply  $0.23 \pm 0.03$  and the real part is  $0.08 \pm 0.03$ . The reconstruction of the measured density matrix,  $\rho_{meas}$ , for  $|\psi_{\pi/2}\rangle$  is then

$$\rho_{meas} = \begin{bmatrix} 0.64 \pm 0.05 & 0.08 + i0.23(\pm 0.03) \\ 0.08 - i0.23(\pm 0.03) & 0.36 \pm 0.05 \end{bmatrix}. \quad (5.8)$$

This density matrix is also presented in pictorial form in Figure 5.5(d) along side the ideal density matrix in Figure 5.5(a). We can see that the values are notably different in the two matrices, especially the appearance of the non-zero real component of the coherence term in the measured density matrix,  $\rho_{meas}$ .

To trace the source of the large discrepancies, two theoretical simulations are



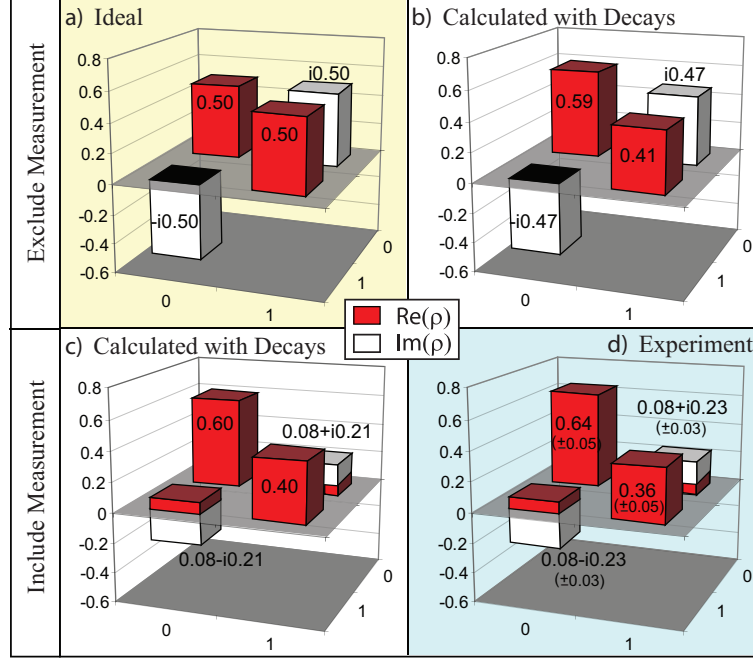


**Figure 5.6:** Density matrices of a single qubit created by a  $\pi/2$  pulse. (a) Ideal matrix. (b)[(c)] Calculated density matrices with decays excluding (including) rotation and probe pulses. (d) Measured density matrix from experiment.

performed The first simulation is of the actual experiment, which takes into account the entire process of preparation, rotation and measurement, as well as the decay parameters of the exciton quantum system. The density matrix,  $\rho_{\text{expsim}}$ , from the simulation result is

$$\rho_{\text{expsim}} = \begin{bmatrix} 0.60 & 0.08 + i0.21 \\ 0.08 - i0.21 & 0.40 \end{bmatrix}, \quad (5.9)$$

and displayed in Figure 5.6(c). The excellent agreement between  $\rho_{\text{meas}}$  and  $\rho_{\text{expsim}}$  signifies that we have complete knowledge of the quantum system used and that its behavior under optical excitation is completely theoretically predictable.

Based on the conclusion from the comparison between the first simulation and the actual experiment data, the following simulation result is a valid gauge for the actual density matrix of the exciton qubit created by a 4 ps  $\frac{\pi}{2}$  pulse. This second simulation models the density matrix without the measurement process, i.e. the rotation and probe pulses. However, parameters of the preparation pulse and the exciton system are still used in the calculation. The value of the density matrix,  $\rho_{\text{prepsim}}$ , created

with only the preparation pulse, is

$$\rho_{prepsim} = \begin{bmatrix} 0.59 & i0.47 \\ -i0.47 & 0.41 \end{bmatrix}, \quad (5.10)$$

and is shown in Figure 5.6(c). The values of the matrix elements are much closer to the values of the ideal matrix. As a result, we can attribute the large discrepancies between the coherence terms in these density matrices to the measurement process represented by the rotation and measurement pulses.

We observe that the population terms of all three non-ideal density matrices are essentially the same. However, the coherence terms of the density matrices with the inclusion of the rotation pulse stray from their ideal values. Specifically, in the presence of the rotation pulse, the coherence terms have non-zero real components, while in the absence of a rotation pulse, they are purely imaginary regardless of the qubit lifetime. This apparent discrepancy arises from the short decoherence of the system and the temporal overlap of the first and the second pump pulses. Although the two 4 ps wide pump pulses are separated by 10 ps, the pulse tail of the first pulse and the pulse front of the second pulse overlap. The amount of overlap, though small, can still affect the accuracy of the measurement of the coherence terms. In the Bloch sphere representation, we can attribute the error to population decay and the simultaneous rotation of the Bloch vector by the preparation and rotation pulses, both of which lead to a non-zero real component in the measured coherence terms.

A single parameter defined as the fidelity,  $\mathbf{F}$ , can be used to quantify and compare the performance of the preparation and measurement process in each of the four different situations under which  $\rho_{ideal}$ ,  $\rho_{meas}$ ,  $\rho_{expsim}$ , and  $\rho_{prepsim}$  are obtained. The fidelity,  $\mathbf{F}$ , is normally used to describe the effectiveness of quantum gate operations [104]. The mathematical definition of the fidelity is  $\mathbf{F} = Tr[\rho_p \rho_I]$ , where  $\rho_p$  is the density matrix of the physical result, and  $\rho_I$  is the density matrix of what is ideally expected. The highest fidelity obtainable is unity.

Two values of the fidelity are calculated for each density matrix. The first value is a calculation of the fidelity using  $\rho_I = \rho_{ideal}$ . This value considers the entire process of preparation, rotation and measurement. The second calculation of the

fidelity uses  $\rho_I = \rho_{prepsim}$ , which only considers performance of the the rotation and measurement process. The different values are listed in Table 5.1, and it is clear that the majority of the errors are introduced in the measurement process including the rotation and measurement pulses.

$F = Tr[\rho_p \rho_I]$	$\rho_p$			
	$\rho_{ideal}$	$\rho_{prepsim}$	$\rho_{expsim}$	$\rho_{meas}$
$\rho_I = \rho_{ideal}$	1	0.97	0.71	$0.73 \pm 0.03$
$\rho_I = \rho_{prepsim}$	–	1	0.72	$0.74 \pm 0.02$

**Table 5.1:** Fidelities of single qubit density matrix tomography with  $\rho_I = \rho_{ideal}$ , which measures the fidelity of the entire preparation and measurement process, and  $\rho_I = \rho_{prepsim}$ , which measures the fidelity of only the measurement process.

We can minimize errors by following the same suggestions at the end of Section 4.3 in Chapter 4. The remedies include shorter pulses and quantum system with longer decoherence time, such as the spin system (see Chapter 6), which has decoherence time of four orders of magnitude longer [106, 107, 109, 137].

### 5.3 Chapter summary

In summary, we have demonstrated the tomographic reconstruction of the density matrix of a single qubit as well as consecutive arbitrary qubit rotations. These measurements can be easily extended to map the complete physical density matrix of multi-qubit systems as in reference [104]. Even though the measurement accuracy is limited by the intrinsic decay parameters of the quantum system, the technique itself is proven to be suitable and practical for the purpose of density matrix tomography. Improved performance in optically driven spin based systems [111] is anticipated. The next chapter (Chapter 6) provides a glimpse into the ample potential of electron spin based qubits in QDs.

## CHAPTER 6

### Selective Optical Control of Electron Spin Coherence in Singly Charged Quantum Dots via Optically Dark and Bright States

In the previous chapters (Chapters 4 and 5), we have demonstrated the ability of the exciton-based quantum bit (qubit) to maintain and propagate quantum information to a high order of accuracy during its lifetime. These preliminary results prove that single qubit manipulation in a semiconductor quantum system is indeed achievable. Although the exciton-based system itself decays too fast for practical quantum information processing and is non-scalable, it sets the stage for the more robust and scalable spin-based system, represented by a single electron spin confined in a single quantum dot (QD).

Unlike the qubit states of the exciton-based system, which consist of a ground state and an excited state, the qubit states of a spin-based system are the two orthogonal spin states of an electron, which are both in the ground states. The advantage of having two ground states as qubit states is that the lifetime of the qubit is not limited by radiative decay of an excited state. In fact, the lifetime of the spin has been measured to be on the order of milliseconds [106–108], making the electron spin an ideal realization of a qubit.

Electron spin rotations have already been demonstrated in surface gated dots using electrical gates [144], but the operation time is limited to a few microseconds by the microwave control on resonance with the spin states. Alternatively, ultrafast optical pulses are readily available. Manipulating the spin states with these pulses increases the gate operation speed and hence the number of operations during the spin

coherence lifetime. Fast operation rates are crucial for practical quantum information processing. Especially when fault tolerant quantum computation is considered, the successful execution of error correction procedures require a minimum of  $10^4 - 10^5$  quantum gate operations within the decoherence time of the quantum system [2]. With ultrafast optical pulses on orders of picoseconds, a spin system with decoherence time of milliseconds can easily accommodate  $10^8 - 10^9$  operations, and is well-qualified for implementing the fault tolerant quantum computation scheme.

In this chapter, we demonstrate phase sensitive partial rotations of the electron spin vector in an ensemble of singly charged QDs using picosecond pulses [145]. Similar rotations have been performed on electrons in quantum wells [146, 147]. The rotations are achieved through dark and bright spin ground states created by optically coupling to the charged exciton (trion) state. The properties of dark and bright here are not absolute but rather depends on the characteristics of the optical field used, in this case, the polarization of the field. This terminology originated from the field of atomic physics [148–151], and thus it is also appropriate for the atomic-like system in a single QD. Accomplishing the partial rotations prepares the way for the demonstration of complete rotations of a single spin, which would encompass arbitrary qubit rotations.

We start the chapter by discussing the theory of stimulated Raman transitions in a  $\Lambda$  three-level system used to model the spin-trion complex. Both probability amplitude and density matrix approaches are used to derive the spin coherence term responsible for the quantum beat phenomenon observed in the spin system. Concurrently, the creation and definition of optically bright and dark spin states are also brought into attention to aid later understanding of the partial rotation experiment. Following the theoretical derivation of the spin quantum beats, we review the experimental measurement process of the spin coherence signal via ultrafast optical pulses. And finally, we conclude by analyzing the experimental data on the initialization and partial rotation of the electron spin.

## 6.1 Theory on stimulated Raman transitions and ground state coherence in a $\Lambda$ system

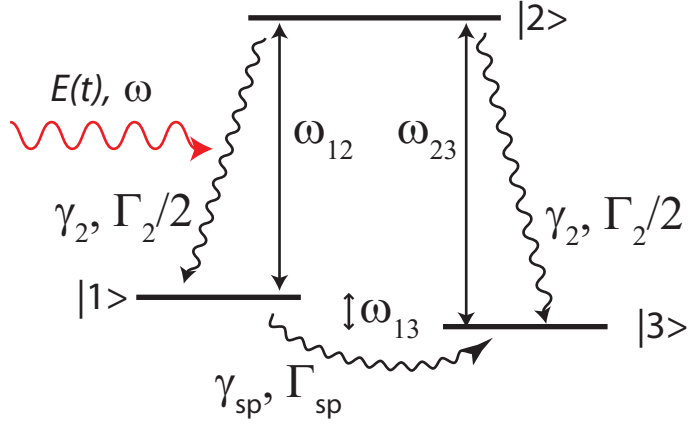


**Figure 6.1:** Diagram of a closed three-level  $\Lambda$  system.  $\omega_{12}$  ( $\omega_{23}$ ) is the transition frequency between states |2> and |1> (|3>).  $\omega_{13} = \omega_{23} - \omega_{12}$  is the frequency difference between states |1> and |3>.  $\mathbf{E}(t)$  is the excitation field with frequency  $\omega$ .  $\Gamma_2$  ( $\gamma_2$ ) is the population decay (decoherence) rate between the excited state and the ground states, and it is assumed to be equal for both transitions.  $\Gamma_{sp}$  ( $\gamma_{sp}$ ) is the population decay (decoherence) rate between the ground states.

In a singly charged QD, the optical transitions between the two spin ground states and an excited trion state can be modelled by a three-level  $\Lambda$  system. This energy level configuration can be viewed as two two-level systems sharing an excited state as shown in Figure 6.1. Astonishingly, the simple addition of a second ground state brings forth a new class of physical phenomena nonexistent in the two-level system. A few well-known phenomena observed in a  $\Lambda$  system include coherent population trapping [128, 152, 153], electromagnetically induced transparency (EIT) [154–158], and lasing without inversion [159–164]. These phenomena are direct results of a dark state generated by the coherence between the ground states through stimulated Raman transitions. In Section 6.2, we demonstrate the importance of this optical dark state in the coherent control of a spin state.

This section explores the physics of a three-level  $\Lambda$  system, with a focus on the generation of ground state coherence, using the exact solutions in the probability amplitude picture (Subsection 6.1.1) and the perturbative solutions in the density matrix picture (Subsection 6.1.2). In Subsection 6.1.1, the mathematical derivation

of an optically dark state is shown under specific excitation condition. In Subsection 6.1.2, we analyze the perturbation pathways that give rise to the experimental signals using the density matrix equations.

### 6.1.1 Exact solutions in the probability amplitude approach

A general state in the three-level  $\Lambda$  system in Dirac notation is  $|\psi\rangle = a_1|1\rangle + a_2|2\rangle + a_3|3\rangle$ , where  $a_1$ ,  $a_2$  and  $a_3$  are probability amplitudes for states  $|1\rangle$ ,  $|2\rangle$  and  $|3\rangle$ , respectively. With the application of the rotating wave approximation (RWA) and the absence of decays, the Schrödinger equations of motion for the probability amplitudes in the field interaction representation, are  $c_1(t)$ ,  $c_2(t)$  and  $c_3(t)$  (see conversion and definitions in Chapter 3), where

$$\begin{aligned}\dot{c}_1(t) &= -i\chi^*(t)c_2(t) - i\frac{\omega_{13}}{2}c_1(t) \\ \dot{c}_2(t) &= -i\chi(t)[c_1(t) + c_3(t)] \\ \dot{c}_3(t) &= -i\chi^*(t)c_2(t) + i\frac{\omega_{13}}{2}c_3(t).\end{aligned}\tag{6.1}$$

The single optical field  $\mathbf{E}(t)$  with frequency  $\omega$  is tuned to the excited state  $|2\rangle$  from the halfway point of states  $|1\rangle$  and  $|3\rangle$ . The frequency difference between states  $|1\rangle$  and  $|3\rangle$  is  $\omega_{13} = \omega_{23} - \omega_{12}$ . The optical field related term is  $\chi(t) = -\frac{\boldsymbol{\mu}_2 \cdot \mathbf{E}(t)}{2\hbar}$ , with the same dipole moment,  $\boldsymbol{\mu}_2 = \boldsymbol{\mu}_{12} = \boldsymbol{\mu}_{32}$ , for both  $1 \leftrightarrow 2$  and  $2 \leftrightarrow 3$  transitions.

For a real optical square pulse,  $\chi(t) = \chi^*(t) = \chi$ , Equation 6.1 can be rewritten in a more simple and solvable form as followed,

$$\begin{aligned}\dot{c}_+(t) &= -i\left[\sqrt{2}\chi c_2(t) + \frac{\omega_{13}}{2}c_-(t)\right] \\ \dot{c}_2(t) &= -i\sqrt{2}\chi c_+(t) \\ \dot{c}_-(t) &= -i\frac{\omega_{13}}{2}c_+(t),\end{aligned}\tag{6.2}$$

where  $c_{\pm}(t) = [c_1(t) \pm c_3(t)]/\sqrt{2}$ , with corresponding states of  $|\pm\rangle = (|1\rangle \pm |3\rangle)/\sqrt{2}$ . A closer look at Equation 6.2 reveals that the equation of motion for  $c_-(t)$  does not contain the optical field term,  $\chi$ . This observation indicates that the state is not directly coupled to the optical field, but is rather driven indirectly through the directly coupled state  $|+\rangle$ . We show later in this discussion how state  $|-\rangle$  can become an optically dark state under certain conditions of the optical field.

The general solution to Equation 6.2 is derived in Appendix B. The probability amplitudes from Equation B.7 are,

$$\begin{aligned} c_+(t) &= \cos \Omega t c_+(0) - i \frac{\omega_{13}}{2\Omega} \sin \Omega t c_-(0) - i \frac{\sqrt{2}\chi}{\Omega} \sin \Omega t c_2(0) \\ c_2(t) &= -i \frac{\sqrt{2}\chi}{\Omega} \sin \Omega t c_+(0) - \frac{\sqrt{2}\chi\omega_{13}}{\Omega^2} \sin^2 \frac{\Omega t}{2} c_-(0) + \left[ \frac{\omega_{13}^2}{4\Omega^2} + \frac{2\chi^2}{\Omega^2} \cos \Omega t \right] c_2(0) \\ c_-(t) &= -i \frac{\omega_{13}}{2\Omega} \sin \Omega t c_+(0) + \left[ \frac{2\chi^2}{\Omega^2} + \frac{\omega_{13}^2}{4\Omega^2} \cos \Omega t \right] c_-(0) - \frac{\sqrt{2}\chi\omega_{13}}{\Omega^2} \sin^2 \frac{\Omega t}{2} c_2(0), \end{aligned} \quad (6.3)$$

where  $\Omega = \sqrt{2\chi^2 + \frac{\omega_{13}^2}{4}}$ . This set of general solutions provides the ability to investigate behaviors of the  $\Lambda$  system under various excitations and initial conditions.

One particular interesting combination of excitation and initial parameters is from the spin control experiment in Section 6.2. The optical field used in the experiment consists of ultrafast pulses, where the bandwidth of the pulses is much greater than the energy separation between states  $|1\rangle$  and  $|3\rangle$  (i.e.  $\Delta\omega \gg \omega_{13}$ ). As a result, both states are excited resonantly, and terms related to  $\omega_{13}$  are negligible. Consequently, Equation 6.3 can be written in a more simple form,

$$\begin{aligned} c_+(t) &= \cos \Omega t c_+(0) - i \sin \Omega t c_2(0) \\ c_2(t) &= -i \sin \Omega t c_+(0) + \cos \Omega t c_2(0) \\ c_-(t) &= c_-(0), \end{aligned} \quad (6.4)$$

with  $\Omega = \sqrt{2}\chi$ . It is immediately apparent that  $c_-(t)$  is independent of any field related terms and maintains its initial value of  $c_-(0)$ . Such behavior is indicative of an optically dark state. In this case, the dark state associated with  $c_-(t)$  is  $|-\rangle$ . The emergence of this dark state reduces the three-level  $\Lambda$  system to a simple two-level system between states  $|+\rangle$  and  $|2\rangle$ . This simplification enables the extraction of three-level physics of a  $\Lambda$  system through the less complicated formalism of a two-level system.

For the convenience of later discussion, Equation 6.4 is rewritten in the matrix form of  $\vec{c}(t_p) = \mathbf{T}(\theta(t_p)) \vec{c}(0)$  with the unitary time evolution operator  $\mathbf{T}(\theta(t_p))$ ,

$$\begin{bmatrix} c_-(t_p) \\ c_+(t_p) \\ c_2(t_p) \end{bmatrix} = \begin{bmatrix} 1 & 0 & 0 \\ 0 & \cos \frac{\theta(t_p)}{2} & -i \sin \frac{\theta(t_p)}{2} \\ 0 & -i \sin \frac{\theta(t_p)}{2} & \cos \frac{\theta(t_p)}{2} \end{bmatrix} \begin{bmatrix} c_-(0) \\ c_+(0) \\ c_2(0) \end{bmatrix}, \quad (6.5)$$



where  $\theta(t_p) = 2\Omega t_p = 2\sqrt{2}\chi t_p$  is the pulse area for a square pulse with pulse duration  $t_p$ . The pulse area  $\theta(t_p)$  here is a factor of  $\sqrt{2}$  larger than that of a true two-level system. The factor of  $\sqrt{2}$  comes from the fact that the “ground state” of the reduced two-level system actually consists of two states,  $|1\rangle$  and  $|3\rangle$ . Similar to the two-level calculations in Chapter 4, the pulse area  $\theta$  in Equation 6.5 can be the generalized pulse area of any well-defined pulse shape, as long as the duration of the pulse is much shorter than the characteristic time scales of evolution in the quantum system.

In order to apply the general initial conditions for both mixed and pure states, we must do so in the density matrix picture. The initial values of the populations and coherence are chosen to match that of the spin-trion system in the experiment. Under no optical excitation, the system is in a completely mixed state of the two ground states,  $|1\rangle$  and  $|3\rangle$ , meaning  $\rho_{11}(0) = \rho_{33}(0) = \rho_{++}(0) = \rho_{--}(0) = \frac{1}{2}$ , and  $\rho_{22}(0) = \rho_{13}(0) = \rho_{32}(0) = \rho_{12}(0) = \rho_{+-}(0) = 0$ . It is also inferred that  $\rho_{11}(0) + \rho_{33}(0) = \rho_{++}(0) + \rho_{--}(0) = 1$  for a closed system. The density matrix elements, taking into account the above initial conditions and given values of probability amplitudes from Equation 6.5, are

$$\begin{aligned}
\rho_{++}(t_p) &= c_+^*(t_p)c_+(t_p) = \cos^2 \frac{\theta(t_p)}{2} \rho_{++}(0) \\
\rho_{22}(t_p) &= c_2^*(t_p)c_2(t_p) = \sin^2 \frac{\theta(t_p)}{2} \rho_{++}(0) \\
\rho_{--}(t_p) &= c_-^*(t_p)c_-(t_p) = \rho_{--}(0) \\
\rho_{+-}(t_p) &= c_-^*(t_p)c_+(t_p) = 0 \\
\rho_{13}(t_p) &= c_3^*(t_p)c_1(t_p) = \frac{1}{2} [\rho_{++}(t_p) - \rho_{--}(t_p)],
\end{aligned} \tag{6.6}$$

With  $\rho_{--}(t_p)$  being a constant, the magnitude of the ground state coherence  $\rho_{13}$  increases as more population in state  $|+\rangle$  is being excited to state  $|2\rangle$  (Figure 6.2(b)). This dependence of the coherence on the difference of the  $|\pm\rangle$  state population becomes physically significant in the spin control experiment discussion in Section 6.2. In the normal representation,  $\rho_{13}^{norm}(t) = \rho_{13}(t_p)e^{-i\omega_{13}t}$  oscillates at the difference frequency  $\omega_{13}$  of the ground states. This oscillation gives rise to the quantum beat signals observed in later experiments.

Another method for generating the ground state coherence is through the adiabatic approach [165–170]. This approach relies on a strict excitation scheme to adiabati-

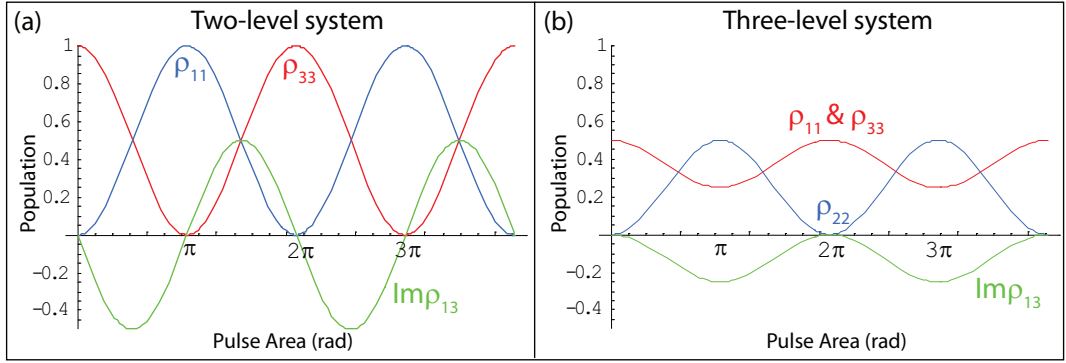


**Figure 6.2:** Density matrix elements as a function of pulse area in (a) two-level and (b) three-level  $\Lambda$  systems with resonant ultrafast optical coupling. In both cases,  $\rho_{13}$  is purely imaginary, so  $|\rho_{13}| = \text{Im}\rho_{13}$ .

cally eliminate the excited state in order to isolate the ground states as a two-level system. Such a scheme usually requires slow narrow-band pulses, which sacrifice speed of operation to satisfy the adiabatic conditions. Moreover, the coupling scheme is characterized by an unitary transformation for the two ground states, which means it is ineffective for a completely mixed initial state. The ultrafast method used here, on the other hand, actually utilizes the excited state and performs better for faster pulses [171]. In addition, since the ultrafast excitation couples to state  $|2\rangle$ , it is not an unitary transformation for the ground states, and coherence is created even for a completely mixed state. The maximum magnitude of the coherence reached for a completely mixed state is 0.25. To achieve the the ultimate maximum value of 0.5, the system needs to be completely initialized in either state  $|1\rangle$  or  $|3\rangle$  (one method of initialization is discussed in Subsection 6.2.1). Figure 6.2 gives a graphical summary of the populations and coherence of the ground states,  $|1\rangle$  and  $|3\rangle$ , in an isolated two-level system (Figure 6.2(a)), and in a three-level system with an intermediate excited state,  $|2\rangle$ , and a resonant ultrafast pulsed optical field (Figure 6.2(b)).

In this section, all discussions were mathematical. In later sections, we extend the discussion by assigning physical meanings to the mathematical entities using the spin-trion  $\Lambda$  system.

### 6.1.2 Perturbative solutions in the density matrix approach

In the previous subsection, the Schrödinger equations of motion for the  $\Lambda$  system are solved exactly to all orders for a resonant ultrafast pulse under no decay. In reality, the differential transmission (DT) technique used in the experiment only selectively measures terms that satisfy the modulation conditions used during signal processing, specifically, terms proportional to the third order susceptibility of the system. In order to pinpoint which terms are detected in the DT signal, we calculate the result using the perturbation process in the density matrix equations. For a complete study, population decays and coherence dephasing terms are included.

The density matrix equations in the field interaction picture under similar real square pulsed excitation conditions as in the previous subsection are

$$\begin{aligned}
\dot{\rho}_{11}(t) &= -i\chi [\rho_{21}(t) - \rho_{12}(t)] + \frac{\Gamma_2}{2} \rho_{22}(t) - \Gamma_{sp} \rho_{11}(t) \\
\dot{\rho}_{22}(t) &= i\chi [\rho_{21}(t) - \rho_{12}(t)] + i\chi [\rho_{23}(t) - \rho_{32}(t)] - \Gamma_2 \rho_{22}(t) \\
\dot{\rho}_{33}(t) &= -i\chi [\rho_{23}(t) - \rho_{32}(t)] + \frac{\Gamma_2}{2} \rho_{22}(t) + \Gamma_{sp} \rho_{11}(t) \\
\dot{\rho}_{12}(t) = \dot{\rho}_{21}^*(t) &= -i\chi [\rho_{22}(t) - \rho_{11}(t)] + i\chi \rho_{13}(t) - \gamma_2 \rho_{12}(t) \\
\dot{\rho}_{23}(t) = \dot{\rho}_{32}^*(t) &= i\chi [\rho_{22}(t) - \rho_{33}(t)] - i\chi \rho_{13}(t) - \gamma_2 \rho_{23}(t) \\
\dot{\rho}_{13}(t) = \dot{\rho}_{31}^*(t) &= -i\chi [\rho_{23}(t) - \rho_{12}(t)] - \gamma_{sp} \rho_{13}(t),
\end{aligned} \tag{6.7}$$

where  $\Gamma_2$  and  $\gamma_2$  are the population relaxation and decoherence rates of the excited state  $|2\rangle$ , which decays equally into states  $|1\rangle$  and  $|3\rangle$ . The spin population decay and decoherence rates are characterized by  $\Gamma_{sp}$  and  $\gamma_{sp}$ , respectively.

In the DT experiments, signals are often obtained using a pump ( $E_1$ ) and probe ( $E_2$ ) pair. The third order signal using two distinct optical fields contains many possible combinations of the two fields. The modulation configuration of the optical fields narrows the number of terms down to 24 as shown in Chapter 3. For time domain excitation using ultrafast pulses, the time ordering of the pulses puts additional constraints on the detectable terms. The term that satisfies all the above conditions is  $E_1^* E_1 E_2^*$ . This singular term contains information from two distinct perturbation pathways. One is a coherent path, which creates the second order ground state coherence ( $\rho_{13}^{(2)}$ ), and the other is a step-wise path, which creates the second order state

populations  $(\rho_{11}^{(2)}, \rho_{33}^{(2)})$ ,

$$\begin{array}{c}
 \text{Coherent :} \\
 \rho_{11}^{(0)} \quad \rho_{12}^{(1)} \quad \rho_{13}^{(2)} \quad \rho_{12}^{(3)} \\
 \rho_{33}^{(0)} \xrightarrow{E_1^*} \rho_{23}^{(1)} \xrightarrow{E_1} \rho_{13}^{(2)} \xrightarrow{E_2^*} \rho_{23}^{(3)} \\
 \hline
 \text{Step - wise :} \\
 \rho_{11}^{(0)} \quad \rho_{12}^{(1)} \quad \rho_{11}^{(2)} \quad \rho_{12}^{(3)} \\
 \rho_{33}^{(0)} \xrightarrow{E_1^*} \rho_{23}^{(1)} \xrightarrow{E_1} \rho_{33}^{(2)} \xrightarrow{E_2^*} \rho_{23}^{(3)}
 \end{array} \quad (6.8)$$

In the following discussion, we concentrate on the coherent pathway which gives rise to signal from the ground state coherence,  $\rho_{13}$ .

The zeroth order values of the density matrix elements are the initial conditions of a completely mixed state, where  $\rho_{11}^{(0)} = \rho_{33}^{(0)} = \frac{1}{2}$  while all the others are zero. To first order of the pump field ( $E_1^*$ ), the only nonzero density matrix elements given the initial conditions are the coherence between the excited state and the ground states,  $\rho_{12}^{(1)}$  and  $\rho_{23}^{(1)}$ . For the ultrafast pulse excitation assumed here, it is valid to represent the field envelope with a delta function,  $\chi = \chi_n \delta(t - \tau_n)$ , where  $n = 1, 2$  denotes the pump and probe fields, respectively. The first order solution is then

$$\begin{aligned}
 \rho_{12}^{(1)}(t) &= i\chi_1 \rho_{11}^{(0)} e^{-\gamma_2(t-\tau_1)} \Theta(t - \tau_1) \\
 \rho_{23}^{(1)}(t) &= -i\chi_1 \rho_{33}^{(0)} e^{-\gamma_2(t-\tau_1)} \Theta(t - \tau_1)
 \end{aligned} \quad (6.9)$$

where the unit step function

$$\Theta(t - \tau_1) = \begin{cases} 0, & t < \tau_1 \\ 1, & t \geq \tau_1 \end{cases} . \quad (6.10)$$

To second order of the pump field, coherence is created in the ground state,

$$\rho_{13}^{(2)}(t) = -|\chi_1|^2 e^{-\gamma_{sp}(t-\tau_1)} \Theta(t - \tau_1), \quad (6.11)$$

and decays at the rate of  $\gamma_{sp}$ . In the normal representation,  $\rho_{13}^{(2)}(t)$  oscillates at  $\omega_{13}$  as shown in Subsection 6.1.1, which is usually not in the optical detection frequency range. However, this coherence can be detected through optically radiative terms of  $\rho_{12}^{(3)}(t)$  and  $\rho_{32}^{(3)}(t)$  using a probe field ( $E_2$ ). In the coherent pathway, only the  $\rho_{13}^{(2)}(t)$  contribution to the third order radiative terms is considered. Because the probe pulse is delayed from the pump pulse, and the oscillation period of  $\rho_{13}^{(2)}(t)$  is on the order

of the temporal separation between the two pulses ( $\tau = \tau_2 - \tau_1$ ), the oscillation must be considered during the integration in the third order calculation. The final third order signal takes the form of

$$E_{sig}^{(3)} \propto \rho_{12}^{(3)}(t) + \rho_{32}^{(3)}(t) = -i2|\chi_1|^2\chi_2 \cos \omega_{13} (\tau_2 - \tau_1) e^{-\gamma_{sp}(\tau_2 - \tau_1)} e^{-\gamma_2(t - \tau_2)}. \quad (6.12)$$

By varying  $\tau = \tau_2 - \tau_1$ , which is the delay between the pump and probe pulses, the dynamics of the oscillation and decay of the ground state coherence can be monitored optically.

In the following experimental section, the exact solutions in the probability amplitude approach are used to explain the physics of the dynamics in the spin-trion system. The perturbation paths in the density matrix approach are used mainly to distinguish and assign the measured signals to corresponding system dynamics.

## 6.2 Optical coherent spin control experiment in singly charged quantum dots

### 6.2.1 Experimental setup and quantum beat signals

The sample used in the coherent spin control study is the 612F-2(ensemble), which is similar to the exciton sample in Chapter 4 and 5. It contains an ensemble of GaAs/Al<sub>0.3</sub>Ga<sub>0.7</sub>As interface fluctuation QDs [75, 88, 90]. The essential difference is that these dots are charged with single electrons through silicon  $\delta$ -doping. The number of electrons trapped in the dot is determined by the doping density of the sample. In this case, the doping density is  $10^{10}/\text{cm}^2$ , which gives an average of one electron per dot [112]. The sample is placed inside a Janis Research<sup>TM</sup> superconducting magneto cryostat, which cools the sample to 5 K. The magnetic field ( $B_x$ ) applied in the experiments is aligned in the Voigt geometry ( $\hat{x}$ ), perpendicular to the sample growth axis, which is in the  $\hat{z}$  direction.

The laser system used for the experiment is the Coherent<sup>TM</sup> Antares system as in Chapter 4, which gives 5 ps pulse duration. The experimental setup is similar to that

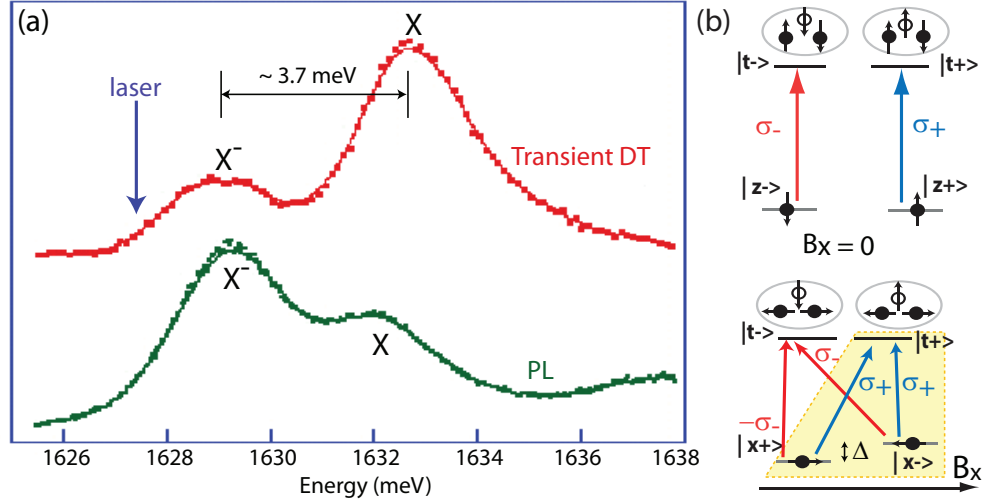


**Figure 6.3:** (a) Ensemble spectra of the 612F-2 sample in DT and photoluminescence (PL). The trion ( $X^{-1}$ ) and exciton ( $X$ ) peaks are separated by a binding energy of 3.7 meV. The blue arrow indicates the energy position of the laser for the spin coherent control experiment. (b) Energy level diagrams of a charged QD at  $B_x = 0$  T and  $B_x \neq 0$  T in the Voigt geometry. The blue and red arrows indicate the polarization selections of the transitions.

in Figure 4.3 in Chapter 4 without the Michelson interferometer. The pump and probe are each modulated at 1 Mhz and 1.05 Mhz. The energy spectrum of the ensemble sample can be either obtained through photoluminescence (PL) or nonlinear DT as shown in Figure 6.3(a). Two ensemble peaks shows up in both spectra. The higher energy peak is due to excitons and the lower energy peak is due to trions, and they are separated by a binding energy of 3.7 meV. For the transient DT experiments in this section, both pump and probe laser frequencies are tuned to the lower energy tail of the ensemble trion spectrum, as indicated by the blue arrow, to avoid simultaneous excitation of excitons.

The energy structure of the singly charged QD at  $B_x = 0$  T can be described by two degenerate two-level systems each consisting of one spin ground state and one trion excited state, as shown in Fig. 6.3(b). The total angular momentum projections along the  $\hat{z}$  axis of the spin ground states  $|z\pm\rangle$  are  $\pm\frac{1}{2}$ , defined by the electron spin, while those of the singlet trion states  $|t\pm\rangle$  are  $\pm\frac{3}{2}$ , defined by the hole spin. The electron spins do not contribute to the total angular momentum of the trion due to

the anti-pairing. The allowed optical transitions are then restricted to  $\Delta m = \pm 1$  for  $\sigma_{\pm}$  polarized excitations. This angular momentum restriction inhibits optical coupling between the two spin states.

Stimulated optical Raman coupling between the spin states via the trion states is enabled by applying a magnetic field in the Voigt geometry. This magnetic field also produces two new eigenstates of the electron spin,  $|x_{\pm}\rangle = (|z_{+}\rangle \pm |z_{-}\rangle)/\sqrt{2}$  parallel or antiparallel to  $\vec{x}$ , the magnetic field direction (Fig. 6.3(b)). The in-plane electron g-factor in this sample is  $g_e = 0.13$  [90,117] and thus the Zeeman splitting is approximately  $\Delta = 2g_e\mu_B B_x \sim 50\mu eV$  at 6.6 T, where  $\mu_B$  is the Bohr magneton.

In contrast, the highly suppressed mixing of the light and heavy hole states at even 6.6 T by the strong spin orbital coupling in this particular sample leads to a negligibly small in-plane hole g-factor [90]. This causes the hole spins to be pinned along the  $\hat{z}$  axis. Consequently, the trion states remain unaffected by the magnetic field. The spin ground states are now optically coupled through the trion states by either  $\sigma_{+}$  or  $\sigma_{-}$  polarized optical pulses (derivation of the transition selection rule is in Section 2.3, Chapter 2). Since the two  $\Lambda$  systems are essentially equivalent, without loss of generality we concentrate on the  $\sigma_{+}$  polarized  $\Lambda$  system highlighted in Fig. 6.3(b).

The 5 ps  $\sigma_{+}$  pulses have a bandwidth of  $\Omega \sim 0.37$  meV  $\gg \Delta$ , the Zeeman splitting, which couple both spin states ( $|x_{\pm}\rangle$ ) to the trion state ( $|t_{+}\rangle$ ) simultaneously and equally. Consequently, as discussed in Section 6.1, a pair of optically bright and dark states,  $|z_{\pm}\rangle = (|x_{+}\rangle \pm |x_{-}\rangle)/\sqrt{2}$ , are formed for the  $\sigma_{+}$  excitation. The transformation of the spin-trion  $\Lambda$  system under the  $\sigma_{+}$  optical pulses with pulse area  $\theta$ , can then be described by the unitary time evolution operator,

$$\mathbf{T}_{\sigma_{+}}(\theta) = \begin{bmatrix} 1 & 0 & 0 \\ 0 & \cos \frac{\theta}{2} & -i \sin \frac{\theta}{2} \\ 0 & -i \sin \frac{\theta}{2} & \cos \frac{\theta}{2} \end{bmatrix}, \quad (6.13)$$

in the  $|z_{\pm}\rangle$  basis, where the optically coupling is between the bright state  $|z_{+}\rangle$  and the trion state  $|t_{+}\rangle$ .

The initial state of the system is largely determined by the sample temperature

of 5 K. At a temperature of 5 K, the thermal excitation energy is  $k_b T = 430 \mu eV$ , which is an order of magnitude larger than the electron Zeeman splitting energy,  $\Delta$ , at 6.6 T. According to the MaxwellBoltzmann distribution, this results in a completely mixed state of the electron spin, which also means equal population in both spin ground states and zero spin coherence in any basis. The mixed initial state can only be represented with a density matrix,

$$\rho_0 = \begin{bmatrix} \rho_{z-,z-} = \frac{1}{2} & 0 & 0 \\ 0 & \rho_{z+,z+} = \frac{1}{2} & 0 \\ 0 & 0 & \rho_{t+,t+} = 0 \end{bmatrix}. \quad (6.14)$$

This completely mixed spin subspace is unaffected using only unitary transformations within this two-level system, such as that of the applied magnetic field  $B_x$ , where  $\mathbf{T}_{B_x}(\omega_L)\rho_0\mathbf{T}_{B_x}^\dagger(\omega_L) = \rho_0$ , and

$$\mathbf{T}_{B_x}(\omega_L) = \begin{bmatrix} \cos \frac{\omega_L t}{2} & -i \sin \frac{\omega_L t}{2} & 0 \\ -i \sin \frac{\omega_L t}{2} & \cos \frac{\omega_L t}{2} & 0 \\ 0 & 0 & 1 \end{bmatrix}, \quad (6.15)$$

with  $\omega_L = \frac{\Delta}{\hbar}$  is the Larmor precession frequency of the electron spin. Although in the experiment the static magnetic field is on at all time, because the state is mixed there is no net spin polarization to interact with the field, and therefore, no spin quantum oscillations.

Ultimately, the initialization of the spin out of the completely mixed state relies on an excitation outside of the spin subspace, in this case, the  $\sigma_+$  polarization pulse. The final initialized state immediately after the optical excitation is given by

$$\rho_I = \mathbf{T}_{\sigma_+}(\theta)\rho_0\mathbf{T}_{\sigma_+}^\dagger(\theta) = \begin{bmatrix} \frac{1}{2} & 0 & 0 \\ 0 & \frac{1}{2} - \xi & \varphi \\ 0 & \varphi^* & \xi \end{bmatrix}, \quad (6.16)$$

where  $\xi = \frac{1}{2} \sin^2 \frac{\theta}{2}$  is the population excited to the trion state  $|t+\rangle$ .  $\xi$  ranges from 0 to  $\frac{1}{2}$  depending on the optical pulse area  $\theta$ . The coherence term is represented by  $\varphi = \frac{i}{4} \sin \theta$ . The initialized density matrix  $\rho_I$  shows that there is a net population



difference of magnitude  $\xi$ , in the optically dark state  $|z-\rangle$ . This population difference in the spin subspace signifies a net spin polarization in the  $-\vec{z}$  direction and does in fact interact with the static magnetic field. The time evolution of the initialized system immediately after the initialization pulse at time  $\tau_0 = 0$  is then

$$\begin{aligned} \rho_{\mathbf{I}}(\tau_0) &= \mathbf{T}_{B_x}(\omega_L) \rho_{\mathbf{I}} \mathbf{T}_{B_x}^\dagger(\omega_L) \\ &= \begin{bmatrix} \frac{1}{2} - \xi \sin^2 \frac{\omega_L \tau_0}{2} & i \frac{\xi}{2} \sin \omega_L \tau_0 & -i \varphi \sin \frac{\omega_L \tau_0}{2} \\ -i \frac{\xi}{2} \sin \omega_L \tau_0 & \frac{1}{2} - \xi \cos^2 \frac{\omega_L \tau_0}{2} & \varphi \cos \frac{\omega_L \tau_0}{2} \\ i \varphi^* \sin \frac{\omega_L \tau_0}{2} & \varphi^* \cos \frac{\omega_L \tau_0}{2} & \xi \end{bmatrix}. \end{aligned} \quad (6.17)$$

The discussion so far has treated the optical excitations and precession dynamics in the magnetic field separately. The assumption is valid since the temporal pulse width (3 ps) is much shorter than the oscillation period of the quantum beats (83 ps). Therefore we can approximate the excitation to the trion state as instantaneous, so that precession around the magnetic field during the optical pulse duration is negligible.

For  $\tau_1 \gg \frac{1}{\Gamma_t} \sim 30$  ps, where  $\Gamma_t$  is the trion population decay rate, the trion state decays incoherently and equally into the two ground states, and  $\{\rho_{t+,t+}, \varphi\} \rightarrow 0$ . The decayed population only appears as a decaying background signal and does not affect the initialized coherence. This explanation is only appropriate when spontaneously generated coherence (SGC) [114] is negligible during the decay. This is true in the case of  $B_x = 6.6$  T. The density matrix after the decay at  $\tau_1$  can be written as a sum of two separate contributions from a completely mixed component ( $\rho_{\mathbf{I}+}^{mixed}$ ) and a completely pure component ( $\rho_{\mathbf{I}+}^{pure}$ ),

$$\begin{aligned} \rho_{\mathbf{I}}(\tau_1) &= \rho_{\mathbf{I}}^{mixed} + \rho_{\mathbf{I}}^{pure} \\ &= \frac{1-\xi}{2} \begin{bmatrix} 1 & 0 & 0 \\ 0 & 1 & 0 \\ 0 & 0 & 0 \end{bmatrix} + \xi \begin{bmatrix} \cos^2 \frac{\omega_L \tau_1}{2} & i \frac{1}{2} \sin \omega_L \tau_1 & 0 \\ -i \frac{1}{2} \sin \omega_L \tau_1 & \sin^2 \frac{\omega_L \tau_1}{2} & 0 \\ 0 & 0 & 0 \end{bmatrix} \end{aligned} \quad (6.18)$$

The pure component of the density matrix shows that the populations in the  $|z\pm\rangle$  states are oscillating at the Larmor frequency,  $\omega_L$ . The physical interpretation of the oscillations is obtained through calculating the expectation values of the three

spin components,  $\langle s_x \rangle$ ,  $\langle s_y \rangle$ , and  $\langle s_z \rangle$ , which correspond to the direction of the spin polarization. The initialized spin polarization with unit  $\frac{\hbar}{2}$  in Cartesian coordinates is then given by

$$\langle \vec{s}_I \rangle = \xi (0, -\sin \omega_L \tau_1, \cos \omega_L \tau_1) \quad (6.19)$$

representing the precession of the spin vector on the  $z - y$  plane around the magnetic field along the  $\hat{x}$  axis.

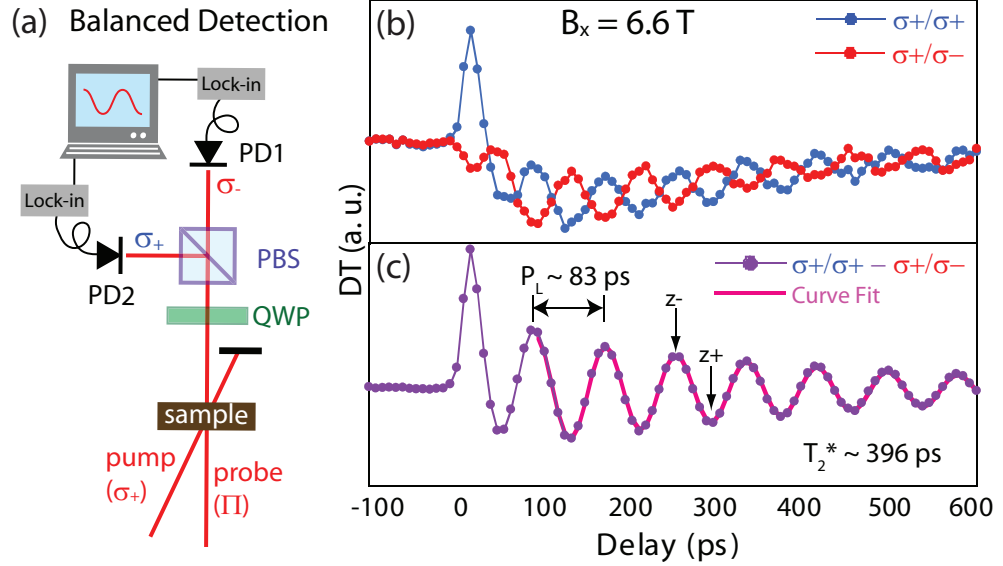


**Figure 6.4:** (a) Balanced detection setup for the initialization experiments.  $\Pi$  denotes linear polarization, QWP indicates a quarter wave plate, PBS is a polarization selective beam splitter and PD denotes photodiode. (b) and (c) Two-beam (pump and probe) quantum oscillation signals of the initialized spin polarization at  $B_x = 6.6$  T. (b) The blue (red) quantum beats signal is obtained using  $\sigma_+$  polarized pump pulses and  $\sigma_+$  ( $\sigma_-$ ) polarized probe pulses. (c) The difference of the two beat signals in (b), where the pink curve is a fit using a decaying Cosine function.

The spin precession is measured through the quantum oscillation of the DT signal in a two-beam pump and probe experiment. In the  $|z_{\pm}\rangle$  basis, the  $\sigma_+$  polarized pump creates the net spin polarization in the spin ground states by exciting population from the bright state,  $|z_+\rangle$ , to the trion. A probe pulse is then scanned in time to measure the initialization process and the subsequent spin polarization oscillations. The experimental setup is configured to excite and measure along the  $\hat{z}$  axis, and hence, all signals represent projections of the spin polarization along the  $\hat{z}$  axis.

Specifically, a  $\sigma_+$  polarized probe (co-polarized) measures the population in state  $|z+\rangle$  while a  $\sigma_-$  probe (cross-polarized) measures the population in state  $|z+\rangle$ . Since the changes of the population in states  $|z\pm\rangle$  are out of phase from each other, the beat signals from the corresponding probes are also out of phase. We can take advantage of this situation to enhance our beat signal and eliminate noise through a balanced detection technique shown in Figure 6.4(a).

The probe pulse is linearly polarized so that both co-polarized and cross-polarized signals are extracted simultaneously through a polarization beamsplitter cube. The co- and cross-polarized signals are each detected and processed using a set of photodiode and lock-in amplifier at each arm. The signals detected from both arms are presented as individual scans in Figure 6.4(b). Because these scans are taken simultaneously, they are subjected to the same common mode noise of the experimental setup, and only the signal is out of phase due to the intrinsic physics of the quantum system. Therefore, when the difference of these signals are taken in Figure 6.4(c), the resulting signal is twice as robust as the original and free of common mode noise. A decaying cosine function fit to the difference signal gives a spin dephasing time of  $T_2^* = 396$  ps limited by inhomogeneous broadening of the electron g-factor in the ensemble and spectral diffusion processes. The peaks and troughs of the beats represent net spin polarization pointing along the  $-\vec{z}$  (spin population in the  $|z-\rangle$  state) and  $+\vec{z}$  (spin population in the  $|z+\rangle$  state) directions, respectively. For the remainder of the chapter, all the the spin quantum beat data are presented as the difference signal between the co- and cross-polarized detection channels.

With one initialization pulse, the maximum initialized population is  $\frac{1}{2}$  via a  $\pi$  pulse excitation to the trion. With multiple initialization pulses configured in the right time sequence, more population of the spin can be initialized. The multiple pulsed initialization process has been reported theoretically [172] and demonstrated experimentally [117] using two pump pulses. The experimental result is shown in Figure 6.5, where the increase in the initialized population is evidence in the substantial increase of the oscillation amplitude. For  $n$   $\pi$  initialization pulses, the initialized population is  $1 - \frac{1}{2^n}$ , which approaches unity rapidly. Optical cooling of the spin

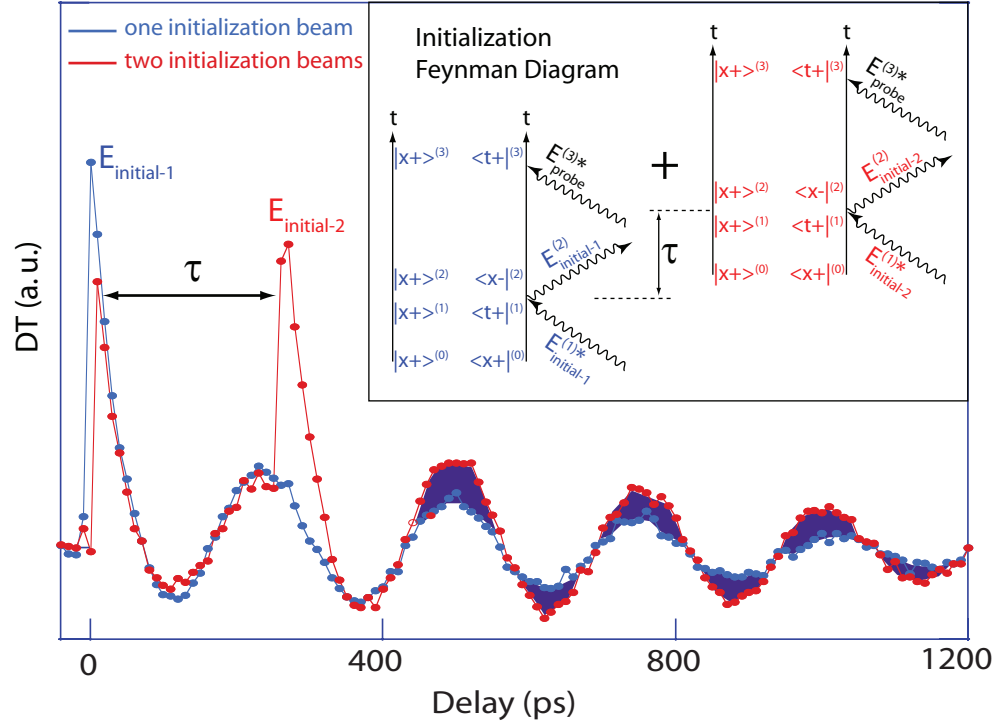


**Figure 6.5:** (Data courtesy of Dr. M. V. Gurudev Dutt [117]) Demonstration of two-pulse spin polarization initialization. The blue plot is the result of one initialization beam and the red plot is the result of two initialization beams. The shaded dark blue areas indicate the net gain in the initialized spin population when using two beams. The time delay between the two initialization pulses is  $\tau$ . The inset is a Feynman diagram of the two-pulse initialization process.

states using CW laser is also an option for spin initialization where the initialization rate depends on the decay mechanisms of the optical pumping states [122, 173].

The Feynman Diagram associated with the two-pulse initialization process is shown in the inset of Figure 6.5. It basically represents an interference of two independent paths. In the two-pulse initialization experiment, both initialization pulses are modulated at the same frequency. This detail on the modulation is crucial in distinguishing signals due to further initialization of the spin system from signals due to control of the initialized spin system (Subsection 6.2.2).

The creation of the spin coherence in the  $|x\pm\rangle$  basis by changing the relative populations in the  $|z\pm\rangle$  basis is yet another good demonstration of the interchangeability of population and coherence between different measurement bases discussed in Chapter 5. In the next subsection, we will further explore this relationship between the

different spin bases and its role in implementing ultrafast arbitrary spin rotations.

### 6.2.2 Coherent control of the initialized spin

The initialized spin polarization described by  $\rho_{\mathbf{I}}^{pure}$  in Subsection 6.2.1 can be controlled through an ultrafast optical pulse arriving after the initialization pulse with tunable delay ( $\tau_c$ ) and pulse area ( $\theta_c$ ). Analogous to arbitrary rotations in the three dimensional Cartesian coordinate, any arbitrary rotations in the spin subspace can be written as a combination of rotations around two fixed orthogonal axes. The two fixed orthogonal axes of rotation in the spin coherent control experiment are determined by the directions of the applied magnetic field ( $\vec{\mathbf{x}}$ ) and the effective magnetic field induced by the optical excitation ( $\vec{\mathbf{z}}$ ).

The general form of the pure spin state  $|\psi\rangle_{sp}$  in the  $|z\pm\rangle$  basis is

$$|\psi\rangle_{sp} = \sqrt{\xi} \left[ e^{i\phi} \cos \frac{\omega_L \tau}{2} |z+\rangle - i \sin \frac{\omega_L \tau}{2} |z-\rangle \right], \quad (6.20)$$

with amplitude of  $\sqrt{\xi}$ , where  $\xi$  is the initialized spin population, and  $\phi$  is the net phase between the dark and bright states  $|z\pm\rangle$  induced by the control pulse. Control of this spin state is accomplished through the manipulation of two variables. The first variable is the relative state probability amplitude, or population, between the two states  $|z\pm\rangle$ . The changes in this quantity is represented by the controlled rotations around  $\vec{\mathbf{x}}$ , the external magnetic field direction. The second variable is the relative phase,  $\phi$ , between the two states. This quantity is controlled by the rotations around  $\vec{\mathbf{z}}$  through a well-engineered optical pulse. By perfecting both rotations simultaneously, the spin state  $|\psi\rangle_{sp}$  can be rotated from any initial position to any final position covering the entire spin Hilbert space. For example, when  $\omega_L \tau = \frac{\pi}{2}$  and  $\phi = \mp \frac{\pi}{2}$ , the spin state  $|\psi\rangle_{sp}$  is proportional to  $|x\pm\rangle$  along the  $\hat{\mathbf{x}}$  axis. Similarly, a zero or  $\pi$  value of  $\phi$  puts the spin state in  $|y\pm\rangle$  along the  $\hat{\mathbf{y}}$  axis.

In the experiment, the population control aspect is automatically given in the presence of the  $B_x$  field. Because the initialized pure spin state is in  $|z-\rangle$ , which is not an eigenstate of the magnetic field,  $B_x$ , the initialized spin polarization precesses around the field. The demonstration of control is achieved through selective excita-

tions at different positions on the  $z - y$  plane during the precession of the net spin polarization. For a control pulse area of  $\theta_c = \pi$ , the optical pulse performs a Rabi rotation from state  $|z+\rangle$  to the trion state  $|t+\rangle$ . The rotation is followed by the trion decaying equally to the  $|x\pm\rangle$  states thus annihilating a portion of the spin coherence. The net result is a rotation together with a reduction of the magnitude of the spin vector. This is a partial rotation.

The density matrix after the  $\pi$  control rotation on the initialized spin from Subsection 6.2.1, and after the trion decays and redistributes in the spin ground states, is given by

$$\begin{aligned} \rho_c(\tau_c) &= \mathbf{T}_{B_x}(\omega_L) \mathbf{T}_{\sigma_+}(\pi) \rho_I^{pure}(\tau_1) \mathbf{T}_{\sigma_+}^\dagger(\pi) \mathbf{T}_{B_x}^\dagger(\omega_L) \\ &= \sin^2 \frac{\omega_L \tau_1}{2} \begin{bmatrix} \frac{1}{2} & 0 & 0 \\ 0 & \frac{1}{2} & 0 \\ 0 & 0 & 0 \end{bmatrix} + \cos^2 \frac{\omega_L \tau_c}{2} \begin{bmatrix} \cos^2 \frac{\omega_L t}{2} & i\frac{1}{2} \sin \omega_L t & 0 \\ -i\frac{1}{2} \sin \omega_L t & \sin^2 \frac{\omega_L t}{2} & 0 \\ 0 & 0 & 0 \end{bmatrix} \end{aligned} \quad (6.21)$$

where  $t$  starts at  $\tau_c$ . There are two terms as a result of the control optical pulse. The first term on the right hand side of Equation 6.21 is an incoherent term with amplitude  $\sin^2 \frac{\omega_L \tau_1}{2}$ , and the second term is a coherent term with amplitude  $\cos^2 \frac{\omega_L \tau_c}{2}$ . The amplitudes of both terms depends on the delay of the control pulse,  $\tau_c$ .

To explore the physics behind the control, we consider three particular values of  $\tau_c$  during the Larmor precession. When the control pulse arrives at  $\tau_c = \tau_{+z} = \frac{\pi}{\omega_L}$ , the entire initialized spin population  $\xi$  is in state  $|z+\rangle$  as shown in Figure 6.6(a). The  $\pi$  pulse excites all of  $\xi$  from the bright state  $|z+\rangle$  to the trion state  $|t+\rangle$ . After the decay of  $|t+\rangle$ , the system returns to the completely mixed state, as the excited population  $\xi$  redistributes equally and incoherently between the two spin ground states. As a result, the quantum beats are annihilated and the simulated signal exhibits a flat line following the control pulse at  $\tau_c = \tau_{+z}$  as shown in Figure 6.6(d).

By moving the control pulse to  $\tau_c = \tau_0 = \frac{3\pi}{2\omega_L}$ , where the optical signal or the  $\hat{z}$  component of the spin polarization is zero as shown in Figure 6.6(b), the spin polarization is along  $-\vec{y}$ , and states  $|z\pm\rangle$  have equal populations. The oscillation amplitude is decreased by half after the control pulse as expected in Figure 6.6(e), because half of  $\xi$  is being ‘‘protected’’ in the dark state  $|z-\rangle$  and is not destroyed by

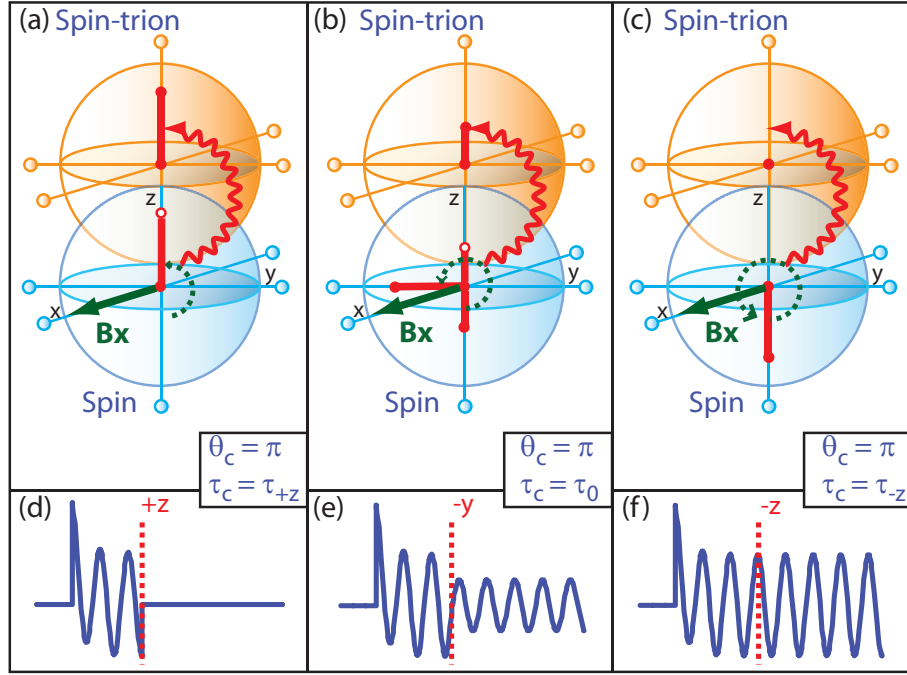


**Figure 6.6:** Evolution of the spin polarization vector at control pulse delay of (a)  $\tau_c = \tau_{+z}$ , (b)  $\tau_c = \tau_0$ , and (c)  $\tau_c = \tau_{-z}$ . The upper orange (lower blue) sphere is the trion-spin (spin) subspace. The red zig-zagged lines represent the  $\sigma_+$  polarized optical control field. The green solid arrows indicate the magnetic field directions and the green dotted curves are the paths of the precession of the spin polarization vector prior to the arrival of the control pulse. The red solid bars represent the spin polarization alignment. (d), (e) and (f) are simulated quantum oscillation signals before and after the control pulse at the different  $\tau_c$  indicated in (a), (b) and (c), respectively.

the decay and redistribution process.

Finally, when the spin polarization is along  $-\vec{z}$  at  $\tau_c = \tau_{-z} = \frac{2\pi}{\omega_L}$ , all of  $\xi$  is preserved in the optically dark state  $|z-\rangle$  as illustrated in Figure 6.6(c). The quantum beats are unaffected by the control pulse and continue to oscillate uninterrupted as pictured in Figure 6.6(f).

Overall then, as this delay  $\tau_c$  of the control optical pulse is scanned, the beat amplitude, which is also the magnitude of the spin polarization  $|\langle \vec{s}_{\tau_c} \rangle|$  from Eq. 6.19 after the control pulse at  $\tau_c$ , follows an oscillatory behavior

$$|\langle \vec{s}_{\tau_c} \rangle| = \frac{\xi}{2}(1 + \cos \omega_L \tau_c). \quad (6.22)$$

Experimentally, due to the unmodulated control beam, we need to consider the effect of the control on the uninitialized population ( $\rho_{I+}^{mixed}$  in Equation 6.19) in

addition to the initialized population ( $\rho_{I+}^{pure}$  in Equation 6.19). In the two-frequency modulation spectroscopy used, the DT signal detected at the difference modulation frequency is equivalent to the signal taken with the pump pulse on minus pump pulse off. When the pump beam is off, the  $\theta_c = \pi$  control pulse produces quantum beats with an amplitude of  $|\langle \vec{s}_{off} \rangle| = \frac{1}{2}$  from the completely mixed spin states, regardless of the control delay  $\tau_c$ . However, when the pump pulse is turned on, the position of the control delay  $\tau_c$  becomes significant. The beat amplitude after both the pump and control pulses consists of two terms, where the first is a  $\tau_c$  dependent controlled term,  $|\langle \vec{s}_{\tau_c} \rangle|$ , due to both the pump and control pulses as described in Equation 6.22, and the second term is a non-controlled term,  $|\langle \vec{s}_{mixed} \rangle| = \frac{1-\xi}{2}$ , due to the redistributed uninitialized spin population. The final amplitude of the normalized quantum beat signal detected after the control pulse, determined by the function  $I_{on-off}$  indicating pump pulse on minus off, is the sum of the controlled ( $|\langle \vec{s}_{\tau_c} \rangle|$ ) and non-controlled terms ( $|\langle \vec{s}_{mixed} \rangle|$ ) minus the  $|\langle \vec{s}_{off} \rangle|$  term,

$$I_{on-off}(\tau_c) = \frac{\xi}{2} \cos \omega_L \tau_c \quad (6.23)$$

Data of the three-beam control experiment are shown in Figure 6.7(a). The  $\cos \omega_L \tau_c$  dependence observed in the signal beat amplitudes after  $\tau_c$  (black solid line) in Figure 6.7(a) is in contrast with the  $1 + \cos \omega_L \tau_c$  dependence of the physical pictures in Figures 6.6(d),(e),and (f) as anticipated in Equation 6.23. For example, at  $\tau_c = \tau_{+z}$ , Figure 6.6(d) shows vanishing quantum beats after  $\tau_c$ , while the quantum beat signal corresponding to  $\tau_c = \tau_{+z}$  in Figure 6.7(a) persists due to the non-zero  $I_{on-off}$ . Numerical simulations in Figure 6.7(b) take into account the experimental parameters, such as the pulse width, beam modulations, and decoherence times of the system. The theoretical results are in excellent agreement with the experiment. An uninterrupted mathematical recap of the entire spin control process of initialization, control and measurement is covered in Appendix C.

We note that unlike the work in Ref. [117], where the observed signal is a result of the quantum interference between two independently initialized spin coherences induced by the two pump pulses, the behavior described here is due to the subsequent



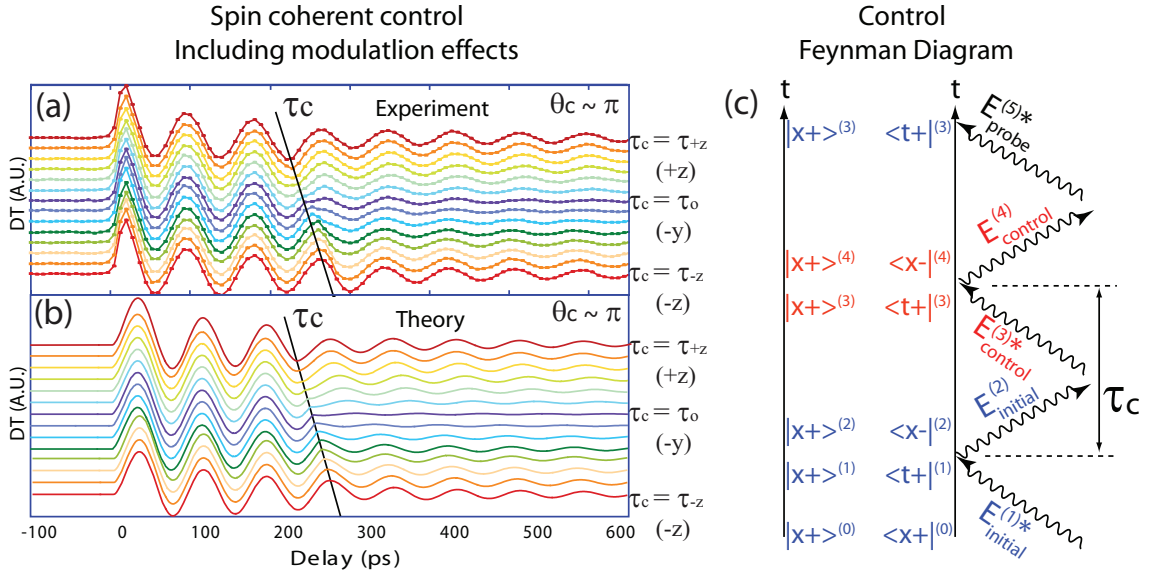


**Figure 6.7:** (a) Experimental result of the three-beam (initialization, control and probe) quantum oscillation signal at different control delay  $\tau_c$  and control pulse area  $\theta_c \sim \pi$ . The black solid line indicates the position of the control pulse. (b) Theoretical simulations of the same experimental set up in (a) (Courtesy of our Collaborator, Dr. Sophia Economou). (c) Feynman diagram of the spin control experiment.

rotation by the control pulse of the initially pump-induced spin coherence. The Feynman diagram for the control sequence is a single continuous path, shown in Figure 6.7(c) as opposed to the sum of two paths as shown in the inset of Figure 6.5. By comparing the two diagrams, it is clear that controlling and rotating the spin is a higher order process than the multiple pulsed initialization of the spin. In terms of optical pulses as transformation matrices for the state vector of the quantum system, the former is a sum of two matrices while the latter is a product.

To completely control the rotations of the electron spin in the spin subspace without populating the trion, we need to use a “transitionless”  $\theta_c = 2\pi$  pulse to control the relative phase  $\phi$  between states  $|z\pm\rangle$  in addition to the populations. This phase control is responsible for the rotation around the  $\vec{z}$  axis. In the presence of this control pulse, the population in the bright state  $|z+\rangle$  is unaffected, but the state acquires an overall phase depending on the detuning of the pulse from the trion state [171]. For example, the overall phase gained for an on resonance  $2\pi$  control

pulse is  $\phi = \pi$ . At  $\tau_c = \tau_0$ , the spin state is rotated from  $|y-\rangle$  to  $|y+\rangle$ , representing a spin flip. Similarly,  $\phi = \frac{\pi}{2}$  rotates the spin state from  $|y-\rangle$  to  $|x+\rangle$ . The detail of the net phase gained relies on the specific pulse shape used. For a secant-hyperbolic pulse ( $\chi(t) = \chi_0 \text{sech}(\Omega t)$ ) used in the experiment, our collaborator in Reference [171] provide a detail derivation of the expression of  $\phi$  given by

$$\phi = 2 \arctan \frac{\Omega}{\delta}, \quad (6.24)$$

where  $\Omega$  is the bandwidth of the pulse, and  $\delta$  is the detuning from the trion state. In addition, the “transitionless” condition is met by requiring  $\chi_0 = \Omega$ , which indeed translates to a  $2\pi$  pulse for the Sech pulse.

The  $2\pi$  rotation on the  $|z+\rangle$  state via the trion required for the phase control are not observed in the interface fluctuation QDs studied. Possible reasons for this difficulty could be the weak confinement potentials and the charged nature of these dots, which allow for interactions between the supposedly closed spin-trion  $\Lambda$  system and its semiconductor environment. The exact nature of the interactions is not fully understood, especially in light of the fact that Rabi oscillations in neutral interface fluctuation QDs have been observed [76]. Nevertheless, the demonstration of Rabi oscillations in a trion ensemble [108] and, more profoundly, in a single trions (recent result obtained in our laboratory) in the self-assembled QD shows that the result in this experiment should be readily applicable in those structures.

Technically, the magnetically induced Larmor precession about  $\vec{x}$  and optically induced rotation about  $\vec{z}$  are sufficient for creating any arbitrary spin state. For an all-optical ultrafast spin rotation scheme desired by quantum information processing, optically induced rotation around  $\vec{x}$  [174] can replace the Larmor precession.

### 6.3 Chapter summary

In summary, we have demonstrated ultrafast spin manipulation utilizing the upper trion state. Although a complete spin rotation is not observed in the interface fluctuation charged QD, this work lays the foundation for ultrafast arbitrary spin rotations in self-assembled QDs, which have much stronger confinement. The potential

of these dots is explored further in the next chapter.

## CHAPTER 7

### Summary and Future Directions

The experimental research described in this thesis is part of an ongoing effort striving for the ultimate realization of a physical quantum computing device in a semiconductor quantum dot (QD) system. The attraction of the QD system lies not merely in its atomic-like discrete states, but more valuably in the flexibility with which the optical properties of these states can be engineered. The energy range of the QD states can be manipulated through bandgap engineering, which allows the QD system to take advantage of a wide range of laser sources available as opposed to being restricted to only atomic transition wavelengths. In addition to the freedom in energy selection, the polarization of optical transitions can also be manipulated. Because spherical symmetry in a QD is not an intrinsic property, parity is not conserved. Utilizing this property, the polarization selection rule of an optical transition can be engineered to deviate from the atomic rules by changing the amount of strain in a dot and the asymmetry of the dot shape. In fact, it was the nonconventional polarizations that led to the observation of spontaneously generated coherence (SGC) [114] in a QD  $\Lambda$  system. The fact that the semiconductor QD is an artificially fabricated structure means that many aspects of the QD can be engineered. In addition to being able to control the energies and polarizations of the optical transitions in a QD, we can also influence the optical dipole moment and the effective carrier g-factors in a dot [175].

The level of flexibility and control in engineering a dot according to specification is evident in the progression of dot samples used in experiments. In the prototypical GaAs interface fluctuation QDs, the large optical dipole was extremely convenient

for the preliminary studies of the optical properties of the dot relevant to quantum computation. In this type of dot, a set of universal quantum gates were accomplished using exciton-based qubits [76, 104]. This thesis extended the demonstration by showing the dot's ability to propagate coherent information and the tomographic construction of a single qubit density matrix in Chapters 4 and 5. The fast 100 ps decoherence time of the exciton-based qubit is impractical for the purpose of quantum computation, which encouraged the adaptation of a spin-based qubit possessing a long decoherence time of at least 100  $\mu$ s. The doped GaAs interface fluctuation QD (IFQD) sample fabricated for the initial study of a single spin in a QD maintained the advantage of the large optical dipole and while introducing single electrons to the neutral dot. The combination produced an excellent medium for understanding the optical and spin properties in a single QD, which aided the speedy formulation of an optical manipulation scheme for a single spin trapped inside a dot discussed in Chapter 6.

Owing to the weak confinement potential of interface fluctuation dots, stability of the electron in the dot is greatly diminished due to tunnelling. The new species of dot is the InAs self-assembled QD (SAQD), modified to address this issue with a stronger confinement and a controllable charging mechanism for the dots via the Schottky diode configuration. One slightly inconvenient consequence of a stronger confinement is the smaller optical dipole moment, and hence, weaker optical signal, which leads to difficulties in detection using the differential transmission (DT) technique presented in Chapter 3.

The next section (Section 7.1) introduces a novel voltage modulation technique for detecting the optical signal from a single InAs dot and some initial characterization results of the dot. Subsection 7.2.1 will highlight a few ground breaking results currently being produced on these dots in our laboratory in both frequency and time domain studies. The results and knowledge gained in the older generations of dot samples formed the foundation necessary for performing coherent single spin rotations in the newer InAs QD samples. The future initiative on an entangled scalable system is being pursued with InAs double-dot molecules by our collaborators

at the Naval Research Laboratory (NRL). Their highly promising work is summarized in Subsection 7.2.2.

### 7.1 Voltage dependent PL and modulated absorption of a single InAs dot

The sample structure and general optical properties of the InAs SAQDs are discussed in Section 2.4 of Chapter 2 and will not be reiterated here. The Schottky diode structure on the surface of the sample is employed to change the electric field across the semiconductor along the growth direction. The DC Stark shift induced by this electric field tunes the internal energy levels of the dot with respect to the Fermi energy of the electron sea in the doped layer. When the dot energy is above the Fermi energy, the dot is neutral, and excitons ( $X^0$ ) dominate in the optical transitions. As the dot energy is tuned closer and closer to the Fermi level, the electrons can begin to tunnel into the dots. The right voltage will charge the dot with exactly one electron, and the optical excitations will generate negatively singly charged excitons (negative trions,  $X^-$ ). The Schottky voltage can be continuously tuned to produced more and more exotic quasi-particles in the dot, such as the positive trion ( $X^+$ ), doubly charged excitons ( $X^{\pm 2}$ ), etc. Our ultimate interest rests in the negative trion, which is the intermediate state for optically coupling the two spin ground states for the purpose of manipulating the single spin qubit.

The primary method used for the initial characterization of the sample is a voltage dependent photoluminescence (PL) mapping of the voltage ranges of different quasi-particles in the InAs dots. The PL map shown in Figure 7.1(a) is from aperture A6(7) of sample R041230F taken using a pump laser at 780 nm. The PL map was constructed by combining many individual PL spectra taken at different fixed Schottky voltages within the range of -1.5 V to 0.5 V. One instance of such a PL spectrum at -1 V is shown in Figure 7.1(b). In this PL map, we can clearly identify the exciton and negative trion transitions separated by a binding energy of approximately 5 meV. The PL map is an excellent tool for identifying different energy states

in a single dot and the respective voltage range in which they occur. However, the PL technique is a non-resonant excitation process, and it does not necessarily reflect the same spectrum as an on-resonance excitation process, such as absorption. In order to probe the on-resonant optical properties of the trion state, which mainly appears in the range of -1.25 V and -1 V, we need to resonantly excite the state.

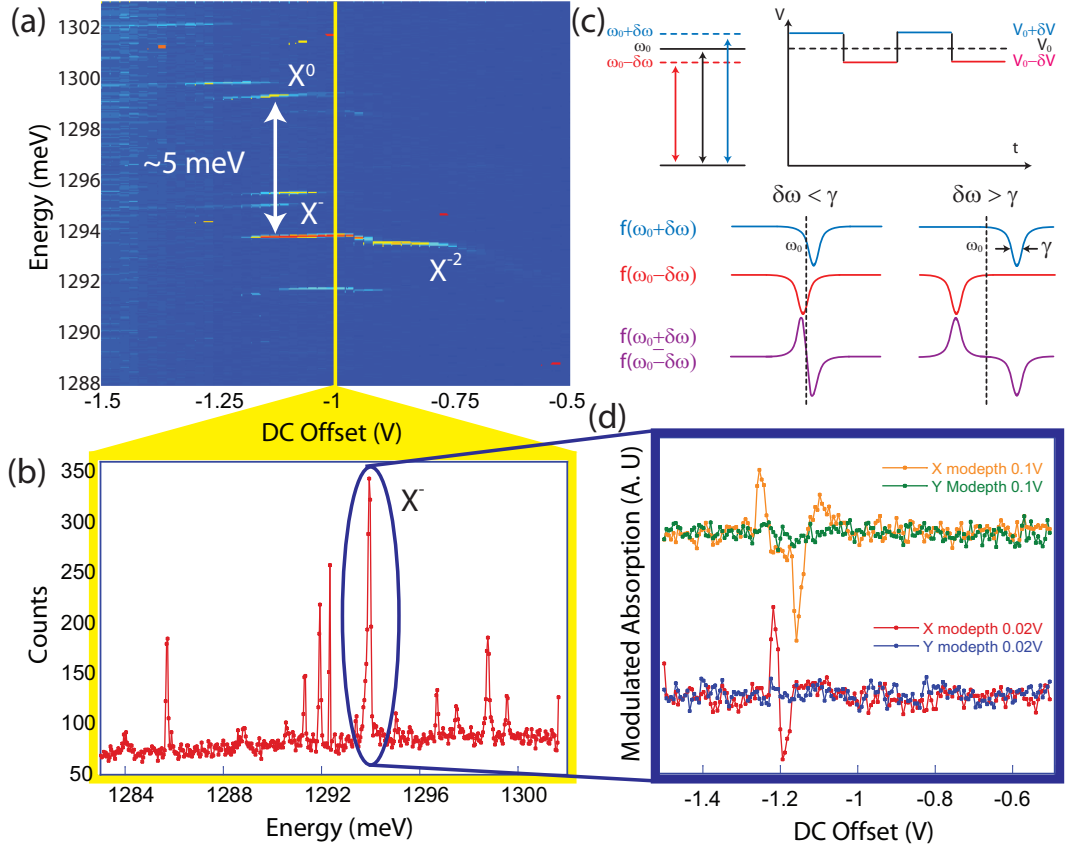


**Figure 7.1:** Voltage dependent PL map and absorption of a single InAs SAQD from sample R041230F, aperture A6(7). (a)  $X^0$  represents the neutral exciton,  $X^-$  is the negative trion, and  $X^{-2}$  is the doubly negative exciton. The 5 meV difference is the binding energy between the exciton and its respective trion, where the trion is the line at lower energy. (b) Cross-section of the PL map taken at -1 V. (c) Pictorial depiction of the voltage modulation absorption scheme.  $\delta\omega$  is the Stark shift amount,  $2\delta V$  is the modulation depth, and  $\gamma$  is the intrinsic linewidth of the state. (d) The two voltage modulation absorption scans are taken at different modulation depths of 0.1 V and 0.02 V. X and Y are the two channels of the lock-in amplifier.

The small optical dipole of the InAs SAQDs previously mentioned considerably decreases the strength of the third order signal predominantly detected by the on-

resonance DT technique used in previous experiments on the GaAs IFQDs. The average dipole moment of the GaAs dots is around 100 D while the average dipole for the InAs dots is 5 times smaller at approximately 20 D. The measured third order DT signal is proportional to  $\mu^4$  (see Chapter 3 for derivation), which means that the same DT signal in InAs dot would be roughly 625 times smaller. Of course, this is a very crude estimation. Nevertheless, the effect of the small optical dipole was hindering the data taking process because the third order optical signal was too weak to be observed. A new resonance manipulation and detection technique is required to circumvent the problem of small optical signal.

The novel technique of voltage modulated absorption that enables the observation of the pure absorption signal was inspired by the Schottky voltage induced DC Stark shift. After the general energy range of the optical transition of the trion is obtained from the PL map, the frequency of a CW laser is tuned to the trion energy at the middle of the voltage range. To extract only the absorption signal from the exciting CW laser, we applied a square modulation to the DC Schottky voltage with a small modulation depth ( $2\delta V$ ). The voltage modulation periodically shifts the energy of the trion state by an amount  $\pm\delta\omega$  with respect to the fixed laser frequency ( $\omega_0$ ) as shown in Figure 7.1(c). As the DC offset portion of the voltage is being scanned, the lock-in amplifier detects the absorption signal at the modulation frequency. Examples of such voltage modulation absorption spectra are shown on Figure 7.1(d) with two modulation depth values. For the bottom spectrum, the modulation depth voltage of 0.02 V induced a DC Stark shift smaller than the linewidth ( $\gamma$ ) of the trion state, resulting in a differential lineshape of the actual absorption profile. As we increase the modulation depth voltage to 0.1 V for the top spectrum, the induced DC Stark shift is larger than the linewidth of the trion state and two out-of-phase peaks are observed with each peak representing the actual absorption profile.

The voltage dependent PL map and the voltage modulation absorption method is part of a set of routine characterization measurements for finding suitable states for further investigation of their magnetic field dependence, transient quantum coherence, and high optical power properties.



## 7.2 Future directions in InAs self-assembled quantum dots

Since voltage modulation is a single beam experiment and does not rely on optical modulation of the excitation field, the absorption signal obtained is to all orders of the optical field and is much stronger than the third order signal from the DT detection technique. Using this simple yet hugely efficient method, we were able to observe in the frequency domain (CW lasers) spin initialization through optical pumping [122] and the first complex absorptive Mollow spectrum in a single quantum dot [82]. At the same time, through careful and relentless experimental efforts, the elusive time domain (pulsed laser) single dot trion signal was also attained and confirmed. This breakthrough sets a milestone in the course of progress towards ultrafast single spin qubit manipulation.

### 7.2.1 CW and transient efforts on single dots

The atomic qualities of the quantum dot have once again been beautifully demonstrated in a set of high field CW experiments on a single exciton state. The strong confinement of the InAs dot provides excellent isolation of the dot states from the effects of delocalized scattering states. The exciton and trion systems in such isolation remain truly closed systems. Under high optical field excitations, the states involved are dressed by the quantized optical fields. In the three-level exciton  $V$  system, a pair of cross-polarized strong pump and weak probe beams were used to detect the famous Autler-Townes doublet in the absorption spectrum. When the pump and probe are co-polarized and exciting the same two-level exciton system, an interesting phenomenon appears in the form of a complex absorption Mollow spectrum as a result of a combination of the optically dressed states and energy transfer between the two beams. This impressive work is described in detail in Reference [82]. Similar features were also observed for the trion state.

Another important accomplishment towards quantum computation is the near unity initialization of the spin-based qubit states via optical pumping through the trion state [122]. When the Voigt geometry magnetic field is turned on, the spin state

is mixed as shown in Figure 2.10(b) in Chapter 2. By tuning the CW laser to the  $V1$  transition, the spin population in state  $|x+\rangle$  is transferred to the trion state and decays with equal probability to both spin states. Since the pumping is only on the  $V1$  transition, the all the spin population in spin state  $|x+\rangle$  will eventually be pumped into the  $|x-\rangle$  state, hence initializing the spin. The reverse pumping direction is equally achievable by tuning the CW laser to the  $V2$  transition. The initialized spin would then be in the  $|x+\rangle$  state. The pumping rate is ultimately limited by the decay rate of the trion state to approximately 1 Ghz. The pumping rate in the Voigt configuration is  $10^3$  orders larger than that in the Faraday configuration where the spin states are not mixed and the rate is limited by the hole spin flip [176]. The final initialization is 99% corresponding to a spin temperature of 0.06 K.

Concurrently, for transient measurements using ultrafast optical pulses, the voltage modulation absorption technique was modified to obtain the absorption signal. Since the time domain pulse has a large bandwidth, the small modulation depth used in CW experiments is no longer useful in extracting the absorption signal. Instead, a large modulation depth is used to switch between voltage values in and out of the range of the trion. Using this method, the population decay time of the trion in zero magnetic field was measured to be around 800 ps and Rabi oscillations of a single trion were confirmed with an extracted dipole moment of approximately 8 D. Furthermore, in the presence of the Voigt magnetic field, preliminary results of single spin quantum beats were also detected with beat frequencies matching the respective electron and hole splittings obtained at equal field in the CW absorption spectra.

The future goal of single spin manipulation (spin Rabi rotation) requires the joint efforts of both frequency and time domains. Advancing from the successes of the exciton and trion Mollow spectra, a frequency domain experiment is underway to obtain the spin Mollow spectrum from which the spin Rabi frequency can be extracted. Meanwhile, pulse excitation will be combined with CW initialization and detection to demonstrate arbitrary rotations of a completely initialized spin qubit.

### 7.2.2 InAs double-dot molecules

While the dynamics and control in a single InAs dot are under intense investigation in our laboratory, our collaborators at NRL are devoting a vast amount of attention to the construction and study of double-QD molecules [118,177]. Their current efforts involve understanding and deciphering the complex optical features in the voltage dependent PL map of a single QD molecule. The presence of anti-crossing is highly suggestive of forms of inter-dot coupling. This is an extremely exciting development for the prospect of multi-qubit entanglement and a scalable quantum computing system.

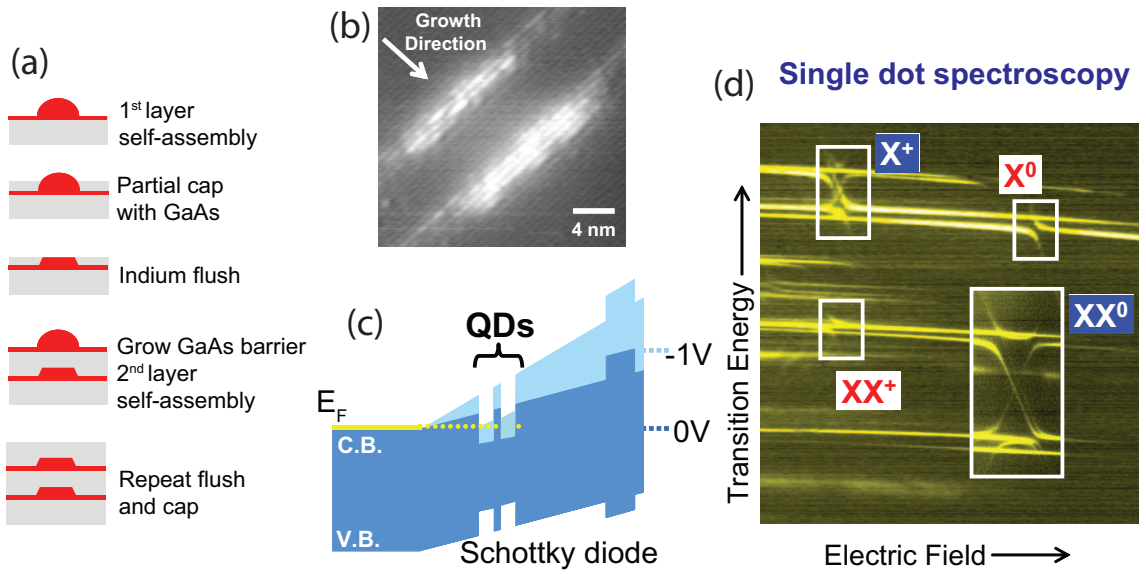


**Figure 7.2:** InAs double dot molecule growth, structures, and voltage dependent PL map. (a) The double dots growth procedure. (b) Scanning tunnelling microscope (STM) image of the vertically stacked double dots. (c) Charging scheme of the dot. (d) Voltage dependent PL map of the double dots, where  $X^0$  ( $X^+$ ) denotes the neutral (positive trion) exciton and  $XX^0$  denotes the neutral biexciton (positively charged biexciton). Images in (b) and (d) are taken from Reference [118], courtesy of Dr. Dan Gammon from the Naval Research Laboratory (NRL).

The InAs QD molecules are grown with a similar method as the single InAs dots discussed in Section 2.4 of Chapter 2 and shown in Figure 7.2(a). The second layer of dots has a nearly perfect vertical alignment with the first layer due to the effects of the strain induced by the first layer of dots on the diffusion and nucleation of the second layer dots [178,179]. The energy separation between the two dots in the dot molecule

can be controlled by manipulating the relative height of each dot. Additionally, the coupling strength between the dots is regulated by the GaAs barrier between the dots. An example of a double-dot molecule is shown in the scanning tunnelling microscope image in Figure 7.2(b), where the dot size and the separation between the dots can be clearly measured.

Schematically, as shown in Figure 7.2(c), the charging of the double-dot molecule is no different from the single dot. However, the resulting states in the double-dot molecule are not only more complicated, but are also much more intriguing. The voltage dependent PL map of a double-dot molecule can be seen in Figure 7.2(d). The crisscrossed patterns in the PL map are results of the coupling between the dots. The horizontal lines are the intra-dot transitions within a single dot as the DC stark shift induced by the Schottky voltage is small compared to the energy scale of the PL map. The diagonal lines can be attributed to the inter-dot transitions which have a large voltage dependence. As the voltage tunes the energy of the inter-dot transition to approximately that of the intra-dot transition, tunnelling of carriers between the dots gives rise to the anti-crossing features seen in Figure 7.2(d). The crisscrossed patterns occur when both the ground and excited states involved in the transitions contain anti-crossing features, such as the transitions of trions ( $X^\pm$ ). The details and physics behind the labelling of these complicated transition lines can be found in References [118, 177]. Further studies of the double-dot molecules also demonstrated the capability of engineering the carrier g-factor [175] and led to further understanding of the spin fine structures in the presence of inter-dot coupling [180].

### 7.3 Summary

Although there are still many obstacles on the path to achieving a true physical realization of a practical quantum computer, what has been accomplished is still undeniably valuable not only to the field of quantum computation but also to the further understanding of the incredible structure of the semiconductor quantum dot. As we progress forward towards the optically manipulated double-dot molecular sys-

tem, we are optimistic that quantum information processing is a tangible reality in the foreseeable future.

## APPENDICES

## APPENDIX A

### Interferometer stabilization circuits

In order to achieve optical phase stability for experiments in Chapters 4 and 5, the Michelson interferometer must be stabilized to within fm. The stabilization circuits for the Michelson interferometer shown on Figure A.1 is designed for such task.

The reference signal is provided by a green helium neon (HeNe) laser following the same path of the laser beam from the 702X dye laser. The interference signal from the green HeNe is detected on a photodiode (PD) and the current is changed into a voltage source for the feedback circuit. This voltage signal is compared to an adjustable precision voltage reference source provided by an operational amplifier (Op-Amp). The difference of the PD voltage and the reference is outputted as an error voltage,  $V_{err}$ , to the input of the summing circuit. The summing circuit combines  $V_{err}$  with a constant background voltage provided by the Lock-in amplifier's auxiliary output. The sum of these two voltages are amplified to provide the driving voltage for the piezoelectric mirror mount (PZT) and completing the feedback loop.

The integration time, feedback speed, of the circuit can be adjusted by choosing the desired capacitor in the feedback circuit. Although a fast integration time is normally desired for faster error correcting rate, we must keep in mind the load on the PZT and its natural resonate frequency and choose a compromising time for the circuit.

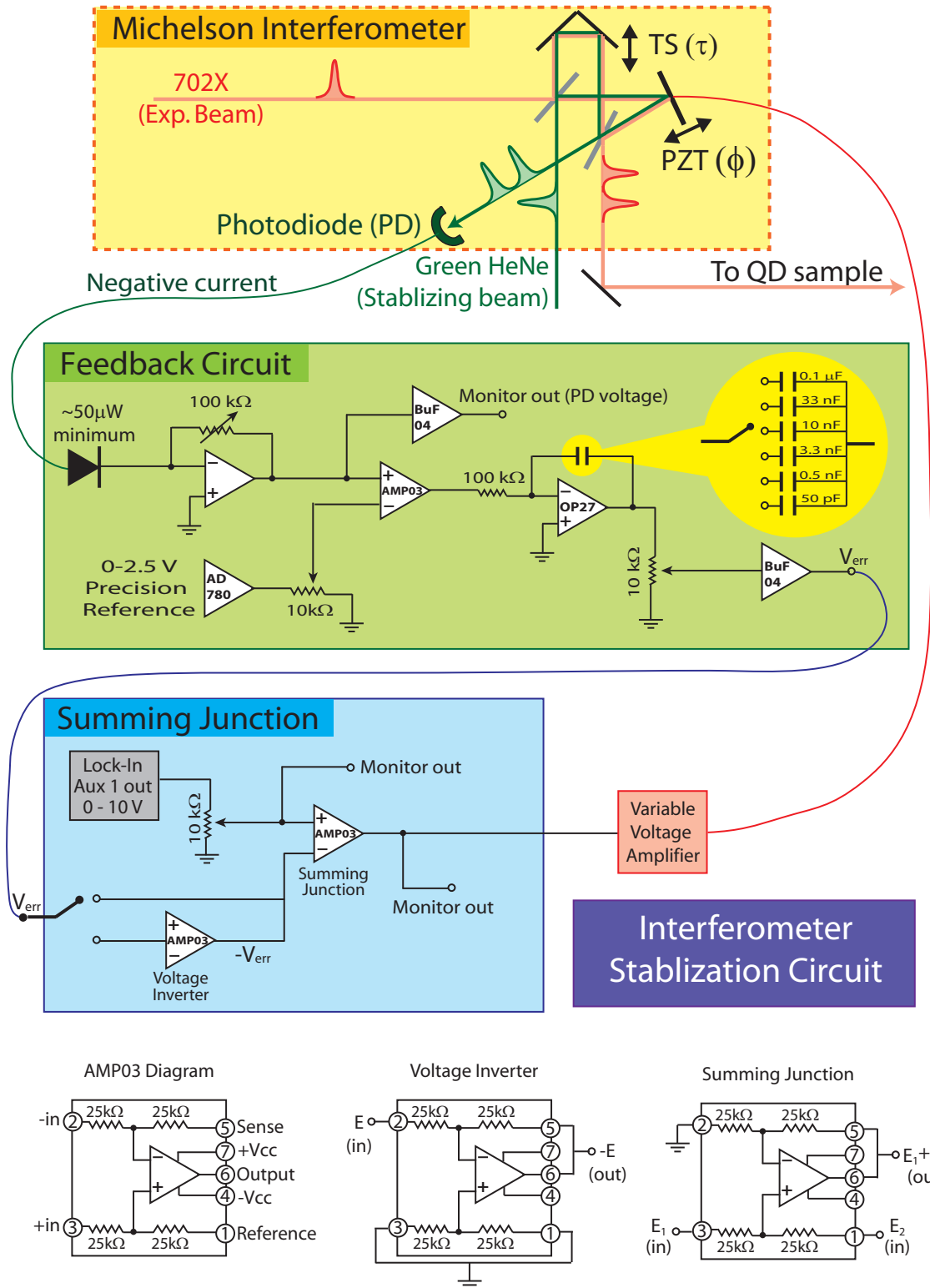


**Figure A.1:** Stabilization scheme for the Michelson interferometer in the coherent control and density matrix tomography experiments in Chapters 4 and 5. The triangular symbols represent operational amplifiers. PZT is the piezoelectric mirror mount and TS is the coarse micro-translation stage. HeNe stands for helium neon.



## APPENDIX B

### Derivation of square pulse solution in three-level $\Lambda$ system

For the three-level  $\Lambda$  system presented in Figure 6.1 of Chapter 6, the rewritten equations of motion (Equation 6.2) under a square pulse excitation are

$$\begin{aligned}\dot{c}_+(t) &= -i \left[ \sqrt{2}\chi c_2(t) + \frac{\omega_{13}}{2} c_-(t) \right] \\ \dot{c}_2(t) &= -i\sqrt{2}\chi c_+(t) \\ \dot{c}_-(t) &= -i\frac{\omega_{13}}{2} c_+(t),\end{aligned}\tag{B.1}$$

where  $\chi = -\frac{\boldsymbol{\mu}_2 \cdot \mathbf{E}}{2\hbar}$  with a constant field,  $\mathbf{E}$ . The dipole moment is  $\boldsymbol{\mu}_2$ , and  $\omega_{13}$  is the frequency difference between state  $|1\rangle$  and  $|3\rangle$ . The probability amplitudes  $c_{\pm}(t) = [c_1(t) \pm c_3(t)]/\sqrt{2}$  correspond to states of  $|\pm\rangle = (|1\rangle \pm |3\rangle)/\sqrt{2}$ .

Since  $c_2(t)$  and  $c_-(t)$  only depends on  $c_+(t)$  and not on each other, we can isolate and solve for  $c_+(t)$ . By taking a derivative of  $\dot{c}_+(t)$  and substituting values of  $\dot{c}_2(t)$  and  $\dot{c}_-(t)$ , we get a second order differential equation of  $c_+(t)$ ,

$$\ddot{c}_+(t) + \Omega^2 c_+(t) = 0,\tag{B.2}$$

where  $\Omega = \sqrt{2\chi^2 + \frac{\omega_{13}^2}{4}}$ . The general solution to Equation B.2 is then

$$c_+(t) = A \cos \Omega t + B \sin \Omega t.\tag{B.3}$$

Consequently, we can solve for  $c_2(t)$  and  $c_-(t)$  by substituting the solution of  $c_+(t)$  into the first order differential equations and obtain,

$$\begin{aligned}c_2(t) &= -i\frac{\sqrt{2}\chi}{\Omega} (A \sin \Omega t - B \cos \Omega t) + \alpha \\ c_-(t) &= -i\frac{\omega_{13}}{2\Omega} (A \sin \Omega t - B \cos \Omega t) + \beta.\end{aligned}\tag{B.4}$$

The next step is to calculate the four unknown constants ( $A$ ,  $B$ ,  $\alpha$  and  $\beta$ ) in terms of the initial values of the system at  $t = 0$ . At  $t = 0$ , we have four equations for four unknowns,

$$\begin{aligned} c_+(0) &= A \\ c_2(0) &= i\frac{\sqrt{2}\chi}{\Omega}B + \alpha \\ c_-(0) &= i\frac{\omega_{13}}{2\Omega}B + \beta \\ \dot{c}_+(0) &= \Omega B = -i\frac{\omega_{13}}{2}c_-(0) - i\sqrt{2}\chi c_2(0). \end{aligned} \quad (\text{B.5})$$

After some simple algebra, the solutions of the constants are

$$\begin{aligned} A &= c_+(0) \\ B &= -i\frac{\omega_{13}}{2\Omega}c_-(0) - i\frac{\sqrt{2}\chi}{\Omega}c_2(0) \\ \alpha &= \frac{\omega_{13}^2}{4\Omega^2}c_2(0) - \frac{\chi\omega_{13}}{\sqrt{2}\Omega^2}c_-(0) \\ \beta &= \frac{2\chi^2}{\Omega^2}c_-(0) - \frac{\chi\omega_{13}}{\sqrt{2}\Omega^2}c_2(0). \end{aligned} \quad (\text{B.6})$$

The final form of the solutions to the equations of motion in terms of the initial values are

$$\begin{aligned} c_+(t) &= \cos \Omega t c_+(0) - i\frac{\omega_{13}}{2\Omega} \sin \Omega t c_-(0) - i\frac{\sqrt{2}\chi}{\Omega} \sin \Omega t c_2(0) \\ c_2(t) &= -i\frac{\sqrt{2}\chi}{\Omega} \sin \Omega t c_+(0) - \frac{\sqrt{2}\chi\omega_{13}}{\Omega^2} \sin^2 \frac{\Omega t}{2} c_-(0) + \left[ \frac{\omega_{13}^2}{4\Omega^2} + \frac{2\chi^2}{\Omega^2} \cos \Omega t \right] c_2(0) \\ c_-(t) &= -i\frac{\omega_{13}}{2\Omega} \sin \Omega t c_+(0) + \left[ \frac{2\chi^2}{\Omega^2} + \frac{\omega_{13}^2}{4\Omega^2} \cos \Omega t \right] c_-(0) - \frac{\sqrt{2}\chi\omega_{13}}{\Omega^2} \sin^2 \frac{\Omega t}{2} c_2(0). \end{aligned} \quad (\text{B.7})$$

In the original basis of  $|1\rangle$  and  $|3\rangle$ , the solutions are

$$\begin{aligned} c_1(t) &= \left[ \left( \frac{1}{2} + \frac{\omega_{13}^2}{8\Omega^2} \right) \cos \Omega t - i\frac{\omega_{13}}{2\Omega} \sin \Omega t + \frac{\chi^2}{\Omega^2} \right] c_1(0) - \frac{2\chi^2}{\Omega^2} \sin^2 \frac{\Omega t}{2} c_3(0) \\ &\quad - \left[ i\frac{\chi}{\Omega} \sin \Omega t + \frac{\chi\omega_{13}}{\Omega} \sin^2 \frac{\Omega t}{2} \right] c_2(0) \\ c_2(t) &= -i\frac{\chi}{\Omega} \sin \Omega t [c_1(0) + c_3(0)] - \frac{\chi\omega_{13}}{\Omega^2} \sin^2 \frac{\Omega t}{2} [c_1(0) - c_3(0)] + \left[ \frac{\omega_{13}^2}{4\Omega^2} + \frac{2\chi^2}{\Omega^2} \cos \Omega t \right] c_2(0) \\ c_3(t) &= \left[ \left( \frac{1}{2} + \frac{\omega_{13}^2}{8\Omega^2} \right) \cos \Omega t + i\frac{\omega_{13}}{2\Omega} \sin \Omega t + \frac{\chi^2}{\Omega^2} \right] c_3(0) - \frac{2\chi^2}{\Omega^2} \sin^2 \frac{\Omega t}{2} c_1(0) \\ &\quad - \left[ i\frac{\chi}{\Omega} \sin \Omega t - \frac{\chi\omega_{13}}{\Omega} \sin^2 \frac{\Omega t}{2} \right] c_2(0). \end{aligned} \quad (\text{B.8})$$

## APPENDIX C

### Complete process of the spin coherent control

#### I. Relationship between the $x$ and $z$ bases of the spin states

The relationship between the  $\mathbf{x}$  and  $\mathbf{z}$  bases are given by the followed equations,

$$|z+\rangle = \frac{|x+\rangle + |x-\rangle}{\sqrt{2}}, \quad |z-\rangle = \frac{|x+\rangle - |x-\rangle}{\sqrt{2}}. \quad (\text{C.1})$$

In the form of the density matrices elements, the two bases are related as followed,

$$\rho_{z+z+} = \frac{1}{2}(\rho_{x+x+} + \rho_{x-x-} + \rho_{x+x-} + \rho_{x-x+}) \quad (\text{C.2})$$

$$\rho_{z-z-} = \frac{1}{2}(\rho_{x+x+} + \rho_{x-x-} - \rho_{x+x-} - \rho_{x-x+}) \quad (\text{C.3})$$

$$\rho_{z+z-} = \frac{1}{2}(\rho_{x+x+} - \rho_{x-x-} - \rho_{x+x-} + \rho_{x-x+}). \quad (\text{C.4})$$

To change from the  $\mathbf{x}$  basis back to the  $\mathbf{z}$  basis, we simply need to swap the notations  $\mathbf{x}$  and  $\mathbf{z}$  in the above equations.

In the Voigt geometry magnetic field along the  $\hat{\mathbf{x}}$  direction, the electron spin is quantized along the magnetic field in the  $\hat{\mathbf{x}}$  direction. The spin Zeeman splitting energy is much smaller than the thermal excitation energy as indicated in the main text of Chapter 6, which results in a nearly completely mixed initial state in both  $\mathbf{x}$  and  $\mathbf{z}$  bases,

$$\rho_o^{(z)} = \rho_o^{(x)} = \begin{bmatrix} \frac{1}{2} & 0 & 0 \\ 0 & \frac{1}{2} & 0 \\ 0 & 0 & 0 \end{bmatrix} \quad (\text{C.5})$$

## II. Evolution of the spin system through the pulse sequence

The following calculations are all done in the  $\mathbf{z}$  basis in the density matrix picture. We use one polarization of light ( $\sigma_+$ ) to excite the system, which means it only couples the  $|z+\rangle$  state to the  $|t+\rangle$  trion state. The spontaneous generated coherence (SGC) is not included in the calculations, which is valid in this case assuming that the Zeeman splitting is much large compared to the trion decay linewidth.

### A. Initialization pulse + free evolution

The excitation of the system by the  $\sigma_+$  initialization pulse with pulse area  $\theta$  can be describe by the unitary transformation matrix  $U_{\sigma_+}$ ,

$$U_{\sigma_+} = \begin{bmatrix} 1 & 0 & 0 \\ 0 & \cos \frac{\theta}{2} & -i \sin \frac{\theta}{2} \\ 0 & -i \sin \frac{\theta}{2} & \cos \frac{\theta}{2} \end{bmatrix}. \quad (\text{C.6})$$

The density matrix of the system after the initialization pulse is described by

$$\rho_I^{(z)} = U_{\sigma_+}^\dagger \rho_o^{(z)} U_{\sigma_+} = \frac{1}{2} \begin{bmatrix} 1 & 0 & 0 \\ 0 & \cos^2 \frac{\theta}{2} & \frac{-i}{2} \sin \theta \\ 0 & \frac{i}{2} \sin \theta & \sin^2 \frac{\theta}{2} \end{bmatrix}. \quad (\text{C.7})$$

For a initialization pulse area  $\theta = \pi$ , all the population in the  $|z+\rangle$  state is excited to the  $|t+\rangle$  state,

$$\rho_{I(\pi)}^{(z)} = \frac{1}{2} \begin{bmatrix} 1 & 0 & 0 \\ 0 & 0 & 0 \\ 0 & 0 & 1 \end{bmatrix}. \quad (\text{C.8})$$

From this point on, we will assume a initialization pulse area of  $\theta = \pi$  for calculation convenience. Before the initialization pulse, the unitary rotation of the magnetic field has no affect on the completely mixed spin states. After the  $\pi$  initialization pulse, half of the spin population is initialized as pure population in the  $|z-\rangle$  state as shown above, which is now subjected to the unitary rotation  $U_{B_x}$  by the magnetic

field along  $\hat{\mathbf{x}}$ ,

$$U_{B_x} = \begin{bmatrix} \cos \frac{\delta t}{2} & -i \sin \frac{\delta t}{2} & 0 \\ -i \sin \frac{\delta t}{2} & \cos \frac{\delta t}{2} & 0 \\ 0 & 0 & 1 \end{bmatrix}, \quad (\text{C.9})$$

where  $\delta$  is the splitting between the spin states in the  $\mathbf{x}$  basis. The free evolution of the density matrix in the magnetic field is

$$\rho_{I(\pi)_+}^{(z)} = U_{B_x}^\dagger \rho_{I(\pi)}^{(z)} U_{B_x} = \frac{1}{2} \begin{bmatrix} \cos^2 \frac{\delta t}{2} & \frac{-i}{2} \sin \delta t & 0 \\ \frac{i}{2} \sin \delta t & \sin^2 \frac{\delta t}{2} & 0 \\ 0 & 0 & 1 \end{bmatrix}. \quad (\text{C.10})$$

After the population from the trion state  $|t+\rangle$  decays equally into the two spin states while neglecting SGC, the density matrix is,

$$\rho_{I(\pi)_+}^{(z)} = \frac{1}{2} \begin{bmatrix} \cos^2 \frac{\delta t}{2} + \frac{1}{2} & \frac{-i}{2} \sin \delta t & 0 \\ \frac{i}{2} \sin \delta t & \sin^2 \frac{\delta t}{2} + \frac{1}{2} & 0 \\ 0 & 0 & 0 \end{bmatrix}, \quad (\text{C.11})$$

where the red fonts keep tracks of the decayed population.

## B. Control pulse + free evolution

The unitary transformation matrix for the control pulse is exactly the same as the initialization pulse. At  $t = t_c$ , the density matrix of the system after the control pulse is given by

$$\rho_{I(\pi)_+C}^{(z)} = U_{\sigma_+}^\dagger \rho_{I(\pi)_+}^{(z)} U_{\sigma_+} = \frac{1}{2} \begin{bmatrix} \cos^2 \frac{\delta t_c}{2} & \frac{-i}{2} \sin \delta t_c \cos \frac{\theta}{2} & -\frac{1}{2} \sin \delta t_c \sin \frac{\theta}{2} \\ \frac{i}{2} \sin \delta t_c \cos \frac{\theta}{2} & \sin^2 \frac{\delta t_c}{2} \cos^2 \frac{\theta}{2} & \frac{-i}{2} \sin^2 \frac{\delta t_c}{2} \sin \theta \\ -\frac{1}{2} \sin \delta t_c \sin \frac{\theta}{2} & \frac{i}{2} \sin^2 \frac{\delta t_c}{2} \sin \theta & \sin^2 \frac{\delta t_c}{2} \sin^2 \frac{\theta}{2} \end{bmatrix} \\ + \frac{1}{2} \begin{bmatrix} \frac{1}{2} & 0 & 0 \\ 0 & \frac{1}{2} \cos^2 \frac{\theta}{2} & \frac{-i}{4} \sin \theta \\ 0 & \frac{i}{4} \sin \theta & \frac{1}{2} \sin^2 \frac{\theta}{2} \end{bmatrix}. \quad (\text{C.12})$$

For  $\theta = \pi$  again, we have maximum effect on the spin states

$$\rho_{I(\pi)+C(\pi)}^{(z)} = \frac{1}{2} \begin{bmatrix} \cos^2 \frac{\delta t_c}{2} + \frac{1}{2} & 0 & -\frac{1}{2} \sin \delta t_c \\ 0 & 0 & 0 \\ -\frac{1}{2} \sin \delta t_c & 0 & \sin^2 \frac{\delta t_c}{2} + \frac{1}{2} \end{bmatrix}. \quad (\text{C.13})$$

Since the population from the trion will decay equally into the two spin states, it will not be subject to the unitary rotation of the magnetic field. Hence, the trion population will be neglected here. The density matrix after the decay with the neglected trion population is

$$\rho_{I(\pi)+\text{control}(\pi)}^{(z)} = \frac{1}{2} \begin{bmatrix} \cos^2 \frac{\delta t_c}{2} + \frac{1}{2} & 0 & 0 \\ 0 & 0 & 0 \\ 0 & 0 & 0 \end{bmatrix}. \quad (\text{C.14})$$

The free evolution induced by the unitary rotation of the magnetic field at  $t = t_c$  gives

$$\rho_{I(\pi)+\text{control}(\pi)+}^{(z)} = \frac{1}{2} \begin{bmatrix} (\cos^2 \frac{\delta t_c}{2} + \frac{1}{2}) \cos^2 \frac{\delta(t-t_c)}{2} & \frac{-i}{2} (\cos^2 \frac{\delta t_c}{2} + \frac{1}{2}) \sin \delta(t-t_c) & 0 \\ \frac{i}{2} (\cos^2 \frac{\delta t_c}{2} + \frac{1}{2}) \sin \delta(t-t_c) & (\cos^2 \frac{\delta t_c}{2} + \frac{1}{2}) \sin^2 \frac{\delta(t-t_c)}{2} & 0 \\ 0 & 0 & 0 \end{bmatrix} \quad (\text{C.15})$$

### C. Probe pulse signal to the first order

To first order of the probe, the signal is proportional to  $\rho_{x+t+}^{(1)} + \rho_{x-t+}^{(1)}$ . The zeroth order is solutions to the density matrix equations due to all order of the initialization and control pulses.

$$\rho_{x+t+}^{(1)} \propto \rho_{x+x+}^{(0)} + \rho_{x+x-}^{(0)}, \quad \rho_{x-t+}^{(1)} \propto \rho_{x-x-}^{(0)} + \rho_{x-x+}^{(0)} \quad (\text{C.16})$$

From section I, neglecting the red decay terms because they were not operated on

by both initialization and control pulses, we get

$$\rho_{x+x-}^{(0)} = \rho_{x-x-}^{(0)} = \frac{1}{2} \quad (\text{C.17})$$

$$\rho_{x+x-}^{(0)} = -\frac{1}{4}[\cos^2 \delta(t-t_c) - i \sin^2 \delta(t-t_c)] \cos^2 \frac{\delta t_c}{2} = -\frac{1}{8}(\cos \delta t_c + 1)e^{-i\delta(t-t_c)}, \quad (\text{C.18})$$

which leads to the final signal from the probe to be

$$signal \propto \rho_{x+t+}^{(1)} + \rho_{x-t+}^{(1)} \propto 1 - \frac{1}{4}(\cos \delta t_c + 1) \cos \delta(t-t_c) \quad (\text{C.19})$$

### III. Calculation signal vs. Data signal

The calculated signal and the signal from experimental data do not agree with each other as seen in Figure 6.7 in Chapter 6. For example, according to the calculation the signal diminishes when  $t_c = \frac{\pi}{\delta}$ , which is in agreement with the physical picture. However, in the data, the signal diminishes when  $t_c = \frac{\pi}{2\delta}$ . This discrepancy can be explain by accounting for the beam modulations used in our experiment.

In the experiment, the initialization and probe are each modulated at  $\Omega_1$  and  $\Omega_2$ , respectively, and the control is unmodulated. We can think of the control and probe together as one PROBE. The differential transmission (DT) signal is then

$$signal_{DT} \propto signal_{I_{on}} - signal_{I_{off}}, \quad (\text{C.20})$$

where the  $signal_{I_{on}}$  is shown in Equation C.19. The  $signal_{I_{off}}$  is signal due to the control and the probe without the initialization and it is given by

$$signal_{I_{off}} \propto 1 - \frac{1}{4} \cos \delta(t-t_c). \quad (\text{C.21})$$

From Equation C.19 and Equation C.21, we conclude that

$$signal_{DT} \propto \cos \delta t_c \cos \delta(t-t_c), \quad (\text{C.22})$$

which does indeed agree with the experimental data.

## BIBLIOGRAPHY



## BIBLIOGRAPHY

- [1] G. E. Moore, “Cramming more components onto integrated circuits”, *Electronics* **38** (1965).
- [2] D. P. DiVincenzo, “The physical implementation of quantum computation”, *Fortschr. Phys.* **48**, 771 (2000).
- [3] G. E. Moore, “No Exponential is Forever...but We Can Delay 'Forever'”, *presentation at International Solid State Circuits Conference (ISSCC)* (2003).
- [4] R. E. Feynman, “American Physical Society lecture, Dec 29, 1959: There’s plenty of room at the bottom”, *Engineering and Science, Caltech publication* (1960).
- [5] D. Deutsch, R. Jozsa, “Rapid Solution of Problems by Quantum Computation”, *Proc. R. Soc. Lond. A* **439**, 553 (1992).
- [6] P. W. Shor, “Polynomial-Time Algorithms for Prime Factorization and Discrete Logarithms on a Quantum Computer”, *SIAM J. Comput.* **26**, 1484 (1997).
- [7] L. K. Grover, “Quantum Mechanics Helps in Searching for a Needle in a Haystack”, *Phys. Rev. Lett.* **79**, 325 (1997).
- [8] W. K. Wootters, W. H. Zurek, “A Single Quantum Cannot be Cloned”, *Nature* **299**, 802 (1982).
- [9] M. A. Nielsen, I. L. Chuang, *Quantum Computation and Quantum Information*, Cambridge University Press, Cambridge, United Kingdom, first edition (2000).
- [10] J. Preskill, *Lecture Notes for Physics 229: Quantum information and Computation*, California Institute of Technology (September, 1998).
- [11] D. P. DiVincenzo, “Universal quantum computation with the exchange interaction”, *Nature* **408** (2000).
- [12] A. K. Lenstra, H. W. Lenstra, Jr., *Lecture Notes in Math: The development of the number field sieve*, Springer-Verlag, p.1554 (1993).
- [13] D. Gottesman, I. Chuang, “Quantum networks as enabling for quantum information science”, *Nature* **402**, 390 (1999).
- [14] C. W. Chou, J. Laurat, H. Deng, K. S. Choi, H. de Riedmatten, D. Felinto, H. J. Kimble, “Functional Quantum Nodes for Entanglement Distribution over Scalable Quantum Networks”, *Science* **316**, 316 (2007).

- [15] P. A. Hiskett, D. Rosenberg, C. G. Peterson, R. J. Hughes, S. Nam, A. E. Lita, A. J. Miller, J. E. Nordholt, “Long-distance quantum key distribution in optical fibre”, *New Journal of Physics* **8**, 193 (2006).
- [16] R. Ursin, F. Tiefenbacher, T. Schmitt-Manderbach, H. Weier, T. Scheidl, M. Lindenthal, B. Blauensteiner, T. Jennewein, J. Perdigues, P. Trojek, B. Oemer, M. Fuerst, M. Meyenburg, J. Rarity, Z. Sodnik, C. Barbieri, H. Weinfurter, A. Zeilinger, “Free-Space distribution of entanglement and single photons over 144 km”, *Nature Physics* **3**, 481 (2007).
- [17] V. Bouchiat, D. Vion, P. Joyez, D. Esteve, M. H. Devoret, “Quantum coherence with a single Cooper pair”, *Physica Scripta T* **76**, 165 (1998).
- [18] Y. Nakamura, Y. A. Pashkin, J. S. Tsai, “Coherent control of macroscopic quantum states in a single-Cooper-pair box”, *Nature* **398**, 786 (1999).
- [19] K. W. Lehnert, K. B. B. A. Turek, L. F. Spietz, D. Gunnarsson, P. Delsing, R. J. Schoelkopf, “Measurement of the excited-state lifetime of a microelectronic circuit”, *Phys. Rev. Lett.* **90**, 2 (2003).
- [20] J. H. Plantenberg, P. de Groot, C. Harmans, J. Mooij, “Demonstration of controlled-NOT quantum gates on a pair of superconducting quantum bits”, *Nature* **447**, 836 (2007).
- [21] F. H. L. Koppens, C. Buizert, I. T. Vink, K. C. Nowack, T. Meunier, L. P. Kouwenhoven, L. M. K. Vandersypen, “Detection of single electron spin resonance in a double quantum dot”, *Journal of Applied Physics* **101**, 081706 (2007).
- [22] A. Lupascu, S. Saito, T. Picot, P. C. de Groot, C. J. P. M. Harmans, J. E. Mooij, “Quantum non-demolition measurement of a superconducting two-level system”, *Nature Physics* **3**, 119 (2007).
- [23] J. A. Jones, M. Mosca, “Implementation of a quantum algorithm on a nuclear magnetic resonance quantum computer”, *Journal of Chemical Physics* **109** (1998).
- [24] N. Linden, H. Barjat, R. Freeman, “An implementation of the Deutsch-Jozsa algorithm on a three-qubit NMR quantum computer”, *Chemical Physics Letters* **296** (1998).
- [25] W. D. Phillips, “Laser cooling and trapping of neutral atoms”, *Rev. Mod. Phys.* **70** (1998).
- [26] C. Monroe, W. Swann, H. Robinson, C. Wieman, “Very Cold Trapped Atoms in a Vapor Cell”, *Phys. Rev. Lett.* **65** (1990).

- [27] B. B. Blinov, R. N. Kohn, Jr., M. J. Madsen, P. Maunz, D. L. Moehring, C. Monroe, “Broadband laser cooling of trapped atoms with ultrafast pulses”, *Journal of the Optical Society of America B* **23** (2006).
- [28] B. B. Blinov, L. Deslauriers, P. Lee, M. J. Madsen, R. Miller, C. Monroe, “Sympathetic cooling of trapped Cd+ isotopes”, *Phys. Rev. A* **65** (2002).
- [29] L. Deslauriers, P. C. Haljan, P. J. Lee, K.-A. Brickman, B. B. Blinov, M. J. Madsen, C. . Monroe, “Zero-Point cooling and low heating of trapped 111Cd+ ions”, *Phys. Rev. A* **70** (2003).
- [30] C. Monroe, D. Meekhof, B. King, W. Itano, D. Wineland, “Demonstration of a Universal Quantum Logic Gate”, *Phys. Rev. Lett.* **75** (1995).
- [31] D. Meekhof, C. Monroe, B. King, W. Itano, D. Wineland, “Generation of non-classical motional states of a trapped atom”, *Phys. Rev. Lett.* **76** (1996).
- [32] P. C. Haljan, K.-A. Brickman, L. Deslauriers, P. J. Lee, C. Monroe, “Spin-dependent Forces on Trapped Ions for Phase-Stable Quantum Gates and Motional Schrödinger Cat States”, *Phys. Rev. Lett.* **94** (2005).
- [33] B. B. Blinov, D. L. Moehring, L.-M. Duan, C. Monroe, “Observation of entanglement between a single trapped atom and a single photon”, *Nature* **428** (2004).
- [34] D. L. Moehring, P. Maunz, S. Olmschenk, K. C. Younge, D. N. Matsukevich, L.-M. Duan, C. Monroe, “Entanglement of Single Atom Quantum Bits at a Distance”, *Nature* **449** (2007).
- [35] D. Stick, W. K. Hensinger, S. Olmschenk, M. J. Madsen, K. Schwab, C. Monroe, “Ion Trap in Semiconductor Chip”, *Nature Physics* **2** (2006).
- [36] K. Kamath, P. Bhattacharya, T. Sosnowski, T. Norris, J. Phillips, “Room temperature operation of In<sub>0.4</sub>Ga<sub>0.6</sub>As/GaAs self-organized quantum dot lasers”, *Electronic Lett.* **32**, 1374 (1996).
- [37] S. Fafard, K. Hinzer, S. Raymond, M. Dion, J. McCaffrey, Y. Feng, S. Charbonneau, “Red-emitting semiconductor quantum dot lasers”, *Science* **274**, 1350 (1996).
- [38] H. Saito, K. Nishi, I. Ogura, S. Sugou, Y. Sugimoto, “Room-temperature lasing operation of a quantum-dot vertical-cavity surface-emitting laser”, *Appl. Phys. Lett.* **69**, 3140 (1996).
- [39] V. I. Klimov, A. A. Mikhailovsky, S. Xu, A. Malko, J. A. Hollingsworth, C. A. Leatherdale, H.-J. Eisler, M. G. Bawendi, “Optical Gain and Stimulated Emission in Nanocrystal Quantum Dots”, *Science* **290**, 314 (2000).

- [40] M. Grundmann, “The present status of quantum dot lasers”, *physica. E* **5**, 167 (2000).
- [41] P. Bhattacharya, S. Krishna, J. Phillips, P. J. McCann, K. Namjou, “Carrier dynamics in self-organized quantum dots and their application to long-wavelength sources and detectors”, *J. Crystal Growth* **84**, 2513 (2000).
- [42] X. D. Huang, A. Stintz, H. Li, L. F. Lester, J. Cheng, K. J. Malloy, “Passive mode-locking in 1.3  $\mu\text{m}$  two-section InAs quantum dot lasers”, *Appl. Phys. Lett.* **78**, 2825 (2000).
- [43] P. Michler, A. Kiraz, C. Becher, W. V. Schoenfeld, P. M. Petroff, L. Zhang, E. Hu, A. Imamoglu, “A quantum dot single-photon turnstile device”, *Science* **290**, 2282 (2000).
- [44] A. Imamoglu, Y. Yamamoto, “Turnstile device for heralded single photons: Coulomb blockade of electron and hole tunneling in quantum confined p-i-n heterojunctions”, *Phys. Rev. Lett.* **72**, 210 (1994).
- [45] C. Santori, M. Pelton, G. Solomon, Y. Dale, E. Yamamoto, “Triggered single photons from a quantum dot”, *Phys. Rev. Lett.* **86**, 1502 (2001).
- [46] T. Flissikowski, A. Hundt, M. Lowisch, M. Rabe, F. Henneberger, “Photon beats from a single semiconductor quantum dot”, *Phys. Rev. Lett.* **86**, 1502 (2001).
- [47] C. Becher, A. Kiraz, P. Michler, A. Imamoglu, W. V. Schoenfeld, P. M. Petroff, L. Zhang, E. Hu, “Triggered single photons from a quantum dot”, *Phys. Rev. B* **63**, 121312(R) (2001).
- [48] V. Zwiller, H. Blom, P. Jonsson, N. Panev, S. Jeppesen, T. Tsegaye, E. Goobar, M. E. Pistol, L. Samuelson, G. Bjork, “Single quantum dots emit single photons at a time: antibunching experiments”, *Appl. Phys. Lett.* **78**, 2476 (2001).
- [49] O. Benson, C. Santori, M. Pelton, Y. Yamamoto, “Regulated and entangled photons from a single quantum dot”, *Phys. Rev. Lett.* **84**, 2513 (2001).
- [50] D. Loss, D. P. D. Vincenzo, “Quantum computation with quantum dots”, *Phys. Rev. A* **57**, 120 (1998).
- [51] F. Troiani, U. Hohenester, E. Molinari, “Exploiting exciton-exciton interactions in semiconductor quantum dots for quantum-information processing”, *Phys. Rev. B* **62**, 2263 (2000).
- [52] E. Biolatti, R. C. Iotti, P. Zanardi, F. Rossi, “Quantum Information Processing with Semiconductor Macroatoms”, *Phys. Rev. Lett.* **85**, 5647 (2000).
- [53] P. Chen, C. Piermarocchi, L. J. Sham, “Control of Exciton Dynamics in Nanodots for Quantum Operations”, *Phys. Rev. Lett.* **87**, 067401 (2001).

- [54] A. Ekert, R. Jozsa, “Quantum computing and Shor’s algorithm”, *Rev. Mod. Phys.* **68**, 733 (1996).
- [55] A. Imamoglu, D. D. Awschalom, G. Burkard, D. P. DiVincenzo, D. Loss, M. Sherwin, A. Small, “Quantum information processing using quantum dot spins and cavity QED”, *Phys. Rev. Lett.* **83**, 4204 (1999).
- [56] A. P. Alivisatos, “Semiconductor clusters, nanocrystals, and quantum dots”, *Science* **271**, 933 (1996).
- [57] A. Eychmuller, A. Mews, H. Weller, “A quantum-dot quantum-well-CdS/HgS/CdS”, *Chem. Phys. Lett.* **208**, 59 (1993).
- [58] M. A. Hines, P. Guyot-Sionnest, “Synthesis and characterization of strongly luminescing ZnS-capped CdSe nanocrystals”, *J. Phys. Chem.* **100**, 468 (1996).
- [59] X. G. Peng, M. C. Schlamp, A. V. Kadavanich, A. P. Alivisatos, “Epitaxial growth of highly luminescent CdSe/GdS core/shell nanocrystals with photostability and electronic accessibility”, *J. Am. Chem. Soc.* **119**, 7019 (1997).
- [60] M. Bruchez, Jr., M. Monronne, P. Gin, S. Weiss, A. P. Alivisatos, “Semiconductor nanocrystals as fluorescent biological labels”, *Science* **281**, 2013 (1998).
- [61] W. C. W. Chan, S. Nie, “Quantum dot bioconjugates for ultrasensitive nonisotopic detection”, *Science* **281**, 2016 (1998).
- [62] K. Brunner, U. Bockelmann, G. Abstreiter, M. Walther, G. Böhm, G. Tränkle, G. Weimann, “Photoluminescence from a single GaAs/AlGaAs quantum dot”, *Phys. Rev. Lett.* **76**, 3216 (1992).
- [63] R. Steffen, T. Koch, J. Oshinowo, F. Faller, A. Forchel, “Photoluminescence study of deep etched InGaAs/GaAs quantum wires and dots defined by low-voltage electron beam lithography”, *Appl. Phys. Lett.* **68**, 223 (1995).
- [64] U. Bockelmann, P. Roussignol, A. Filoramo, W. Heller, G. Abstreiter, K. Brunner, G. Böhm, G. Weimann, “Time resolved spectroscopy of single quantum dots: Fermi gas of excitons?”, *Phys. Rev. Lett.* **76**, 3622 (1996).
- [65] W. Wegscheider, G. Schedelbeck, G. Abstreiter, M. Rother, M. Bichler, “Atomically precise GaAs/AlGaAs quantum dots fabricated by twofold cleaved edge overgrowth”, *Phys. Rev. Lett.* **79**, 1917 (1997).
- [66] U. Bockelmann, W. Heller, A. Filoramo, P. Roussignol, “Microphotoluminescence studies of single quantum dots. I. Time-resolved experiments”, *Phys. Rev. B* **55**, 4456 (1997).
- [67] U. Bockelmann, W. Heller, G. Abstreiter, “Microphotoluminescence studies of single quantum dots. II. Magnetic-field experiments”, *Phys. Rev. B* **55**, 4469 (1997).

- [68] X. G. Peng, L. Manna, W. Yang, J. Wickham, E. Scher, A. Kadavanich, A. P. Alivisatos, "Shape control of CdSe nanocrystals", *Nature* **404**, 59 (2000).
- [69] V. F. Puntès, K. M. Krishna, A. P. Alivisatos, "Colloidal nanocrystal shape and size control: The case of cobalt", *Science* **291**, 2115 (2001).
- [70] J. Hu, L. Shi Li, W. Yang, L. Manna, L. Wang Wang, A. P. Alivisatos, "Linearly polarized emission from colloidal semiconductor quantum rods", *Science* **292**, 2060 (2001).
- [71] L. Manna, E. C. Scher, A. P. Alivisatos, "Synthesis of soluble and processable rod-, arrow-, teardrop-, and tetrapod-shaped CdSe nanocrystals", *J. Am. Chem. Soc.* **122**, 12700 (2000).
- [72] H. F. Hess, E. Betzig, T. D. Harris, "Near-field spectroscopy of the quantum constituents of a luminescent system", *Science* **264**, 1740 (1994).
- [73] K. Brunner, G. Abstreiter, G. Böhm, G. Tränkle, G. Weimann, "Sharp-line photoluminescence and two-photon absorption of zero-dimensional biexcitons in a GaAs/AlGaAs structure", *Phys. Rev. Lett.* **73**, 1138 (1994).
- [74] A. Zrenner, L. V. Butov, M. Hagn, G. Abstreiter, G. Böhm, G. Weimann, "Quantum dots formed by interface fluctuations in AlAs/GaAs coupled quantum well structures", *Phys. Rev. Lett.* **72**, 3382 (1994).
- [75] D. Gammon, E. S. Snow, B. V. Shanabrook, D. S. Katzer, D. Park, "Homogeneous Linewidths in the Optical Spectrum of a Single Gallium Arsenide Quantum Dot", *Science* **273**, 87 (1996).
- [76] T. H. Stievater, X. Li, D. G. Steel, D. Gammon, D. S. Katzer, D. Park, C. Piermarocchi, L. J. Sham, "Rabi Oscillations of Excitons in Single Quantum Dots", *Phys. Rev. Lett.* **87**, 133603 (2001).
- [77] J. R. Guest, T. H. Stievater, X. Li, J. Cheng, D. G. Steel, D. Gammon, D. S. Katzer, D. Park, C. Ell, A. Thränhardt, G. Khitrova, H. M. Gibbs, "Measurement of optical absorption by a single quantum dot exciton", *Phys. Rev. Lett.* **65**, 241310 (2002).
- [78] P. M. Petroff, S. P. DenBaars, "MBE and MOCVD growth and properties of self-assembling quantum dot arrays in III-V semiconductor structures", *Superlattices and Microstructures* **15**, 15 (1994).
- [79] D. J. Eaglesham, M. Cerullo, "Dislocation-free Stranski-Krastanow growth of Ge on Si (100)", *Phys. Rev. Lett.* **64**, 1943 (1994).
- [80] N. Richard, "Self-organized growth of quantum dot structures", *Semicond. Sci. Tech.* **11**, 1365 (1996).

- [81] P. M. Petroff, A. Lorke, A. Imamoglu, “Epitaxially self-assembled quantum dots”, *Physics Today* **54**, 46 (2001).
- [82] X. Xu, B. Sun, P. R. Berman, D. G. Steel, A. S. Bracker, D. Gammon, L. J. Sham, “Coherent optical spectroscopy of a strongly driven quantum dot”, *Science* **317**, 929 (2007).
- [83] T. Takagahara, *Quantum Coherence, Correlation and Decoherence in Semiconductor Nanostructure*, Academic Press, Elsevier Science, San Diego, first edition (2003).
- [84] N. Peyghambarian, S. W. Koch, A. Mysyrowicz, *Introduction to Semiconductor Optics*, Prentice-Hall, Inc, New Jersey, first edition (1993).
- [85] N. W. Ashcroft, N. D. Mermin, *Solid State Physics*, Thomson Learning, Inc, USA, first edition (1976).
- [86] J. M. Luttinger, W. Kohn, “Motion of Electrons and Holes in Perturbed Periodic Fields”, *Phys. Rev.* **97**, 869 (1955).
- [87] M. P. Marder, *Condensed Matter Physics*, John Wiley, Chichester, New York, first edition (2000).
- [88] D. Gammon, E. S. Snow, B. V. Shanabrook, D. S. Katzer, D. Park, “Fine Structure Splitting in the Optical Spectra of Single GaAs Quantum Dots”, *Phys. Rev. Lett.* **76**, 3005 (1996).
- [89] Q. Wu, R. D. Grober, D. Gammon, D. S. Katzer, “Imaging Spectroscopy of Two-Dimensional Excitons in a Narrow GaAs/AlGaAs Quantum Well”, *Phys. Rev. Lett.* **83**, 2652 (1999).
- [90] J. G. Tischler, A. S. Bracker, D. Gammon, D. Park, “Fine Structure of Trions and Excitons in Single GaAs Quantum Dots”, *Phys. Rev. B* **66**, 081310 (2002).
- [91] A. Thränhardt, C. Ell, G. Khitrova, H. M. Gibbs, “Anisotropic emission of interface fluctuation quantum dots”, *Eur. Phys. J. B* **27**, 571 (2002).
- [92] S. Adachi, “GaAs, AlAs and  $\text{Al}_x\text{Ga}_{1-x}\text{As}$ : Material parameter for use in research and device applications”, *J. Appl. Phys.* **58**, 3 (1985).
- [93] J. R. Guest, T. H. Stievater, G. Chen, E. A. Tabak, B. G. Orr, D. G. Steel, D. Gammon, D. S. Katzer, “Near-Field Coherent Spectroscopy and Microscopy of a Quantum Dot System”, *Science* **293**, 2224.
- [94] J. R. Guest, *Near-field coherent optical spectroscopy and microscopy of a mesoscopic quantum system*, Ph.D. thesis, The University of Michigan, The Harrison M. Randall Laboratory of Physics, Ann Arbor MI 48109-1120 (2000).

- [95] T. Tanaka, J. Singh, Y. Arakawa, P. Bhattacharya, “Near band edge polarization dependence as a probe of structural symmetry in GaAs/AlGaAs quantum dot structures”, *Appl. Phys. Lett.* **62**, 756 (1993).
- [96] T. Takagahara, “Theory of exciton fine structures and extremely slow spin relaxation in single quantum dots”, *J. Lumi.* **87-89**, 308 (2000).
- [97] H. W. van Kesteren, E. C. Cosman, F. J. A. M. Greidanus, P. Dawson, K. J. Moore, C. T. Foxon, “Optically Detected Magnetic Resonance Study of a Type-II GaAs-AlAs Multiple Quantum Well”, *Phys. Rev. Lett.* **61**, 129 (1988).
- [98] H. W. van Kesteren, E. C. Cosman, W. A. J. A. van der Poel, C. T. Foxon, “Fine structure of excitons in type-II GaAs/AlAs quantum wells”, *Phys. Rev. B* **41**, 5283 (1990).
- [99] E. Blackwood, M. J. Snelling, R. T. Harley, S. R. Andrews, C. T. Foxon, “Exchange interaction of excitons in GaAs heterostructures”, *Phys. Rev. B* **50**, 14246 (1994).
- [100] S. Glasberg, H. Shtrikman, I. Bar-Joseph, P. C. Klipstein, “Exciton exchange splitting in wide GaAs quantum wells”, *Phys. Rev. Lett.* **60**, 16295 (1990).
- [101] T. Takagahara, “Theory of exciton doublet structures and polarization relaxation in single quantum dots”, *Phys. Rev. Lett.* **62**, 16840 (2000).
- [102] S. V. Goupolov, E. L. Ivchenko, A. V. Kavokin, “Fine structure of localized exciton levels in quantum wells”, *J. Exp. and Theor. Phys.* **86**, 388 (1998).
- [103] E. L. Ivchenko, “Fine structure of excitonic levels in semiconductor nanostructures”, *Phys. Stat. Sol. (a)* **164**, 487 (1997).
- [104] X. Li, Y. Wu, D. Steel, D. Gammon, T. H. Stievater, D. S. Katzer, D. Park, C. Piermarocchi, L. J. Sham, “An All-Optical Quantum Gate in a Semiconductor Quantum Dot”, *Science* **301**, 809 (2003).
- [105] X. Li, Y. Wu, D. Steel, D. Gammon, T. H. Stievater, D. S. Katzer, D. Park, C. Piermarocchi, L. J. Sham, “Raman coherence beats from the entangled state involving polarized excitons in single quantum dots”, *Phys. Rev. B* **70**, 195330 (2004).
- [106] M. Kroutvar, Y. Ducommun, D. Heiss, M. Bichler, D. Schuh, G. Abstreiter, J. J. Finley, “Optically programmable electron spin memory using semiconductor quantum dots”, *Nature* **432**, 81 (2004).
- [107] J. M. Elzerman, R. Hanson, L. H. W. van Beveren, B. Witkamp, L. M. K. Vandersypen, L. P. Kouwenhoven, “Single-shot read-out of an individual electron spin in a quantum dot”, *Nature* **430**, 431 (2004).



- [108] A. Greilich, R. Oulton, E. A. Zhukov, I. A. Yugova, D. R. Yakovlev, M. Bayer, A. Shabaev, A. L. Efros, I. A. Merkulov, V. Stavarache, D. Reuter, A. Wieck, “Optical Control of Spin Coherence in Singly Charged (In, Ga)As/GaAs Quantum Dots”, *Phys. Rev. Lett.* **96**, 227401 (2006).
- [109] J. R. Petta, A. C. Johnson, J. M. Taylor, E. A. Laird, A. Yacoby, M. D. Lukin, C. M. Marcus, M. P. Hanson, A. C. Gossard, “Coherent Manipulation of Coupled Electron Spins in Semiconductor Quantum Dots”, *Science* **309**, 2180 (2005).
- [110] A. Greilich, D. R. Yakovlev, A. Shabaev, A. L. Efros, I. A. Yugova, R. Oulton, V. Stavarache, D. Reuter, A. Wieck, M. Bayer, “Mode Locking of Electron Spin Coherences in Singly Charged Quantum Dots”, *Science* **313**, 341 (2006).
- [111] C. Piermarocchi, P. Chen, L. J. Sham, D. G. Steel, “Optical RKKY Interaction between Charged Semiconductor Quantum Dots”, *Phys. Rev. Lett.* **89**, 167402 (2002).
- [112] A. S. Bracker, E. A. Stinaff, D. Gammon, M. E. Ware, J. G. Tischler, D. Park, D. Gershoni, A. V. Filinov, M. Bonitz, A. V. Filinov, M. Bonitz, “Binding energies of positive and negative trions: From quantum wells to quantum dots”, *Phys. Rev. B* **72**, 035332 (2005).
- [113] J. Cheng, *Coherent nonlinear optical spectroscopy of electron spin in charged semiconductor quantum dots*, Ph.D. thesis, The University of Michigan, The Harrison M. Randall Laboratory of Physics, Ann Arbor MI 48109-1120 (2006).
- [114] M. V. G. Dutt, J. Cheng, B. Li, X. Xu, X. Li, P. R. Berman, D. G. Steel, A. S. Bracker, D. Gammon, S. E. Economou, R.-B. Liu, L. J. Sham, “Stimulated and Spontaneous Optical Generation of Electron Spin Coherence in Charged GaAs Quantum Dots”, *Phys. Rev. Lett.* **94**, 227403 (2005).
- [115] R. Winkler, S. J. Papadakis, E. P. D. Poortere, M. Shayegan, “Highly anisotropic g-factor of two-dimensional hole systems”, *Phys. Rev. Lett.* **85**, 4574 (2000).
- [116] J. Cheng, Y. Wu, X. Xu, D. Sun, D. Steel, A. Bracker, D. Gammon, W. Yao, L. Sham, “Spin relaxation in charged quantum dots measured by coherent optical phase modulation spectroscopy”, *Solid State Communications* **140**, 381 (2006).
- [117] M. V. G. Dutt, J. Cheng, Y. Wu, X. Xu, D. G. Steel, A. S. Bracker, D. Gammon, S. E. Economou, R.-B. Liu, L. J. Sham, “Ultrafast optical control of electron spin coherence in charged GaAs quantum dots”, *Phys. Rev. B* **74**, 125306 (2006).
- [118] E. A. Stinaff, M. Scheibner, A. S. Bracker, I. V. Ponomarev, V. L. Korenev, M. E. Ware, M. F. Doty, T. L. Reinecke, D. Gammon, “Optical Signatures of Coupled Quantum Dots”, *Science* **311**, 636 (2006).

- [119] M. E. Ware, E. A. Stinaff, D. Gammon, M. F. Doty, A. S. Bracker, D. Gershoni, V. L. Korenev, Ş. C. Bădescu, Y. Lyanda-Geller, T. L. Reinecke, “Polarized Fine Structure in the Photoluminescence Excitation Spectrum of a Negatively Charged Quantum Dot”, *Phys. Rev. Lett.* **95**, 177403 (2005).
- [120] J. M. García, G. Medeiros-Ribeiro, K. Schmidt, T. Ngo, J. L. Feng, A. Lorke, J. Kotthaus, P. M. Petroff, “Intermixing and shape changes during the formation of InAs self-assembled quantum dots”, *Appl. Phys. Lett.* **71**, 2014 (1997).
- [121] A. V. Koudinov, I. A. Akimov, Y. G. Kusrayev, F. Henneberger, “Optical and magnetic anisotropies of the hole states in Stranski-Krastanov quantum dots”, *Phys. Rev. B* **70**, 241305 (2004).
- [122] X. Xu, Y. Wu, B. Sun, Q. Huang, J. Cheng, D. Steel, A. Bracker, D. Gammon, C. Emary, L. Sham, “Fast spin state initialization in a singly charged InAs-GaAs quantum dot by optical cooling”, *Phys. Rev. Lett.* **99**, 097401 (2007).
- [123] A. Müller, E. B. Flagg, P. Bianucci, X. Wang, D. G. Deppe, W. Ma, J. Zhang, M. Xiao, G. J. Salamo, C.-K. Shih, “Resonance fluorescence from a coherently driven semiconductor quantum dot in a cavity”, *Phys. Rev. Lett.* **99**, 187402 (2007).
- [124] Y. Wu, X. Li, L. M. Duan, D. G. Steel, D. Gammon, “Density Matrix Tomography through Sequential Coherent Optical Rotations of an Exciton Qubit in a Single Quantum Dot”, *Phys. Rev. Lett.* **96**, 087402 (2006).
- [125] N. H. Bonadeo, J. Erland, D. Gammon, D. Park, D. S. Katzer, D. G. Steel, “Coherent Optical Control of the Quantum State of a Single Quantum Dot”, *Science* **282**, 1473 (1998).
- [126] L. Allen, J. H. Eberly, *Optical Resonance and Two-level Atoms*, Dover Publications Inc., New York, first edition (1987).
- [127] P. Meystre, M. Sargent, *Elements of Quantum Optics*, Springer-Verlag, New York, third edition (1999).
- [128] M. O. Scully, M. S. Zubairy, *Quantum Optics*, Cambridge University Press, Cambridge, United Kingdom, first edition (1997).
- [129] N. Rose, C. Zener, “Double Stern-Gerlach experiment and related collision phenomena”, *Phys. Rev.* **40**, 502 (1932).
- [130] F. W. Byron, Jr., R. W. Fuller, *Mathematics of Classical and Quantum Physics*, Dover Publication Inc., New York, third edition (1992).
- [131] N. H. Bonadeo, G. Chen, D. Gammon, D. S. Katzer, D. Park, D. G. Steel, “Nonlinear Nano-Optics: Probing One Exciton at a Time”, *Phys. Rev. Lett.* **81**, 2759 (1998).

- [132] H. Kamada, H. Gotoh, J. Temmyo, T. Takagahara, H. Ando, “Exciton Rabi Oscillation in a Single Quantum Dot”, *Phys. Rev. Lett.* **87**, 246401 (2001).
- [133] H. Htoon, T. Takagahara, D. Kulik, O. Baklenov, A. L. H. Jr., C. K. Shih, “Interplay of Rabi Oscillations and Quantum Interference in Semiconductor Quantum Dots”, *Phys. Rev. Lett.* **88**, 087401 (2002).
- [134] A. Zrenner, E. Beham, S. Stuffer, F. Findeis, M. Bichler, G. Abstreiter, “Coherent properties of a two-level system based on a quantum-dot photodiode”, *Nature* **418**, 612 (2002).
- [135] T. Calarco, A. Datta, P. Fedichev, E. Pazy, P. Zoller, “Spin-based all-optical quantum computation with quantum dots: Understanding and suppressing”, *Phys. Rev. A* **68**, 012310 (2003).
- [136] C. Piermarocchi, P. Chen, Y. S. Dale, L. J. Sham, “Theory of fast quantum control of exciton dynamics in semiconductor quantum dots”, *Phys. Rev. B* **65**, 075307 (2002).
- [137] R. Hanson, L. H. W. van Beveren, I. T. Vink, J. M. Elzerman, W. J. M. Naber, F. H. L. Koppens, L. P. Kouwenhoven, L. M. K. Vandersypen, “Single-shot read-out of electron spin states in a quantum dot using spin-dependent tunnel rates”, *Phys. Rev. Lett.* **94**, 196802 (2005).
- [138] Q. Q. Wang, A. Muller, M. T. Cheng, H. J. Zhou, P. Bianucci, C. K. Shih, “Coherent Control of a V-Type Three-Level System in a Single Quantum Dot”, *Phys. Rev. Lett.* **95**, 187404 (2005).
- [139] A. M. Childs, I. L. Chuang, D. W. Leung, “Realization of quantum process tomography in NMR”, *Phys. Rev. A* **64**, 012314 (2001).
- [140] P. C. Haljan, P. J. Lee, K.-A. Brickman, M. Acton, L. Deslauriers, C. Monroe, “Fine Structure Splitting in the Optical Spectra of Single GaAs Quantum Dots”, *Phys. Rev. A* **72**, 062316 (2005).
- [141] W. Gerlach, O. Stern, “Der experimentelle nachweis der richtungsquantelung im magnetfeld”, *Zeits. Phys.* **9**, 349 (1922).
- [142] C. Froehly, B. Colombeau, M. Vampouille, “Highly simplified device for ultrashort-pulses measurement”, *Progress in Optics* **20**, 65 (1983).
- [143] A. M. Weiner, “Femtosecond optical pulse shaping and processing”, *Prog. Quant. Electron* **19**, 161 (1995).
- [144] F. H. L. Koppens, C. Buizert, K. J. Tielrooij, I. T. Vink, K. C. Nowack, T. Meunier, L. P. Kouwenhoven, L. M. K. Vandersypen, “Driven coherent oscillations of a single electron spin in a quantum dot”, *Nature* **442**, 766 (2006).

- [145] Y. Wu, E. D. Kim, X. Xu, J. Cheng, D. G. Steel, A. S. Bracker, D. Gammon, S. E. Economou, L. J. Sham, “Selective optical control of electron spin coherence in singly charged GaAs-Al<sub>0.3</sub>Ga<sub>0.7</sub>As quantum dots”, *Phys. Rev. Lett.* **99**, 097402 (2007).
- [146] Y. Shen, A. M. Goebel, H. Wang, “Control of quantum beats from electron spin coherence in semiconductor quantum wells”, *Phys. Rev. B* **75**, 045341 (2007).
- [147] J. A. Gupta, R. Knobel, N. Samarth, D. D. Awschalom, “Ultrafast manipulation of electron spin coherence”, *Science* **292**, 2458 (2001).
- [148] H. R. Gray, R. M. Whitley, C. R. Stroud, Jr., “Coherent trapping of atomic populations”, *Optics Letters* **3**, 218 (1978).
- [149] C. R. Stroud, Jr., D. A. Cardimona, “Double resonance self-induced transparency”, **37**, 221 (1981).
- [150] V. Milner, Y. Prior, “Multilevel dark states: coherent population trapping with elliptically polarized incoherent light”, *Phys. Rev. Lett.* **80**, 940 (1997).
- [151] P. R. Berman, “Spontaneously generated coherence and dark states”, *Phys. Rev. A* **72**, 035801 (2005).
- [152] R. M. Whitley, C. R. Stroud, Jr., “Double optical resonance”, *Phys. Rev. A* **14**, 1498 (1976).
- [153] K. Zaheer, M. S. Zubairy, “Phase sensitivity in atom-field interaction via coherent superposition”, *Phys. Rev. A* **39**, 2000 (1989).
- [154] S. E. Harris, J. E. Field, A. Imamoglu, “Nonlinear optical processes using electromagnetically induced transparency”, *Phys. Rev. Lett.* **64**, 1107 (1990).
- [155] K. H. Hahn, K. D. A. S. E. Harris, “Nonlinear generation of 104.8-nm radiation within an absorption window in zinc”, *Phys. Rev. Lett.* **65**, 2777 (1990).
- [156] K.-J. Boller, A. Imamoglu, S. E. Harris, “Observation of electromagnetically induced transparency”, *Phys. Rev. Lett.* **66**, 2593 (1991).
- [157] J. E. Field, K. H. Hahn, S. E. Harris, “Electric-field-induced second-harmonic generation with reduced absorption in atomic hydrogen”, *Phys. Rev. Lett.* **67**, 3062 (1991).
- [158] K. Hakuta, L. Marmet, B. Stoicheff, “Electric-field-induced second-harmonic generation with reduced absorption in atomic hydrogen”, *Phys. Rev. Lett.* **66**, 596 (1991).
- [159] A. Javan, “Theory of a Three-Level Maser”, *Phys. Rev.* **107**, 1579 (1956).
- [160] S. E. Harris, “Lasers without inversion: Interference of lifetime-broadened resonances”, *Phys. Rev. Lett.* **62**, 1033 (1989).

- [161] M. O. Scully, S. Y. Zhu, A. Gavrielides, “Degenerate quantum-beat laser: Lasing without inversion and inversion without lasing”, *Phys. Rev. Lett.* **62**, 2813 (1989).
- [162] S. E. Harris, J. H. Macklin, “Lasers without inversion: Single-atom transient response”, *Phys. Rev. A* **40**, 4135 (1989).
- [163] A. Imamoglu, “Interference of radiatively broadened resonances”, *Phys. Rev. A* **40**, 2835 (1989).
- [164] A. Lyras, X. Tang, P. Lambropoulos, J. Zhang, “Radiation amplification through autoionizing resonances without population inversion”, *Phys. Rev. A* **40**, 4131 (1989).
- [165] P. Matre, R. Dum, R. Taieb, P. Zoller, “Resonance fluorescence from quantized one-dimensional molasses”, *Phys. Rev. A* **47**, 1378 (1993).
- [166] N. Lutkenhaus, J. I. Cirac, P. Zoller, “Mimicking a squeezed-bath interaction: Quantum-reservoir engineering with atoms”, *Phys. Rev. A* **57**, 548 (1998).
- [167] C. W. Gardiner, *Handbook of stochastic methods*, Springer, New York, second edition (1985).
- [168] C. W. Gardiner, P. Zoller, *Quantum noise*, Springer, New York, second edition (2000).
- [169] Z. Kis, F. Renzoni, “Qubit rotation with stimulated Raman adiabatic passage”, *Phys. Rev. A* **65** (2002).
- [170] P. Chen, C. Piermarocchi, L. J. Sham, D. Gammon, D. G. Steel, “Theory of quantum optical control of a single spin in a quantum dot”, *Phys. Rev. B* **69**, 075320 (2004).
- [171] S. E. Economou, L. J. Sham, Y. Wu, D. G. Steel, “Proposal for optical U(1) rotations of electron spin trapped in a quantum dot”, *Phys. Rev. B* **74**, 205415 (2006).
- [172] A. Shabaev, A. L. Efros, D. Gammon, I. A. Merkulov, “Optical readout and initialization of an electron spin in a single quantum dot”, *Phys. Rev. B* **68**, 201305 (2003).
- [173] A. Imamoglu, E. Knill, L. Tian, P. Zoller, “Optical Pumping of Quantum-Dot Nuclear Spins”, *Phys. Rev. Lett.* **91**, 017402 (2003).
- [174] C. Emary, L. J. Sham, “Optically controlled single-qubit rotations in self-assembled InAs quantum dots”, *J. Phys.: Condens. Matter* **19**, 056203 (2007).
- [175] M. F. Doty, M. Scheibner, I. V. Ponomarev, E. A. Stinaff, A. S. Bracker, V. L. Korenev, T. L. Reinecke, D. Gammon, “Electrically Tunable g Factors in Quantum Dot Molecular Spin States”, *Phys. Rev. Lett.* **97**, 197202 (2006).

- [176] M. Atatüre, J. Dreiser, A. Badolato, A. Högele, K. Karrai, A. Imamoglu, “Quantum-Dot Spin-State Preparation with Near-Unity Fidelity”, *Science* **310**, 551 (2006).
- [177] A. S. Bracker, M. Scheibner, M. F. Doty, E. A. Stinaff, I. V. Ponomarev, J. C. Kim, L. J. Whitman, T. L. Reinecke, D. Gammon, “Engineering electron and hole tunneling with asymmetric InAs quantum dot molecules”, *Appl. Phys. Lett.* **89** (2006).
- [178] J. Tersoff, C. Teichert, M. G. Lagally, “Self-organization in growth of quantum dot superlattices”, *Phys. Rev. Lett.* **76**, 1675 (1996).
- [179] Q. Xie, A. Madhukar, P. Chen, N. P. Kobayshi, “Vertically self-organized InAs quantum box islands on GaAs (100)”, *Phys. Rev. Lett.* **75**, 2542 (1995).
- [180] M. Scheibner, M. F. Doty, I. V. Ponomarev, A. S. Bracker, E. A. Stinaff, V. L. Korenev, T. L. Reinecke, D. Gammon, “Spin fine structure of optically excited quantum dot molecules”, *Phys. Rev. B* **75** (2007).